USGS
science for a changing world

هيئة المساحة الجيولوجية السعودية
SAUDI GEOLOGICAL SURVEY

Eruptive History of Northern Harrat Rahat—Volume, Timing, and Composition of Volcanism Over the Past 1.2 Million Years

Chapter D of
Active Volcanism on the Arabian Shield—Geology, Volcanology, and Geophysics of Northern Harrat Rahat and Vicinity, Kingdom of Saudi Arabia

U.S. Geological Survey Professional Paper 1862
Saudi Geological Survey Special Report SGS–SP–2021–1

U.S. Department of the Interior
U.S. Geological Survey

Cover. U.S. Geological Survey photograph looking south at Um Junb, within the Matan volcanic center. Um Junb erupted pyroclastic trachyte deposits and produced a steep sided benmoreite dome approximately 438 thousand years ago. A lava flow can be seen breaching the crater rim of Um Junb. In the foreground are the rubbly tops of basaltic lava flows. Background image shows northern Harrat Rahat lava flows, maars, and lava domes. U.S. Geological Survey photograph by Andrew Calvert, January 25, 2012.

Eruptive History of Northern Harrat Rahat—Volume, Timing, and Composition of Volcanism Over the Past 1.2 Million Years

By Mark E. Stelten, Drew T. Downs, Duane E. Champion, Hannah R. Dietterich, Andrew T. Calvert, Thomas W. Sisson, Gail A. Mahood, and Hani M. Zahran

Chapter D of

Active Volcanism on the Arabian Shield—Geology, Volcanology, and Geophysics of Northern Harrat Rahat and Vicinity, Kingdom of Saudi Arabia

Edited by Thomas W. Sisson, Andrew T. Calvert, and Walter D. Mooney

U.S. Geological Survey Professional Paper 1862
Saudi Geological Survey Special Report SGS–SP–2021–1

U.S. Department of the Interior
U.S. Geological Survey

U.S. Geological Survey, Reston, Virginia: 2023

Suggested citation:
Stelten, M.E., Downs, D.T., Champion, D.E., Dietterich, H.R., Calvert, A.T., Sisson, T.W., Mahood, G.A., and Zahran, H.M., 2023, Eruptive history of northern Harrat Rahat—Volume, timing, and composition of volcanism over the past 1.2 million years, chap. D *of* Sisson, T.W., Calvert, A.T., and Mooney, W.D., eds., Active volcanism on the Arabian Shield—Geology, volcanology, and geophysics of northern Harrat Rahat and vicinity, Kingdom of Saudi Arabia: U.S. Geological Survey Professional Paper 1862 [also released as Saudi Geological Survey Special Report SGS–SP–2021–1], 46 p., https://doi.org/10.3133/pp1862D.

Associated data for this publication:
Stelten, M.E., 2021, Ar isotope data for volcanic rocks from the northern Harrat Rahat volcanic field and surrounding area, Kingdom of Saudi Arabia: U.S. Geological Survey data release, https://doi.org/10.5066/P92FB6AQ.

ISSN 1044-9612 (print)
ISSN 2330-7102 (online)

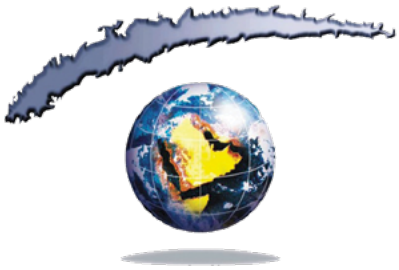

هيئة المساحة الجيولوجية السعودية
SAUDI GEOLOGICAL SURVEY

Ministry of Industry and Mineral Resources
BANDAR BIN IBRAHIM BIN ABDULLAH AL-KHORAYEF, Minister and SGS Chairman

Saudi Geological Survey
Abdullah bin Mufter Al-Shamrani, Chief Executive Officer

Saudi Geological Survey, Jiddah, Kingdom of Saudi Arabia: 2023

Contents

Figures

Tables

Conversion Factors

International System of Units to U.S. customary units

Multiply	By	To obtain
	Length	
centimeter (cm)	0.3937	inch (in.)
millimeter (mm)	0.03937	inch (in.)
meter (m)	3.281	foot (ft)
kilometer (km)	0.6214	mile (mi)
kilometer (km)	0.5400	mile, nautical (nmi)
meter (m)	1.094	yard (yd)
	Area	
square kilometer (km^2)	247.1	acre
square kilometer (km^2)	0.3861	square mile (mi^2)
	Volume	
cubic kilometer (km^3)	0.2399	cubic mile (mi^3)

Temperature in degrees Celsius (°C) may be converted to degrees Fahrenheit (°F) as follows:

$$°F = (1.8 \times °C) + 32.$$

Datum

Vertical coordinate information is referenced to the World Geodetic System of 1984 (WGS 1984).

Abbreviations

C.E.	Common Era
DEM	digital elevation model
DRE	dense rock equivalent
ICP-AES	inductively coupled plasma atomic emission spectrometry
ICP-MS	inductively coupled plasma mass spectrometry
ka	kilo-annum
km^3/k.y.	cubic kilometer per thousand years
k.y.	thousand years
LAB	lithosphere-asthenosphere boundary
Ma	mega-annum
mg	milligram
µm	micrometer
mm/k.y.	millimeter per thousand years
MMN	Makkah-Madīnah-Nafud
Moho	Mohorovičić discontinuity
m.y.	million years
SGS	Saudi Geological Survey
USGS	U.S. Geological Survey
XRF	X-ray fluorescence
±	plus or minus

Active Volcanism on the Arabian Shield
Edited by T.W. Sisson, A.T. Calvert, and W.D. Mooney
U.S. Geological Survey Professional Paper 1862
Saudi Geological Survey Special Report SGS–SP–2021–1

Chapter D

Eruptive History of Northern Harrat Rahat—Volume, Timing, and Composition of Volcanism Over the Past 1.2 Million Years

By Mark E. Stelten, [1] Drew T. Downs,[1] Duane E. Champion,[2] Hannah R. Dietterich,[1] Andrew T. Calvert,[1] Thomas W. Sisson,[1] Gail A. Mahood,[3] and Hani M. Zahran[4]

Abstract

Harrat Rahat, one of several large, basalt-dominated volcanic fields in the western part of the Kingdom of Saudi Arabia, is a prime example of continental, intraplate volcanism. Excellent exposure makes this an outstanding site to investigate changing volcanic flux and composition through time. We present 93 $^{40}Ar/^{39}Ar$ ages and 6 ^{36}Cl surface-exposure ages for volcanic deposits throughout northern Harrat Rahat that, integrated with a new geologic map, define 12 eruptive stages. Exposed volcanic deposits in the study area erupted less than 1.2 million years ago (Ma), and 214 of 234 identified eruptions occurred less than 570 thousand years ago (ka). Two eruptions were in the Holocene, including a historically described basaltic eruption in 1256 C.E. and a trachyte eruption newly recognized as Holocene (4.2±5.2 ka). An estimated approximately 82 cubic kilometers (km^3; dense rock equivalent) of volcanic products can be documented as having erupted since 1.2 Ma, though this is a lower limit because of concealment of deposits older than 570 ka. Over the last 570 thousand years (k.y.), the average eruption rate was 0.14 cubic kilometers per thousand years (km^3/k.y.), but volcanism was episodic with periods alternating between low (0.04–0.06 km^3/k.y.) and high (0.1–0.3 km^3/k.y.) effusion rates. Before 180 ka, eruptions vented from the volcanic field's dominant eastern vent axis and from a subsidiary, diffuse, western vent axis. After 180 ka, volcanism focused along the eastern vent axis, and the composition of volcanism varied systematically along its length from basalt dominated in the north to trachyte dominated in the south. We hypothesize that these compositional variations younger than 180 k.y. reflect the growth of a mafic intrusive complex beneath the southern part of the vent axis, which led to the development of evolved magmas. Lastly, these new age data allow for a reassessment of the volcanic recurrence interval at northern Harrat Rahat. Based on available data, volcanism in northern Harrat Rahat over the last 180 k.y. is poorly described using a Poisson distribution with a single recurrence interval. Instead, data for northern Harrat Rahat are better described using a mixed exponential distribution that is applicable for volcanic systems characterized by two different eruptive states, where one state with a longer recurrence interval corresponding to periods of low eruption frequency and one state with a shorter recurrence interval corresponding to periods of high eruption frequency. The preferred model for northern Harrat Rahat over the last 180 k.y. uses a long recurrence interval of 4.0 k.y. and a short recurrence interval of 0.22 k.y.

Introduction

The Arabia Plate hosts 16 large Cenozoic harrats (Arabic for lava field), some composites from multiple centers or ages, that stretch approximately 3,000 kilometers (km) from the Gulf of Aden to northeast of the Mediterranean Sea (fig. 1) and cover an area of approximately 180,000 square kilometers (km^2), together composing one of the world's largest alkali basalt volcanic provinces (Coleman and others, 1983; Camp and Roobol, 1989). The largest harrat entirely within the Kingdom of Saudi Arabia, Harrat Rahat is located in the west-central part of the uplifted Arabian Shield. Excellent exposure and minimal erosion make Harrat Rahat a prime example of continental, intraplate volcanism and an outstanding site to investigate changing volcanic flux and composition through the lifetime of a continental basalt field. Harrat Rahat has been the focus of several studies in recent years primarily because it lies between the major cities of Makkah at its south end and Al Madīnah al Munawwarah (hereafter referred to as Al Madīnah) at its north end (fig. 2). A well-documented eruption of the basalt of Al Labah (unit bla; all unit symbols are from Downs and others [2019]) in 1256 C.E. demonstrates that Harrat Rahat continues to be active. This eruption vented approximately 20 km southeast of the Al Madīnah city center,

[1]U.S. Geological Survey.

[2]U.S. Geological Survey, now deceased.

[3]Stanford University.

[4]Saudi Geological Survey.

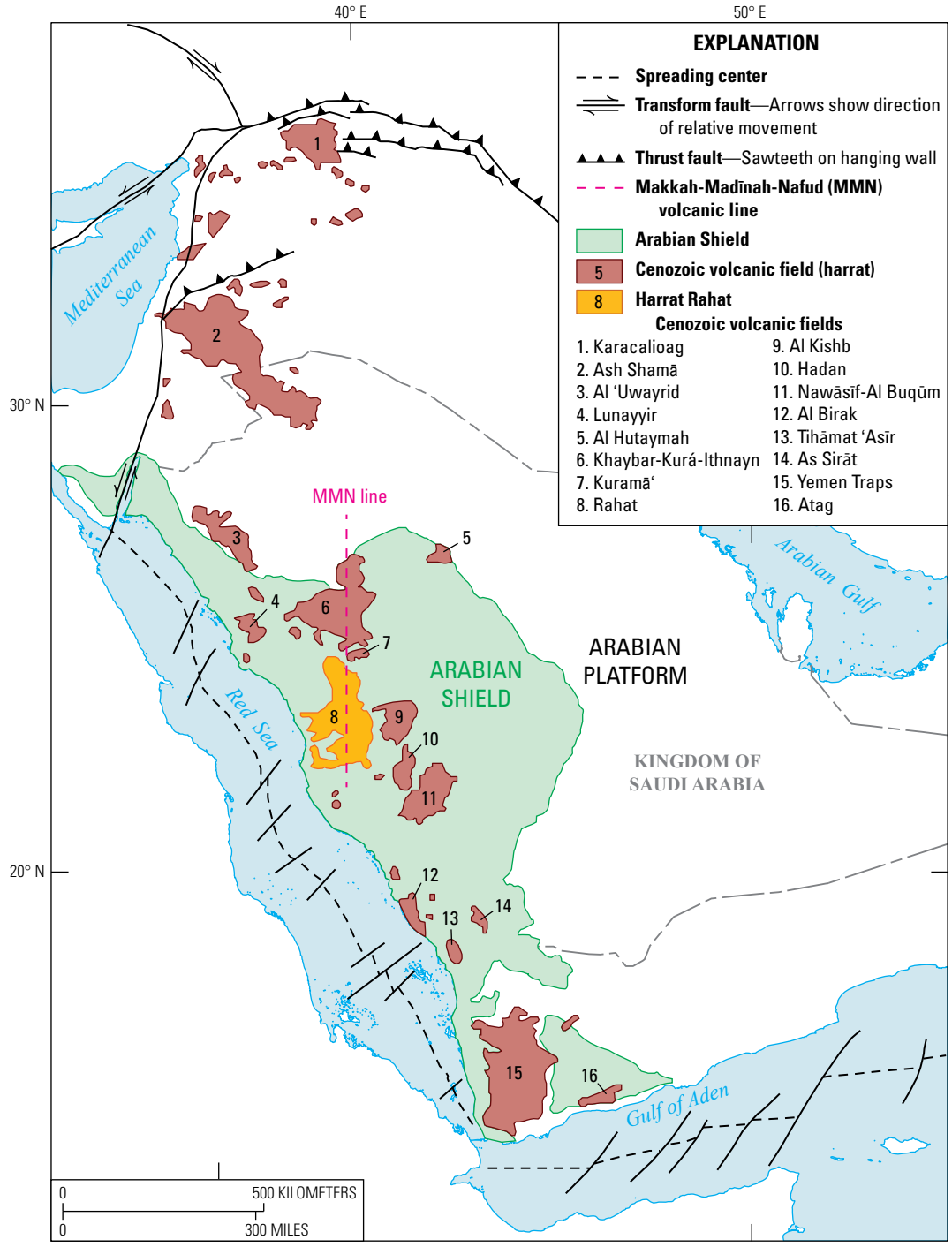

Figure 1. Map of the Kingdom of Saudi Arabia and the surrounding region. Red areas mark the location of Cenozoic volcanic fields (Harrat Rahat shown in orange). The Makkah-Madīnah-Nafud (MMN) volcanic line is a north-trending linear vent system defined by the central axes of Harrat Rahat, Harrat Khaybar, and Harrat Ithnayn (Camp and Roobol, 1992). The Arabian Shield (shown in green) is a region of exposed Neoproterozoic basement rock. Major tectonic features compiled by Stern and Johnson (2010). Locations of Cenozoic volcanic fields are from Coleman and others (1983) and Camp and Roobol (1989).

and lava flows reached within 8 km of the contemporary city center (Camp and others, 1987).

Harrat Rahat consists dominantly of basaltic lavas that compose a 50- to 75-km-wide volcanic plateau extending approximately 310 km north-south, covering an area of approximately 20,000 km^2, and encompassing more than 900 observable vents (Camp and others, 1987; Camp and Roobol, 1989; Runge and others, 2016). Harrat Rahat is a composite of four smaller harrats consisting of, from south to north, Harrat ar Rukhq, Harrat Turrah, Harrat Bani Abdullah, and Harrat Rashid (also known as Harrat al Madīnah; Coleman and others, 1983; Moufti, 1985; Moufti and others, 2013; fig. 2). In this chapter, we refer to Harrat Rashid as northern Harrat Rahat following recent publications (for example, Murcia and others, 2017; Downs and others, 2018, Stelten and others, 2018). Each of these smaller harrats is characterized by an

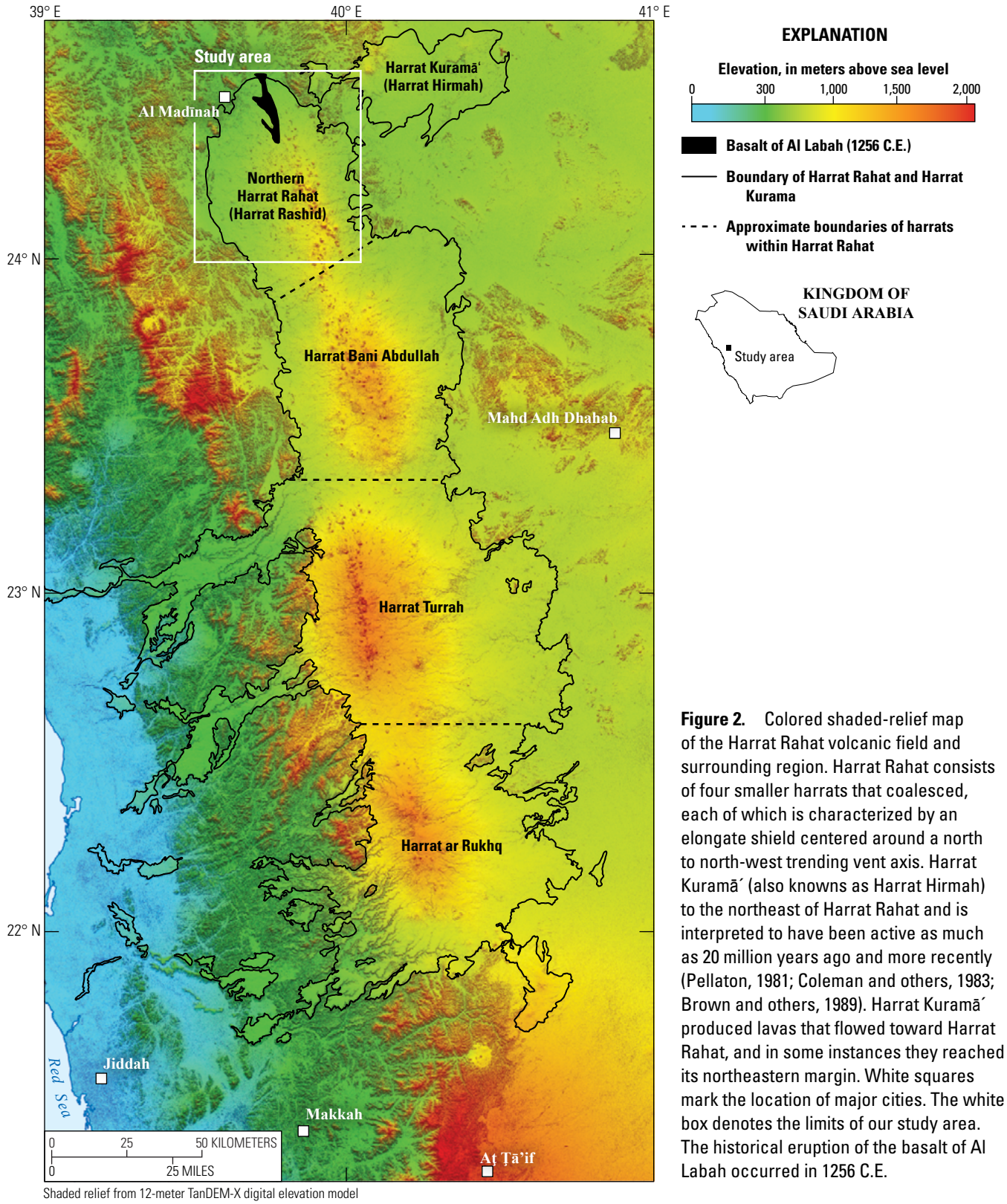

Shaded relief from 12-meter TanDEM-X digital elevation model

Figure 2. Colored shaded-relief map of the Harrat Rahat volcanic field and surrounding region. Harrat Rahat consists of four smaller harrats that coalesced, each of which is characterized by an elongate shield centered around a north to north-west trending vent axis. Harrat Kuramā´ (also knowns as Harrat Hirmah) to the northeast of Harrat Rahat and is interpreted to have been active as much as 20 million years ago and more recently (Pellaton, 1981; Coleman and others, 1983; Brown and others, 1989). Harrat Kuramā´ produced lavas that flowed toward Harrat Rahat, and in some instances they reached its northeastern margin. White squares mark the location of major cities. The white box denotes the limits of our study area. The historical eruption of the basalt of Al Labah occurred in 1256 C.E.

elongate shield centered around a north- to north-northwest-trending, topographically high axis of vents. Initiation of volcanism at each harrat is inferred to have been broadly contemporaneous at approximately 10 million years ago (Ma; Camp and Roobol, 1989; Moufti and others, 2013), although absolute age measurements are sparse. Geologic observations, mapping, and previous geochronological studies demonstrated that the ages of volcanic products of Harrat Rahat generally decrease to the north, and that northern Harrat Rahat (Harrat Rashid) is dominated by the stratigraphically youngest

eruptive products, including a concentration of minimally eroded lava flows and vent complexes (Camp and others, 1987; Camp and Roobol, 1989, 1991; Moufti and others, 2013). Several early studies described the volcanic geology of northern Harrat Rahat and provided important results on the timing and composition of its volcanism (Camp and Roobol, 1989, 1991; Moufti, 1985). However, these early studies lacked the resources and opportunity to perform a detailed evaluation of the eruptive history and compositional evolution for the entirety of northern Harrat Rahat.

This report expands on results and interpretations presented by Stelten and others (2020) by assessing eruption frequency for northern Harrat Rahat. The study benefits from detailed mapping, paleomagnetic analysis, high-precision absolute age determinations, and chemical analyses of volcanic products undertaken as part of a collaborative U.S. Geological Survey (USGS) and Saudi Geological Survey (SGS) study to better understand the eruptive history of this well-exposed continental alkali basalt province. In an early stage of this study, Downs and others (2018) and Stelten and others (2018) assessed the geologic history of certain regions of northern Harrat Rahat, specifically near the city of Al Madīnah and within the Matan volcanic center (fig. 3), but did not evaluate the northern Harrat Rahat as a whole. We expand on prior work and present 93 $^{40}Ar/^{39}Ar$ ages and 6 ^{36}Cl surface-exposure ages from Stelten and others (2020) for volcanic deposits throughout northern Harrat Rahat, making northern Harrat Rahat one of the best dated mafic volcanic fields in the world. These data are integrated with 57 $^{40}Ar/^{39}Ar$ eruption ages and 5 ^{36}Cl surface-exposure ages reported by Downs and others (2018) and Stelten and others (2018), and with 691 whole-rock analyses for northern Harrat Rahat from Downs (2019). Together, these age and geochemical determinations were used in preparation of a new geologic map of northern Harrat Rahat that supports this report (Downs and others, 2019; Robinson and Downs, 2023), in which more than 200 distinct eruptive units are identified and placed in stratigraphic context. In this paper, we build upon previous studies by integrating these eruption ages, whole-rock geochemistry, and field relations to (1) describe the eruptive history for the entirety of northern Harrat Rahat from 1.2 Ma to present, (2) characterize the timing and episodicity of volcanism, (3) estimate the volume of magma produced through time, (4) develop a petrologic model for the spatial and compositional evolution of the volcanic field through time, and (5) reevaluate the volcanic recurrence interval in northern Harrat Rahat. Our new constraints provide important insights into the development and compositional evolution of continental alkali basalt provinces that are applicable to other continental basalt fields in Saudi Arabia and worldwide.

Geologic Background

Broadly, Cenozoic volcanism on the Arabia Plate can be divided into three stages (Coleman, 1993; Bosworth and others, 2005; Calvert and Sisson, 2023). Initial volcanism at about 30 Ma, prior to the opening of the Red Sea, emplaced the voluminous alkali, transitional, and tholeiitic flood basalts of Ethiopia, Sudan, and southwest Yemen and is widely interpreted as driven by arrival of a mantle plume beneath what is now the Afar depression. The second period of magmatism, near 25 Ma, saw emplacement of regional dikes of tholeiitic basalt parallel and adjacent to the Red Sea's east margin, accompanied by early rifting and emplacement of scattered, now deeply eroded harrats. The Yemen Trap series consists of alkali and transitional basalts plus rhyolites—not tholeiitic basalts. The Ethiopian Traps consist of alkali, transitional, and tholeiitic basalts. The 25 Ma initial rift basalts are tholeiites but the earlier basalts are generally not (fig. 1; Almond, 1986a,b; Camp and Roobol, 1989). In contrast, volcanism after 15 Ma is dominantly alkalic, and most volcanism occurred along the Makkah-Madīnah-Nafud volcanic line (fig. 1), which is defined by the north-trending linear vent systems of Harrats Rahat, Khaybar, and Ithnayn, with smaller and more alkaline fields flanking to the southeast and northwest (Coleman and others, 1983; Camp and Roobol, 1992). The driving force behind volcanism in the younger (younger than 15 Ma) harrats remains unclear, but has variously been attributed to (1) uplift and extension associated with impingement of the Afar plume on the lithosphere (Almond, 1986b; Camp and Roobol, 1989, 1992), (2) melting related to Red Sea rifting and left-lateral movement along the Aqaba-Dead Sea Transform fault boundary (Coleman and McGuire, 1988; Stein and Hofmann, 1992; Bosworth and others, 2005; Moufti and others, 2012), or (3) regional lithospheric thinning coupled with northward flow of hot asthenosphere related to the Afar plume (Duncan and others, 2016). Isotopic and geochemical studies of northern Harrat Rahat (Salters and others, 2023; Sisson and others, 2023) indicate low-degree melting dominantly of depleted asthenospheric upper mantle with a subordinate (20–30 percent) component of, or similar to, the Afar mantle plume. Thus, although the driving force behind volcanism over the past 15 million years (m.y.) is unclear, it is generally agreed that volcanism in the Arabian harrats is driven by decompression melting.

Volcanism Throughout Harrat Rahat

The timing of volcanism throughout Harrat Rahat has been determined by several broad-scale studies (Camp and Roobol, 1989, 1991; Moufti and others, 2013). On the basis of field observations and aerial imagery, Camp and Roobol (1989, 1991) defined three major volcanic groups for the Harrat Rahat volcanic field: Shawahit, Hammah, and Madinah basalts. These volcanic groups are separated by disconformities characterized by erosional incision and mature lateritic surfaces. Based on a compilation of 25 K-Ar ages (Pellaton, 1981; Coleman and others, 1983; Camp and Roobol, 1989), Camp and Roobol (1989, 1991) assigned ages of 10 to 2.5 Ma for the Shawahit basalt, 2.5 to 1.7 Ma for the Hammah basalt, and 1.7 Ma to present for the Madinah basalt. The Shawahit and Hammah basalts are widely exposed in Harrat ar Rukhq, Harrat Turrah, and Harrat Bani Abdullah (fig. 2), the southern three-quarters of Harrat Rahat. The northern quarter of Harrat Rahat is dominated

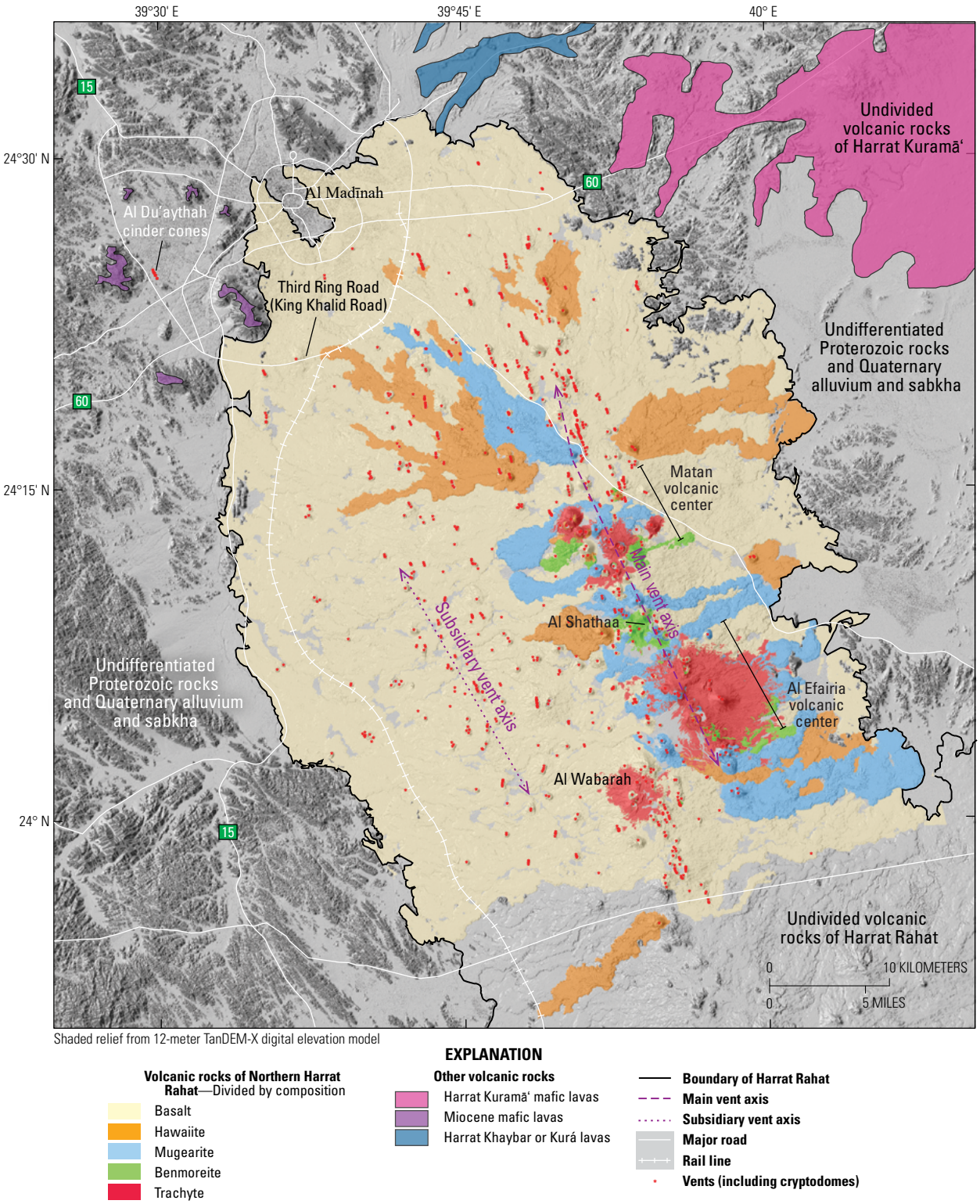

Figure 3. Map of the study area in northern Harrat Rahat. Gray areas have not been mapped. Northern Harrat Rahat eruptive units are displayed by composition. Red dots represent known vent locations and include non-erupted cryptodomes as well as nested and aligned craters and scoria cones from single eruptions. The location and trends of the main vent axis and the subsidiary vent axis are defined by constructional relief and abundant, aligned volcanic vents. The locations of the Matan volcanic center and Al Efairia volcanic center, which lie along the main vent axis and host the majority of evolved volcanism in northern Harrat Rahat, and the explosive eruption of the benmoreite of Al Shathaa (unit osa) are indicated. Also shown are the locations of older volcanic deposits located around Harrat Rahat, including mafic lavas derived from Harrat Kuramā´, Harrat Khaybar, and Miocene mafic lavas that cap hills of Proterozoic basement rock at the northwest end of Harrat Rahat (Downs and others, 2019; Robinson and Downs, 2023). Figure modified from Downs and others (2019).

by the Madinah basalt, which implies that volcanism either migrated to the north or ceased in the south over time.

Volumetrically, Harrat Rahat is dominated by basalt and hawaiite (greater than 95 percent) with minor amounts of mugearite, benmoreite, and trachyte (Camp and Roobol, 1989). Basalt and hawaiite are present throughout the entire history of Harrat Rahat, but more evolved eruptive products such as mugearite, benmoreite, and trachyte are absent in the Shawahit basalt (that is, volcanic products older than 2.5 Ma) and are most abundant in the Madinah basalt, particularly in northern Harrat Rahat.

Northern Harrat Rahat

The study area in northern Harrat Rahat spans about 75 km from just north of the Al Madīnah metropolitan area south-southeast to a major oil and gas pipeline system that crosses the volcanic field close to latitude 24° N. Here the field is approximately 55 km wide, flanked on the east and west sides by Proterozoic basement rocks overlain by Quaternary sediments (figs. 2, 3). This area contains the greatest abundance of morphologically young lava flows, domes, maars, tuff rings, and craters in Harrat Rahat (Moufti, 1985; Camp and Roobol, 1989, 1991; Downs and others, 2018, 2019; Stelten and others, 2018). Recently, Downs and others (2019) and Robinson and Downs (2023) identified 239 distinct eruptive units in northern Harrat Rahat, not including isolated vents that are not correlated with exposed volcanic deposits. In some cases, eruptions in Harrat Rahat occur through multiple aligned vents (Runge and others, 2014), and the number of eruptive units presented by Downs and others (2019) and Robinson and Downs (2023) accounts for this observation. The majority of eruptive units are basaltic lavas that erupted from a broadly north-northwest-trending concentration of vents (hereafter referred to as the main vent axis) that thereby constructed the topographic crest of the volcanic field, standing as high as 400 meters (m) above adjacent Proterozoic rock exposures (fig. 3). This main vent axis lies in the eastern third of northern Harrat Rahat, about 15 to 20 km from its eastern margin and has a width of approximately 6 to 10 km (fig. 3). An approx-imately parallel but more diffuse concentration of vents (hereafter referred to as the subsidiary vent axis) is situated approximately 10 km to the west of the main vent axis and at lower elevations, commonly about 200 m above Proterozoic basement rock (fig. 3; El Difrawy and others, 2013). Prior to this study, the relative age of volcanism along these vent axes was undetermined.

All intermediate-to-evolved volcanism (that is, mugearite, benmoreite, and trachyte) issued from the main eastern vent axis, predominantly from two volcanic centers hereafter referred to as the Matan and Al Efairia volcanic centers (names from Moufti, 1985; fig. 3). Trachyte also erupted from Al Wabarah, located approximately 8 km southwest of the Al Efairia volcanic center's main vent complex. The Matan and Al Efairia volcanic centers erupted magmas that ranged from basalt to trachyte. In most areas, trachytes are among the stratigraphically youngest eruptive products in northern Harrat Rahat (Moufti, 1985; Camp and Roobol 1989, 1991; Stelten and others, 2018). Previous researchers interpreted chemical variations in Harrat Rahat eruptive products (that is, basalt to trachyte) to represent crystallization differentiation of mantle-derived basalts with little to no assimilation of Proterozoic crust (Camp and Roobol, 1989; Moufti and others, 2012; Stelten and others, 2018). Limited crustal assimilation is consistent with the similarity of the isotopic compositions of intermediate and trachytic units to mafic units (Moufti and others, 2012; Salters and others, 2023) and with geochemical studies at other Arabian harrats (Shaw and others, 2003; Duncan and others, 2016).

Several prior studies have attempted to determine the age of volcanism in northern Harrat Rahat. Camp and Roobol (1989, 1991) assigned the majority of eruptive products in northern Harrat Rahat to the Madinah basalt (1.7 Ma to 1256 C.E.), which they subdivided into seven subunits (units $Qm_{1–7}$) based on the degree of erosion, the abundance and size of loess-filled depressions across their surfaces, and Landsat imagery, as well as archeological arguments and historical records for the youngest subunits (units Qm_6 and Qm_7). On the basis of these criteria, they suggested that most eruptions occurred between 1.7 and 0.6 Ma (subunits $Qm_{1–3}$). Camp and Roobol (1989, 1991) interpreted at least six eruptions in northern Harrat Rahat (subunits Qm_6) as post-Neolithic (that is, less than 6,000 years before present; Crassard and others, 2013) based on geological and archeological arguments. Two eruptions were identified as historical (unit Qm_7), including the well-documented eruption of the basalt of Al Labah (unit bla) at 1256 C.E. (described in Wafā' Al-Wafā' Bi Akhbār Dār Al-Muṣṭafā by Al-Samhūdī, 1488) and a line of four small cinder cones with two short basaltic lava flows (collectively, the basalt of Al Du'aythah, [unit bdu]) on the west margin of Al Madīnah that were provisionally assigned an age of 641 C.E. (Camp and Roobol, 1989). Moufti and others (2013) further investigated the eruptive history of northern Harrat Rahat by providing 25 $^{40}Ar/^{39}Ar$ ages for eruptive products from the $Qm_{1–6}$ subunits. Although they generally supported the age groups proposed by Camp and Roobol (1989, 1991), the $^{40}Ar/^{39}Ar$ data demonstrated significant overlap in the ages of the different Madinah basalt morphologic subunits.

On the basis of estimates of the number of volcanic vents in northern Harrat Rahat (including estimates of buried vents) and broad estimates of the age of Harrat Rahat volcanic deposits available at the time, El Difrawy and others (2013) estimated the recurrence interval of eruptions in northern Harrat Rahat to be between 70 and 13,300 years, with a best estimate of 3,300 years, Similarly, Runge and others (2014) evaluated the recurrence interval to between 3,900 and 13,300 years for the whole of Harrat Rahat. The broad range of estimated recurrence intervals presented by these previous studies is largely because of a lack of age control on volcanic products in northern Harrat Rahat and highlights the need for improved geochronology.

In the initial stages of this study, Downs and others (2018) and Stelten and others (2018) obtained new high-precision $^{40}Ar/^{39}Ar$ ages and ^{36}Cl surface-exposure ages for the northwestern terminus of Harrat Rahat, within and proximal to the city of Al Madīnah, and for the Matan volcanic center, respectively (fig. 3). Downs and others (2018) demonstrated that volcanism near Al Madīnah occurred at least from 1,014±14 ka to 1256 C.E., and they importantly demonstrated that the basalt of Al Du'aythah (unit bdu), previously assigned the provisional age of 641 C.E., erupted at 13.3±1.9 ka. Stelten and others (2018) demonstrated that volcanism within the Matan volcanic center (fig. 3) occurred from at least 1,112.1±17.6 ka to 17.6±1.8 ka and that young trachyte eruptions were preceded by eruption of mafic (basalt and hawaiite) and intermediate (mugearite and benmoreite) magmas. New age data provided by both Downs and others (2018) and Stelten and others (2018) accord with exposed superposition but are commonly inconsistent with eruption ages that would be inferred from the prior age group assignments of Camp and Roobol (1989, 1991). The present study expands on previous work by providing age, geochemical data, and field relations for the entirety of northern Harrat Rahat.

Physical Characteristics of Eruptive Products in Northern Harrat Rahat

Basalt, hawaiite, and mugearite magmas mainly erupted in Hawaiian, Strombolian, and Vulcanian styles, forming scoria cones and emplacing lava flows that reach greater than 20 km in length (Moufti, 1985; Camp and others, 1987; Camp and Roobol, 1989, 1991; Dietterich and others, 2018; Downs and others, 2019; Robinson and Downs, 2023). In some instances, mafic magmas interacted with groundwater resulting in phreatomagmatic eruptions that constructed maars and tuff rings (Moufti, 1985; Murcia and others, 2015). Mafic scoria and ashfall deposits are rarely preserved, likely because of their small volumes, coupled with a dry, unvegetated environment where aeolian and fluvial processes quickly disperse unconsolidated material. The only well-preserved mafic scoria-fall deposit resulted from fire fountaining and low-level Strombolian activity during the 1256 C.E. eruption of the basalt of Al Labah (unit bla), and this tephra is preserved only as far as 5 km from its vent (Kawabata and others, 2015). Benmoreite and trachyte magmas had high viscosities on eruption, forming domes and small lava flows. Collapse of domes and spines formed pyroclastic flows of poorly vesiculated pumice and lava blocks that flowed as far as 7 km from their sources. In some cases, Peléan and Vulcanian explosions associated with dome emplacement excavated kilometer-scale craters. Additionally, rare cases of sub-Plinian eruptions of benmoreite and trachyte are inferred to have occurred, resulting in craters and sub-pumiceous pyroclastic-flow deposits that extend continuously as far as 7 km from their sources (Moufti, 1985; Camp and Roobol, 1989; Stelten and others, 2018; Downs and others, 2019; Robinson and Downs, 2023).

Methods

Whole-Rock Chemical Analyses

Whole-rock samples were collected throughout the map area as part of the SGS-USGS mapping effort (Downs and others, 2019). Major-oxide and trace-element concentrations were measured for 691 whole-rock samples from northern Harrat Rahat by X-ray fluorescence (XRF) and by inductively coupled plasma mass spectrometry (ICP-MS) at the GeoAnalytical Laboratory at Washington State University in Pullman, Washington, United States. Geochemical data are presented in the USGS data repository by Downs (2019). Vug-filling secondary minerals, consisting of zeolites, gypsum, and rarely calcite, are widespread in harrat volcanic rocks, even in samples with well-preserved non-hydrated glass, becauseof repeated wetting by brief but intense rain followed by rapidevaporation. Zeolites and gypsum were removed by extended and repeated sonication of crushed rock fragments in warm deionized water, but traces of calcite may remain in some samples. Samples with original analytical totals less than 94 weight percent, high loss on ignition, or visible residual secondary minerals were not used (Downs and others, 2019). Subsets of the analyses and additional preparation methods are reported by Downs and others (2018), Stelten and others (2018), and Dietterich and others (2018).

$^{40}Ar/^{39}Ar$ Dating

One hundred and fifty rock samples were collected throughout the study area for geochronologic analysis via the $^{40}Ar/^{39}Ar$ method as part of the SGS-USGS mapping effort. Results for 93 of these samples are presented in this chapter, reproduced from Stelten and others (2020), whereas data for the remaining 57 samples were presented by Downs and others (2018, 2023a) and Stelten and others (2018, 2023). Dense samples with a crystalline groundmass were chosen for analysis. For most samples, groundmass separates were analyzed. To prepare groundmass separates, the samples were crushed via roller mill, sonicated under deionized water, and sieved to 250–355 micrometers (μm). Groundmass was separated from phenocryst phases using a Frantz magnetic separator and careful handpicking under a binocular microscope. For trachyte and some benmoreite samples, feldspar separates (anorthoclase or sanidine) were prepared from the 250–355 μm size fraction of crushed whole-rock samples by standard magnetic and density separation techniques. Prior to irradiation, the feldspar separates were sonicated in cold 8 percent hydrofluoric acid to remove any glass adhering to the crystals and then were sonicated in deionized water. The sanidine crystals were then inspected under a binocular microscope to ensure that no fluoride compounds were deposited on the sanidine crystals. Approximately 100 to 150 milligrams (mg) of material were prepared for each groundmass separate, and approximately 50 to 75 mg of material were prepared for each feldspar separate.

Groundmass and feldspar separates were irradiated along with Bodie Hills sanidine (9.7946±0.0033 Ma, equivalent to Fish Canyon sanidine at 28.0985±0.0126 Ma; Fleck and others, 2019) for 1 hour in the central thimble of the USGS Training, Research, Isotopes, General Atomics (TRIGA) reactor in Denver, Colorado, United States (Dalrymple and others, 1981) at a power level of 1 megawatt. For incremental heating analysis of groundmass and bulk feldspar separates, the argon was extracted in discrete temperature steps using a molybdenum crucible in a custom resistance furnace attached to a MAP 216 mass spectrometer at the USGS Menlo Park facility. Prior to measurement of argon isotopic composition,

Table 1. Summary of $^{40}Ar/^{39}Ar$ eruption ages for northern Harrat Rahat.

[Unit symbols from Downs and others (2019) and Robinson and Downs (2023). When calculating weighted mean ages for a given unit, replicate analyses of a single sample were averaged first and then the ages for different samples from the same unit were averaged. Where available, weighted mean ages are used as the eruption age. For samples analyzed prior to July 2016, mass discrimination was calculated assuming $^{40}Ar/^{36}Ar_{atmosphere}$ = 295.5±0.5 (Steiger and Jäger, 1977), whereas for samples analyzed after July 2016 mass discrimination was calculated assuming $^{40}Ar/^{36}Ar_{atmosphere}$ = 298.56±0.31 (Lee and others, 2006). The change in the assumed $^{40}Ar/^{36}Ar$ of atmospheric argon does not result in a bias in ages because both monitors and unknowns from each irradiation were calculated in the same manner. The assumed atmospheric argon composition used for each analysis is indicated in the table. Ages were calculated using the decay constants recommended by Steiger and Jäger (1977). Ages were calculated relative to Bodie Hills sanidine at 9.7946 million years ago (Ma; equivalent to Fish Canyon sanidine at 28.0985±0.0126 Ma). $^{40}Ar/^{36}Ar_i$ isochron intercept. Abbreviations: GM, groundmass; An, anorthoclase; San, sanidine; IH, incremental heating; ka, thousand years ago; LF, laser total fusion; MSWD, mean square of weighted deviates; T, temperature; °C, degree Celsius; %, percent]

Unit symbol	Sample	Location		Material-method	Plateau or weighted mean		Isochron			^{39}Ar, in % [T range, in °C]	$^{40}Ar^*$, in %
		Easting	Northing		Age ±1σ (ka)	MSWD	Age ±1σ (ka)	MSWD	$^{40}Ar/^{36}Ar_i$ (±2σ)		
badh	R17AC132	582574	2656022	GM-IH	235.2±11.4	1.45	208.9±16.9a	1.02	301.3±3[b]	74 [775–1,375]	8.8
bag	R15MS028	585909	2693021	GM-IH	216.8±13.5[a]	1.63	1.8±122.5	1.29	302.7±9.3[c]	97.6 [550–1,200]	2.4
bag	R15MS029	587097	2695017	GM-IH	222.5±10.6[a]	0.50	328.7±101.4	0.36	287.2±17.8[c]	38.6 [550–950]	5.4
				Weighted mean age (±1σ)	220.3±8.3						
bai	R16DD205	563860	2701588	GM-IH	560.4±8.4	1.93	546.2±9.6[a]	1.28	301.4±3.2[c]	94.8 [625–1,250]	28.4
bam1	R15MS003	583569	2682186	GM-IH	264±7.2	2.05	252.2±6.8[a]	1.15	300.6±1.7[b]	100 [550–1,300]	14.1
bar	R14AC69	590358	2681448	GM-IH	130.3±5[a]	0.60	132.7±7.5	0.65	295.0±2.5[c]	90.8 [550–1,100]	7.9
basu	R16MS057	584487	2658457	GM-IH	444.4±6.8[a]	1.53	447.4±10	1.66	297.7±3.8[b]	96.6 [550–1,275]	21.4
basu	R16MS089	590006	2659273	GM-IH	471.6±9.7[a]	0.89	457.3±20.4	0.93	299.6±3.4[b]	100 [625–1,375]	12.4
				Weighted mean age (±1σ)	453.4±12.8						
bba	R14TS84	583592	2676619	GM-IH	674.7±7.2[a]	0.94	668.4±22.8	1.05	295.9±3.5[c]	99.4 [550–1,275]	13.7
bbd	R16DD216	566681	2697072	GM-IH	223.4±8.6[a]	0.24	220.4±42.4	0.28	299±13.9[b]	62.3 [550–1,125]	10.6
bd1	R14AC18	592242	2679233	GM-IH	717.7±12.2[a]	0.64	724.3±20.3	0.68	295.3±1.2[c]	100 [550–1,250]	8.8
bd3	R14AC65	603272	2670061	GM-IH	318.1±7.1[a]	2.05	302±11.7	1.68	299.8±6.3[c]	90.3 [550–1,200]	23.2
bd3	R14AC66	601665	2671983	GM-IH	300±6.1[a]	1.00	298.5±13	1.19	295.7±3.6[c]	74.9 [600–1,125]	12.9
				Weighted mean age (±1σ)	307.7±4.6						
bda	R14TS130	580964	2672737	GM-IH	223±18.9[a]	1.47	162.9±28.7	0.86	298.0±2.3[c]	99.3 [550–1,300]	3.2

Table 1. Summary of $^{40}Ar/^{39}Ar$ eruption ages for northern Harrat Rahat.—Continued

Unit symbol	Sample	Location		Material-method	Plateau or weighted mean		Isochron			^{39}Ar, in % [T range, in °C]	$^{40}Ar^*$, in %
		Easting	Northing		Age ±1σ (ka)	MSWD	Age ±1σ (ka)	MSWD	$^{40}Ar/^{36}Ar_i$ (±2σ)		
bdr	R15TS193	566704	2670155	GM-IH	295±15.4	2.91	232.7±15.9[a]	0.98	305.2±3.1[b]	100 [550–1,350]	10.2
bdw	R16DD221	573572	2700545	GM-IH	25.6±16.2[a]	1.70	87.7±47.3	1.38	293.3±8.9[c]	49.8 [550–875]	1.0
bdy	R16MS080	580828	2690769	GM-IH	168.1±9.1	1.73	139.2±11.3[a]	0.73	301.8±2.3[b]	100 [550–1,350]	5.9
bg3	R14DS1	588701	2675770	GM-IH	1,112.1±17.6[a]	1.01	1,118.8±49.2	1.17	295.0±6.2[c]	81.2 [550–1,175]	18.8
bh10	R16MS075	591473	2691621	GM-IH	137.3±11.3[a]	0.45	121.4±52.8	0.51	299.8±9.7[b]	71.1 [550–1,125]	3.8
bh82	R15MS041	579664	2705816	GM-IH	507.4±38.3[a]	0.72	445.1±246.4	0.83	299.2±5.9[b]	90.6 [625–1,250]	1.8
bh83	R15MS021	569465	2675983	GM-IH	505.1±10.3[a]	1.58	459.4±32.2	1.44	300.0±7.4[c]	100 [550–1,250]	15.1
bh86	R15TS197	560403	2669086	GM-IH	319.6±13.2	1.40	255.6±30.5[a]	0.86	302.2±3.7[b]	87.4 [700–1,250]	5.9
bh86	R16MS078	564237	2668133	GM-IH	349.1±7.9	1.08	308.2±26.7[a]	0.89	302.8±6.2[b]	97.7 [625–1,250]	11.8
				Weighted mean age (±1σ)	285.4±20.1						
bh89	R15TS161	574371	2689742	GM-IH	1,014±14[a]	0.28	988±42	0.23	299.9±4.6[b]	57.955 [900–1,200]	16.3
bhb	R15MS031	589420	2699949	GM-IH	246.4±25[a]	1.51	350.7±128.4	1.60	290.9±13.0[c]	43.8 [725–1,100]	3.5
bhg	R15MS037	561322	2703723	GM-IH	382.5±5.8[a]	1.17	372.5±19.7	1.33	297.0±6.5[c]	75.1 [750–1,225]	17.3
bhu	R15MS026	562501	2692863	GM-IH	285.1±6.6[a]	0.57	283.6±9.1	0.71	295.6±2.4[c]	86.4 [550–1,125]	15.3
bhy	R15TS202	593341	2676141	GM-IH	235.1±7.5[a]	1.43	233.5±20.6	1.63	295.6±5.8[c]	99.7 [550–1,250]	9.7
bja	R17AC125	574946	2665947	GM-IH	738.5±7.3	1.51	698.1±16[a]	0.91	303.2±3.7[b]	100 [550–1,375]	22.6
bjab	R16MS053	568611	2675106	GM-IH	435.6±16.5	3.90	324.7±29.3[a]	1.51	309.2±6.1[b]	100 [550–1,400]	12.6
bjn	R16MS063	599442	2669428	GM-IH	512.8±9.3[a]	0.95	482.9±19.5	0.74	301.5±3.8[b]	90.3 [625–1,200]	15.6
bjr	R15MS024	571129	2671928	GM-IH	207.3±8.4[a]	1.40	209.9±39.4	1.60	295.2±8.8[c]	78 [775–1,350]	6.7
bka	R14TRO158	580435	2711222	GM-IH	225.7±17.1	2.71	144.6±19.6[a]	0.19	306.8±3.9[b]	100 [550–1,300]	7.3
blqa	R17AC139	579996	2711994	GM-IH	196.9±10.3[a]	0.22	213.8±31.2	0.21	296.6±7.5[b]	71.6 [550–1,150]	7.1
blsa	R17TS234	579478	2701502	GM-IH	346.9±9.9[a]	0.68	345.5±22.5	0.73	298.6±4[b]	99.6 [550–1,225]	10.0
blsl	R16MS073	598390	2688370	GM-IH	228.6±12[a]	0.97	241±57.5	1.07	297.4±11.5[b]	98 [550–1,250]	6.6
bm1	R15MS042	585621	2675281	GM-IH	230.7±4.4[a]	1.07	226.1±9.1	1.22	296.9±6.4[c]	89.3 [550–1,125]	22.3

Table 1. Summary of $^{40}Ar/^{39}Ar$ eruption ages for northern Harrat Rahat.—Continued

Unit symbol	Sample	Location		Material-method	Plateau or weighted mean		Isochron			^{39}Ar, in % [T range, in °C]	$^{40}Ar^*$, in %
		Easting	Northing		Age ±1σ (ka)	MSWD	Age ±1σ (ka)	MSWD	$^{40}Ar/^{36}Ar_i$ (±2σ)		
bmat	R15MS001a	571467	2698610	GM-IH	136.7±7.6[a]	0.46	148.4±12.4	0.32	294.1±2.8[c]	94.3 [550–1,200]	5.6
bmg	R15TS169	569252	2686959	GM-IH	570±5.9[a]	1.05	546.3±22.7	1.02	298.6±6.6[c]	86.7 [700–1,200]	20.9
bmk	R16MS059	605978	2654449	GM-IH	315.9±9.3	1.56	261.3±19.1[a]	0.51	304.4±4.4[b]	100 [550–1,275]	10.4
bml	R15DD030	573401	2663207	GM-IH	225±7.6[a]	1.30	220.4±15.1	1.49	299±3.2[b]	77 [625–1,200]	8.1
bml	R14TRO140	571165	2664261	GM-IH	218.1±9.1[a]	0.13	223±43.9	0.16	297.9±13.6[b]	50.5 [700–1,100]	9.2
				Weighted mean age (±1σ)	222.2±5.8						
bmsm	R15DD057	576765	2668872	GM-IH	594.7±7.1	1.63	552.8±19.6[a]	1.13	304.7±6.4[b]	94.2 [550–1,250]	23.3
bmu	R15MS039	564637	2708368	GM-IH	344.7±4.8[a]	0.95	338.5±6.1	0.72	297.0±2.1[c]	99.6 [550–1,375]	22.4
bmy	R15DD051	578923	2667891	GM-IH	684.4±9.6	1.17	660.4±13.4[a]	0.37	305.3±6.4[b]	57.9 [750–1,150]	40.5
bna	R15MS040b	580528	2711526	GM-IH	162.9±11.1[a]	1.49	165.1±28.9	1.63	298.4±3.4[b]	100 [550–1,250]	2.9
bni	R15DD020	587627	2686341	GM-IH	402.5±15.4[a]	1.86	396±43.6	2.16	298.8±4.6[b]	92.7 [550–1,200]	6.0
bnu	R15TS155	569546	2694630	GM-IH	131.2±8.3[a]	1.45	137.2±13.6	1.56	294.9±2.0[c]	99.3 [550–1,250]	3.8
bpr	R14TS101	576726	2703121	GM-IH	378.8±10[a]	1.53	363.1±13.3	1.29	296.7±1.8[c]	98.8 [625–1,350]	10.6
bqg	R15MS022	570114	2676455	GM-IH	214.9±7.2[a]	1.11	168.7±36.9	1.01	298.6±5.6[c]	100 [550–1,250]	4.7
bqg	R16MS055	573186	2680951	GM-IH	286.3±13.5	2.61	218.7±23.7[a]	1.31	304.2±4.2[b]	98.8 [550–1,275]	8.5
				Weighted mean age (±1σ)	215.2±6.9						
brg	R14TS45	604131	2663642	GM-IH	542±6.3[a]	1.19	535.3±8	1.10	296.7±2.3[c]	89.5 [700–1,275]	25.9
brg	R15DS174	603762	2664722	GM-IH	550±14.9[a]	1.86	506.9±32.8	1.73	301.8±5.2[b]	90.642 [550–1,200]	14.0
brg	R15DS174	603762	2664722	GM-IH	544.3±22[a]	1.60	474.4±107	1.84	302.4±13.2[b]	48.8 [950–1,200]	9.3
				Weighted mean age (±1σ)	543.3±5.6						
brh	R16DD222	566408	2695456	GM-IH	411.5±5.9[a]	0.90	409.9±20.8	1.01	298.7±6.5[b]	100 [550–1,400]	16.5
bri	R15DD035	569955	2655799	GM-IH	438.9±21[a]	1.01	314.1±357.8	1.12	300.5±12.3[b]	89.7 [775–1,300]	2.3
bsa	R14AC84	592366	2671105	GM-IH	288.8±19.6[a]	2.27	236.4±36.7	1.84	299.5±5.9[c]	63.4 [550–1,150]	7.5
bsah	R16MS058	599791	2654219	GM-IH	401.6±9.8[a]	1.51	403±14.4	1.71	298.4±2[b]	97.8 [550–1,250]	11.2
bsas	R14AC68	596910	2677863	GM-IH	115.3±7.5[a]	1.78	115.5±14.6	2.04	295.4±4.1[c]	91 [550–1,150]	6.0

Table 1. Summary of $^{40}Ar/^{39}Ar$ eruption ages for northern Harrat Rahat.—Continued

Unit symbol	Sample	Location		Material-method	Plateau or weighted mean		Isochron			^{39}Ar, in % [T range, in °C]	$^{40}Ar^*$, in %
		Easting	Northing		Age ±1σ (ka)	MSWD	Age ±1σ (ka)	MSWD	$^{40}Ar/^{36}Ar_i$ (±2σ)		
bsd	R14DS53	589500	2664469	GM-IH	584.5±10.4[a]	0.13	565.4±133.6	0.17	300.2±25.9[b]	57.6 [925–1,175]	14.3
bsf	R15TS191	568962	2671123	GM-IH	217.5±6.7[a]	0.99	219.1±16.2	1.17	298.2±5.8[b]	95.5 [700–1,245]	10.4
bsh	R15MS020	563271	2698094	GM-IH	206.5±8.1[a]	0.97	198.6±12.9	1.02	296.1±1.8[c]	97.5 [550–1,300]	5.4
bsh	R15MS020	563271	2698094	GM-IH	186.6±7[a]	0.81	187.8±11.6	0.90	295.4±1.7[c]	96.8 [550–1,275]	4.6
bsh	R15MS020	563271	2698094	GM-IH	184.9±7.1[a]	0.98	188.8±11.3	1.06	295.1±1.7[c]	100 [550–1,425]	5.2
				Weighted mean age (±1σ)	191.5±4.2						
bsi	R14TS33	584610	2681045	GM-IH	138.1±17.2[a]	2.15	67.5±110.3	2.50	302.5±25.4[c]	45.7 [550–1,050]	4.5
bsi	R14TS33	584610	2681045	GM-IH	158.7±12.1[a]	1.51	217.3±35.3	1.12	287.4±10.4[c]	47.6 [550–1,075]	7.1
				Weighted mean age (±1σ)	151.9±9.9						
bss	R16MS085	580873	2671355	GM-IH	461.9±4.9[a]	1.18	458.9±5.9	1.22	299.2±1.6[b]	94.5 [700–1,275]	23.7
bssu	R17AC133	583595	2656608	GM-IH	324.8±7.3	0.74	313.9±11.3 [a]	0.66	300±2.6[b]	99.8 [550–1,325]	13.7
bsu	R15JR010	571544	2703271	GM-IH	86.8±7.6[a]	1.70	84.2±22.9	2.20	296.0±13.9[c]	79.3 [550–950]	7.9
bsu	R16DD200	569641	2705169	GM-IH	84.3±8.6[a]	1.38	69.2±13.8	1.33	300.6±3.7[b]	99.3 [550–1,275]	4.3
				Weighted mean age (±1σ)	85.7±5.7						
bsy	R16MS054	570599	2678890	GM-IH	296.2±12.6	2.23	236.2±29.2[a]	1.50	304.7±6.7[b]	97.6 [625–1,375]	10.2
btw	R15DD145	572740	2679533	GM-IH	769.6±42.4	10.22	497.5±37.5[a]	1.14	305.9±2.2[c]	96.7 [550–1,225]	6.4
bun	R16DD192	556167	2694396	GM-IH	122.3±7.3	1.34	105±8.6[a]	0.43	301.2±2.1[c]	98.1 [550–1,200]	6.5
buph	R17TS220	577151	2666602	GM-IH	551.8±8.7	1.74	510.8±29.4[a]	1.57	303.9±8.4[b]	100 [550–1,300]	20.5
buqa	R15AC112	577900	2710277	GM-IH	1,086±14	3.31	961±45[a]	1.97	313.8±11.8[b]	93.4 [700–1,350]	32.3
buqa	R17AC140	579498	2710243	GM-IH	1,080±6	1.13	1,073±8[a]	0.97	299.7±2.1[b]	100 [550–1,300]	40.0
				Weighted mean age (±1σ)	1,069.6±19.3						
bur	R15DD002	567045	2708609	GM-IH	401.8±6.3[a]	1.27	396.7±14.9	1.34	296.3±5.8[c]	100 [550–1,300]	21.4
burr	R14DS68	594438	2683558	GM-IH	362.8±12.2[a]	0.86	255.5±91.3	0.69	308.4±18.5[b]	60.5 [875–1,225]	10.0
burr	R16MS070	598392	2681297	GM-IH	371.5±14.4[a]	1.94	350.7±85.9	2.21	300.4±18.1[b]	78.4 [700–1,150]	10.9
				Weighted mean age (±1σ)	366.4±9.3						
busb	R14TS66	591094	2662303	GM-IH	308.5±7[a]	1.18	308.1±45.8	1.38	298.6±10.2[b]	75.5 [600–1,175]	9.3

Table 1. Summary of $^{40}Ar/^{39}Ar$ eruption ages for northern Harrat Rahat.—Continued

Unit symbol	Sample	Location		Material-method	Plateau or weighted mean		Isochron			^{39}Ar, in % [T range, in °C]	$^{40}Ar^*$, in %
		Easting	Northing		Age ±1σ (ka)	MSWD	Age ±1σ (ka)	MSWD	$^{40}Ar/^{36}Ar_i$ (±2σ)		
busb	R17AC130	577970	2659158	GM-IH	267±16.7[a]	1.48	250±47.5	1.61	299.3±4.6[b]	98.5 [550–1,225]	4.2
				Weighted mean age (±1σ)	302.3±14.8						
han1	R14AC101	569852	2699714	GM-IH	139±5.4[a]	1.48	143.3±19.5	1.72	294.2±11.7[c]	78.1 [550–1,000]	10.9
hhil	R16MS060	605408	2662006	GM-IH	490.1±4.6[a]	3.65	491.6±5.2	3.62	296.9±3.6[b]	95.7 [550–1,175]	45.3
hkh	R14TRO107	591285	2646655	GM-IH	29±3.9[a]	0.43	31.8±8.1	0.47	297.9±3.5[b]	85.1 [600–1,125]	2.2
hlh	R15MS017	591577	2688452	GM-IH	154.8±5.5[a]	0.96	135±15.2	0.79	297.6±3.6[c]	72.1 [550–1,150]	5.5
hma	R14TS18	583252	2697945	GM-IH	220.5±10.9[a]	1.77	258.5±71.5	1.96	292.7±11.9[c]	54.6 [550–1,125]	5.4
hmo	R14TRO29	585148	2678873	GM-IH	239±4.1[a]	0.52	237±5.6	0.57	296.0±2.4[c]	81.2 [550–1,200]	19.6
hmk	R14AC72	595357	2663246	GM-IH	265.9±7.4[a]	1.47	277.6±26.8	1.63	294.0±7.3[c]	87.5 [700–1,250]	10.2
hmk	R14AC72	595357	2663246	GM-IH	255.1±9.3[a]	1.79	168.8±61.1	1.51	308.1±19.6[c]	56 [700–1,150]	11.5
hmk	R14TS112	599688	2658186	GM-IH	238.9±4.8[a]	0.88	229.4±16.1	0.97	297.6±8.0[c]	69.5 [550–1,125]	15.5
				Weighted mean age (±1σ)	248.2±8.3						
masu	R16MS087	594178	2658890	GM-IH	252.2±2.7[a]	0.68	253.1±8.5	0.85	297.9±11.1[b]	50.7 [550–900]	32.8
md1	R14AC19	592238	2679266	GM-IH	115.7±3.5[a]	0.70	135.6±21.8	0.78	292.4±7.5[c]	65.8 [650–1,100]	5.8
md1	R14AC21	591693	2679691	GM-IH	118.4±4.5[a]	1.41	106.2±6.9	0.92	296.7±2.6[c]	87.6 [625–1,200]	4.5
				Weighted mean age (±1σ)	116.7±2.8						
mma	R14TS131	580449	2675225	GM-IH	154±8.3[a]	1.96	173.4±23.7	1.99	293.8±4.3[c]	61.1 [550–1,125]	4.4
mmk	R14TRO97	608731	2660413	GM-IH	114.4±8.5[a]	1.78	130.8±30.4	1.92	297.3±4.8[b]	93.1 [650–1,200]	2.4
mmu	R14AC96	588989	2672786	GM-IH	220.6±5.1[a]	0.82	258.7±29.3	0.69	287.8±13[c]	54.9 [675–1,150]	12.5
mmu	R14TS74	584781	2672259	GM-IH	226.8±3.4[a]	1.72	207.2±15.5	1.63	299.5±7.1[c]	100 [550–1,375]	14.6
mmu	R14TS81	595374	2673921	GM-IH	246.2±5.2	2.19	200.4±28.1[a]	1.71	304.7±12.9[c]	85 [825–1,275]	14.6
mmu	R14TS82	595378	2673907	GM-IH	211.9±3.5[a]	1.32	203.8±5.6	1.09	297.1±1.9[c]	77.5 [550–1,125]	12.4
				Weighted mean age (±1σ)	219.6±4						
mnzy	R14TS61	599920	2660121	GM-IH	461.2±6.2[a]	1.93	441.5±17.3	1.73	299.0±7.0[c]	64.4 [900–1,200]	22.5
msr	R14AC48	591711	2670200	GM-IH	389.9±5[a]	2.00	349.5±24.2	1.72	307.2±15.3[c]	70.6 [600–1,150]	28.3
mss	R14TS63	589326	2666857	GM-IH	688.6±5.9	1.72	621.8±24[a]	0.88	306.9±6.8[b]	97.9 [625–1,275]	22.5

Table 1. Summary of $^{40}Ar/^{39}Ar$ eruption ages for northern Harrat Rahat.—Continued

Unit symbol	Sample	Location		Material-method	Plateau or weighted mean		Isochron			^{39}Ar, in % [T range, in °C]	$^{40}Ar^*$, in %
		Easting	Northing		Age ±1σ (ka)	MSWD	Age ±1σ (ka)	MSWD	$^{40}Ar/^{36}Ar_i$ (±2σ)		
muq	R16MS082	595405	2670991	GM-IH	402.6±3.4	0.75	385.6±12.6[a]	0.62	304.2±8.8[b]	77.5 [625–1,150]	31.7
mz2	R14AC27	597282	2666653	GM-IH	183.7±2.8[c]	2.07	188.8±3.7	1.57	293.4±2.4[c]	89.2 [550–1,100]	18.2
mz2	R14AC64	605448	2670591	GM-IH	195.1±1.8[a]	1.32	197.2±3.3	1.38	294.2±3.4[c]	98.8 [550–1,250]	27.5
mz2	R14TS62	589387	2666827	GM-IH	197.8±2.2[a]	1.22	196.1±4.5	1.31	296.2±3.7[c]	91 [550–1,200]	23.7
mz2	R16DD270	594648	2665445	GM-IH	201.8±2.2	1.18	191.1±4.6[a]	0.61	303±3.8[b]	89.4 [550–1,200]	21.2
mz2	R16MS083	593889	2668229	GM-IH	207.3±3	1.55	198.6±5.8[a]	1.32	300.8±3[b]	93.73 [550–1,225]	15.9
		Weighted mean age (±1σ)			195.9±1.3						
mzy	R14TS46	604005	2663367	GM-IH	410.5±4.1[a]	1.16	418.2±30.9	1.53	294±13.3[c]	42.8 [750–1,050]	21.0
mzy	R14TS59	599676	2659779	GM-IH	410±5.9[a]	0.59	384.8±28.2	0.56	301.9±16.1[c]	55.4 [550–1,075]	27.5
		Weighted mean age (±1σ)			410.3±3.4						
oba	R14TS83	583976	2676263	GM-IH	242.8±2.4[a]	1.73	255.5±6.8	1.37	291.7±4.2[c]	92.6 [600–1,250]	19.5
osb	R15TS206	594307	2677881	GM-IH	620.3±8	7.67	535.8±11.8[a]	1.09	317.9±5.7[b]	76.75 [550–1,175]	32.8
og2	R14AC90	590214	2677944	GM-IH	128.2±4.2[a]	0.55	96±27.3	0.38	303±13.9[c]	36.6 [650–1,100]	9.1
og3	R14AC3	588825	2675913	GM-IH	558.7±4.8[a]	1.67	565.4±66.8	1.98	293.3±45.7[c]	45.5 [600–950]	37.4
og4	R14AC79	594576	2667074	GM-IH	319.1±2.8[a]	2.15	318.4±6.6	2.37	295.6±3.4[c]	87.5 [650–1,175]	22.4
og4	R14AC81	594714	2666700	GM-IH	1,137.9±3.1[a]	1.76	1139.6±5.1	1.90	295±2.7[c]	100 [550–1,350]	50.5
og4	R14AC82	594965	2667022	GM-IH	313±3.1[a]	1.55	301.3±7.3	1.31	297.5±2.5[c]	83.7 [550–1,150]	16.7
		Weighted mean age (±1σ)			316.4±2.1						
oju	R14TS69	590688	2676356	An-LF	441.2±6.9[a]	2.06	441.7±10.9	2.10	293.5±7.5[c]	-	-
oju	R14TS70	590357	2676968	An-IH	435.3±5.6[a]	2.06	432.5±18.3	2.61	297.0±38.8[c]	54.7 [725–1,000]	-
oju	R14AC13	590399	2675875	GM-IH	424.2±1.8[d]	1.45	422.6±5.6	1.59	296.2±6.2[c]	100 [550–1,300]	41.4
		Weighted mean age (±1σ)			437.6±4.3						
oz4	R16DD171	601032	2662221	GM-IH	433.4±2.9[a]	1.97	427.9±7.9	2.05	300.6±6.3[b]	89.51 [550–1,250]	35.6
oz4	R16MS062	602664	2662074	GM-IH	467.1±14.5	17.11	415.5±6.2[a]	1.47	304.1±1.1[b]	100 [550–1,350]	14.4
		Weighted mean age (±1σ)			430.2±6.9						
ozy	R14TS47	598779	2660691	GM-IH	418.8±1.9[a]	0.53	401.8±8.6	0.06	302±7.3[c]	81.5 [550–1,175]	36.4

Table 1. Summary of $^{40}Ar/^{39}Ar$ eruption ages for northern Harrat Rahat.—Continued

Unit symbol	Sample	Location		Material-method	Plateau or weighted mean		Isochron			^{39}Ar, in % [T range, in °C]	$^{40}Ar^*$, in %
		Easting	Northing		Age ±1σ (ka)	MSWD	Age ±1σ (ka)	MSWD	$^{40}Ar/^{36}Ar_i$ (±2σ)		
Qbra	R17TS219	576319	2717545	GM-IH	2,153±11	0.38	2,140±26[a]	0.40	300.2±6.8[b]	75 [700–1,175]	48.1
Qv	R14TS127	594070	2660650	GM-IH	986.2±10.7[a]	0.98	987.2±17.6	1.17	298.3±5.4[b]	83.4 [550–1,225]	36.8
Tbja	R17AC155	558224	2695735	GM-IH	13,562±30.2[c]	0.20	13,576±52	0.23	296±16.4[b]	38.7 [700–900]	88.9
td1	R14AC17	592217	2679181	GM-IH	16.9±2.9[a]	1.95	26.4±5.5	1.24	292.6±3.3[c]	45.8 [825–1,150]	1.8
td1	R14AC17	592217	2679181	An-IH	18.1±2.4[a]	0.45	23.7±4.5	0.12	288.5±10.8[c]	56.2 [625–1,050]	8.3
				Weighted mean age (±1σ)	17.6±1.8						
tef	R14AC29	597141	2666662	GM-IH	72.3±2.8[d]	2.05	68±6.2	2.16	296.7±3.8[c]	78.2 [550–950]	7.1
tef	R14AC55	594976	2662545	San-IH	83.7±1.6[a]	1.54	80.4±6	1.61	300.1±19.4[c]	78 [625–1,100]	29.9
tef	R14AC55	594976	2662545	San-LF	90.9±1.9[a]	1.22	88.6±6.5	1.29	296.7±29.9[c]	-	-
tef	R14AC70	595306	2662928	GM-IH	86.9±1.9[a]	0.50	89.5±4.7	0.52	294.7±2.8[c]	92.2 [550–1,150]	8.3
tef	R14AC70	595306	2662928	San-LF	86.5±8.7[a]	0.48	81±14.2	0.59	297±11.5[c]	-	-
tef	R14AC70	595306	2662928	San-IH	93.1±2.1[a]	1.19	94.7±3.4	1.21	293.2±7.2[c]	77.8 [650–1,150]	31.0
				Weighted mean age (±1σ)	88±1.8						
tg2	R14AC10	589155	2676995	San-IH	94.9±4.2[a]	2.07	95.9±5.4	2.15	293.2±8.3[c]	70.2 [600–1,075]	27.1
tg2	R14AC10	589155	2676995	San-IH	86.7±1.4	0.73	92.9±4.1 a	0.37	285.2±13.9[c]	73.3 [625–925]	31.7
tg2	R14AC86	589321	2677183	San-IH	93.8±3.1[a]	1.63	98.3±7.2	1.63	289.7±17.4[c]	71.8 [650–1,025]	28.6
				Weighted mean age (±1σ)	93.8±2.1						
tg3	R15MS010	588560	2675414	San-IH	142.4±2.2[a]	0.75	143.6±9.9	0.91	294.7±14.2[c]	69.7 [625–950]	23.5
tg4	R14AC35	593636	2665094	GM-IH	64±3.1[d]	1.43	61.8±8.1	1.41	297.4±20.1[c]	72.7 [650–1,100]	21.4
tg4	R14AC78	594832	2664097	GM-IH	85.7±4.1[a]	1.66	80.4±6.4	1.43	301.2±15.7[c]	58 [650–1,050]	31.4
tg4	R14AC80	594661	2667022	San-IH	84±1.8[a]	1.11	80.1±5.2	1.11	298.3±8.4[c]	71.4 [600–1,150]	17.6
				Weighted mean age (±1σ)	84.3±1.6						
tg5	R14AC25	596742	2666166	San-IH	79.2±1.8[a]	1.08	88.8±6.1	0.90	287.1±10.9[c]	74.1 [625–1,075]	19.0
tg5	R14AC25	596742	2666166	San-LF	112.4±2.2	1.04	86.3±13.2[a]	0.80	310.8±16.6[c]	-	-
tg5	R14AC28	597270	2666652	San-IH	81.5±3.7[a]	2.37	110.2±17.4	1.59	272.1±34.0[c]	63.3 [700–925]	18.2
				Weighted mean age (±1σ)	79.7±1.6						

Table 1. Summary of $^{40}Ar/^{39}Ar$ eruption ages for northern Harrat Rahat.—Continued

Unit symbol	Sample	Location		Material-method	Plateau or weighted mean		Isochron			^{39}Ar, in % [T range, in °C]	$^{40}Ar^*$, in %
		Easting	Northing		Age ±1σ (ka)	MSWD	Age ±1σ (ka)	MSWD	$^{40}Ar/^{36}Ar_i$ (±2σ)		
tma	R14TS68	585375	2679376	San-IH	122.3±1.9[a]	1.41	118.5±5.3	1.41	300.0±13.2[c]	69.4 [625–1,050]	33.9
tma	R14TS68	585375	2679376	GM-IH	120.6±2.1[a]	1.81	123.1±6	2.04	294.4±5.1[c]	72.8 [550–925]	14.0
				Weighted mean age (±1σ)	121.5±1.4						
tmo	R14TS28	586169	2678421	GM-IH	31.9±2.1[a]	1.85	35.8±4.6	1.88	294.4±2.4[c]	91.4 [550–1,175]	2.9
trg	R14TRO38	597700	2664563	GM-IH	15.2±2.7	1.94	4.2±5.2[a]	1.36	300.9±2.2[b]	91.025 [550–1,200]	1.1
twa	R14AC51	590154	2655719	GM-IH	41±2[a]	1.7	34.5±5.6	1.63	297.4±3.4[c]	92.2 [550–1,300]	4
twa	R14AC51	590154	2655719	San-IH	35.9±2.7[a]	1.46	30.7±5	1.93	300.3±14.4[c]	63.2 [625–900]	45.8
				Weighted mean age (±1σ)	39.2±1.6						
tz1	R14TRO50	592921	2665149	GM-IH	286.6±4.4	1.34	270.4±7.7[a]	0.07	309.1±10.6[b]	84.5 [700–1,000]	38.4
tz1	R16DD274	593191	2665405	GM-IH	288.1±3.5	2.2	268.1±6.6[a]	0.45	307±5.7[b]	63.46 [650–950]	26
				Weighted mean age (±1σ)	269.1±5						
tz2	R14AC32	595670	2663658	GM-IH	124.5±2.4[a]	1.45	120.4±7.8	1.54	296.2±2.8[c]	89.8 [600–1,150]	7
tz2	R14AC32	595670	2663658	San-IH	116.9±2.9[a]	1.6	114.2±7	1.81	298.1±16.3[c]	79.2 [625–1,075]	30.3
tz2	R14AC75	594468	2664534	GM-IH	126.8±3.8	2.82	128.8±12.6[a]	2.93	297.8±7[b]	100 [550–1,400]	10.9
				Weighted mean age (±1σ)	121.6±1.8						

[a]Preferred age for a given experiment.

[b]The age was calculated assuming $^{40}Ar/^{36}Ar_{atmosphere}$ = 298.56±0.31 (Lee and others, 2006).

[c]The age was calculated assuming $^{40}Ar/^{36}Ar_{atmosphere}$ = 295.5±0.5 (Steiger and Jäger, 1977).

[d]Indicates the age was not included in the weighted mean age for that unit.

[e]Indicates the age is only approximate because of a complicated argon release spectra.

groundmass separates were degassed at 500 degrees Celsius (°C) and sanidine separates were degassed at 600 °C until undesirable gases (for example, water, nitrogen, and hydrocarbons as measured by a Granville-Phillips 835 Vacuum Quality Monitor) were reduced to acceptable levels for argon analysis. For laser total-fusion analyses of fluence monitors and single feldspar grains, argon was extracted in a single heating step using a New Wave CO_2 laser coupled with a MAP 216 mass spectrometer. For all experiments, extracted argon was exposed to a 4-ampere tungsten filament, 125 kelvin cold finger, and two SAES ST-175 getters (one operated at 300 °C, and one at room temperature) to remove active gasses.

Uncertainties in reported $^{40}Ar/^{39}Ar$ ages include propagated uncertainties in counting statistics and J values. All age uncertainties reported in the text, figures, and tables are ±1σ uncertainty. Instrumental mass discrimination was calculated by repeated measurement of atmospheric argon. Argon isotope measurements presented in this study were made between December 2014 and July 2017. Initially, ages and mass discrimination were calculated assuming $^{40}Ar/^{36}Ar_{atmosphere}$ = 295.5±0.5 (Steiger and Jager, 1977), but starting in May 2016 the USGS argon geochronology laboratory in Menlo Park, California, began calculating ages and mass discrimination assuming $^{40}Ar/^{36}Ar_{atmosphere}$ = 298.56±0.31 (Lee and others,

2006). The assumed isotope ratio of atmospheric argon used when calculating each age is noted in table 1. The change in the assumed $^{40}Ar/^{36}Ar$ of atmospheric argon does not result in a bias in ages because both monitors and unknowns from each irradiation were calculated in the same manner. See Calvert and Lanphere (2006) and Fleck and others (2014) for additional details regarding analytical techniques, mass spectrometer design, and irradiation procedures.

^{36}Cl Cosmogenic Surface-Exposure Dating

Eleven samples were collected for ^{36}Cl cosmogenic surface-exposure dating from within our study area. Results for five of these samples have been reported by Stelten and others (2018, 2023) and Downs and others (2018, 2023a). Surface-exposure dating was used for mafic lava flows that were either too young to date via the $^{40}Ar/^{39}Ar$ method or in cases where no samples suitable for $^{40}Ar/^{39}Ar$ dating could be collected. For all samples, crushed whole-rock was used for ^{36}Cl dating, but plagioclase separates were also analyzed where available. See appendix 1 for a description of sample locations, shielding, and erosion rate estimates for all samples.

Chemical separation and analysis of samples took place at the Purdue Rare Isotope Measurement (PRIME) Laboratory at Purdue University in West Lafayette, Indiana, United States. Samples were dissolved, spiked with a ^{35}Cl enriched tracer (Desilets and others, 2006), and analyzed via accelerator mass spectrometry. All samples were split prior to dissolution and analyzed for their major-element concentrations via XRF and for their trace-element concentrations via inductively coupled plasma-atomic emission spectrometry (ICP-AES) and ICP-MS at the USGS in Denver, Colo., following the methods of Taggart (2002). Cosmogenic surface-exposure ages were calculated using the CRONUScalc ^{36}Cl Exposure Age Calculator v. 2.0 (see the Cosmic-Ray Produced Nuclide Systematics on Earth Project: http://www.physics.purdue.edu/primelab/CronusProject/cronus/ for more information). Ages were calculated using the Lal and Stone time-independent scaling model (Lal, 1991; Stone, 2000). See Marrero and others (2016) for a discussion of the CRONUScalc ^{36}Cl Exposure Age Calculator.

Results

Major-Oxide and Trace-Element Compositions of Harrat Rahat Volcanic Rocks

Eruptive products of northern Harrat Rahat range from basalt to trachyte (using the classification scheme of Cox and others [1979] to be consistent with the map of Downs and others [2019] and Robinson and Downs [2023]), with SiO_2 concentrations ranging from 45 to 64 weight percent (fig. 4*A*), consistent with previously published compositions of Harrat Rahat volcanic rocks (Camp and Roobol, 1989; Moufti and others, 2012; Murcia and others, 2017). Of the 239 eruptive units in northern Harrat Rahat distinguished by Downs and others (2019) and Robinson and Downs (2023), 180 are basalt, 13 are hawaiite, 19 are mugearite, 13 are benmoreite, and 14 are trachyte. In general, basalts of Harrat Rahat have compositions typical of intraplate, continental alkali basalts and differ from older basalts peripheral to the volcanic field, including Miocene basalts capping hills of Proterozoic basement west of Al Madīnah and early Pleistocene basalts from Harrat Kuramā‘ or Khaybar (figs. 3, 4*B*, 4*C*).

$^{40}Ar/^{39}Ar$ and ^{36}Cl Geochronology

We present 93 $^{40}Ar/^{39}Ar$ eruption ages (table 1; Stelten and others, 2020; Stelten, 2021) and 6 ^{36}Cl surface-exposure ages (tables 2 and 3, appendix 2) for volcanic products in northern Harrat Rahat, and we integrate these results with 57 $^{40}Ar/^{39}Ar$ eruption ages and 5 ^{36}Cl surface-exposure ages previously reported by Downs and others (2018, 2023a) and Stelten and others (2018, 2023). In total, eruption ages have been determined for 115 of the 239 units in the geologic map of Downs and others (2019) and Robinson and Downs (2023). Eruption ages for samples that were not directly dated were estimated on the basis of dated eruptive units that bound the undated units. In some cases, characteristic remanent magnetic directions determined from paleomagnetic analysis were used to correlate directly dated units with those lacking absolute age dates. In instances where paleomagnetic correlations can be made, we assign the eruptive age for the directly dated unit to the unit that has not been directly dated (Downs and others, 2019; Robinson and Downs, 2023). The distribution of $^{40}Ar/^{39}Ar$ and ^{36}Cl ages (along with stratigraphically and paleomagnetically constrained ages) are plotted in figure 5.

Eruption ages for volcanic deposits exposed in northern Harrat Rahat range from 1,137.9±3.1 to 0.763 ka (1256 C.E.), not including pre-Harrat Rahat mafic lavas (fig. 5). In general, the oldest volcanic products are limited to partial exposures along the margins of the study area where they extend beyond concealing younger volcanic rocks, and in the southwestern part of the study area where there was a paucity of younger volcanism (fig. 6). In contrast, younger volcanic rocks (younger than 300 ka) dominate the central part of the study area and erupted predominantly from the topographically high main vent axis, flowing either to the east, west, or north.

Downs and others (2019) and Robinson and Downs (2023) defined 12 eruptive stages based on variations in the frequency of distinguished eruptions through time (fig. 5). In general, eruptive stages were defined by distinct periods of either increased or decreased eruption frequency. However, these eruptive stages were primarily defined to allow the age of volcanic rocks to be easily viewed on the geologic map (fig. 6) and do not alone signify changes in the behavior of the magmatic system. A map displaying the topography of the northern Harrat Rahat and the locations of geologic features referred to in the discussion is provided in figure 7.

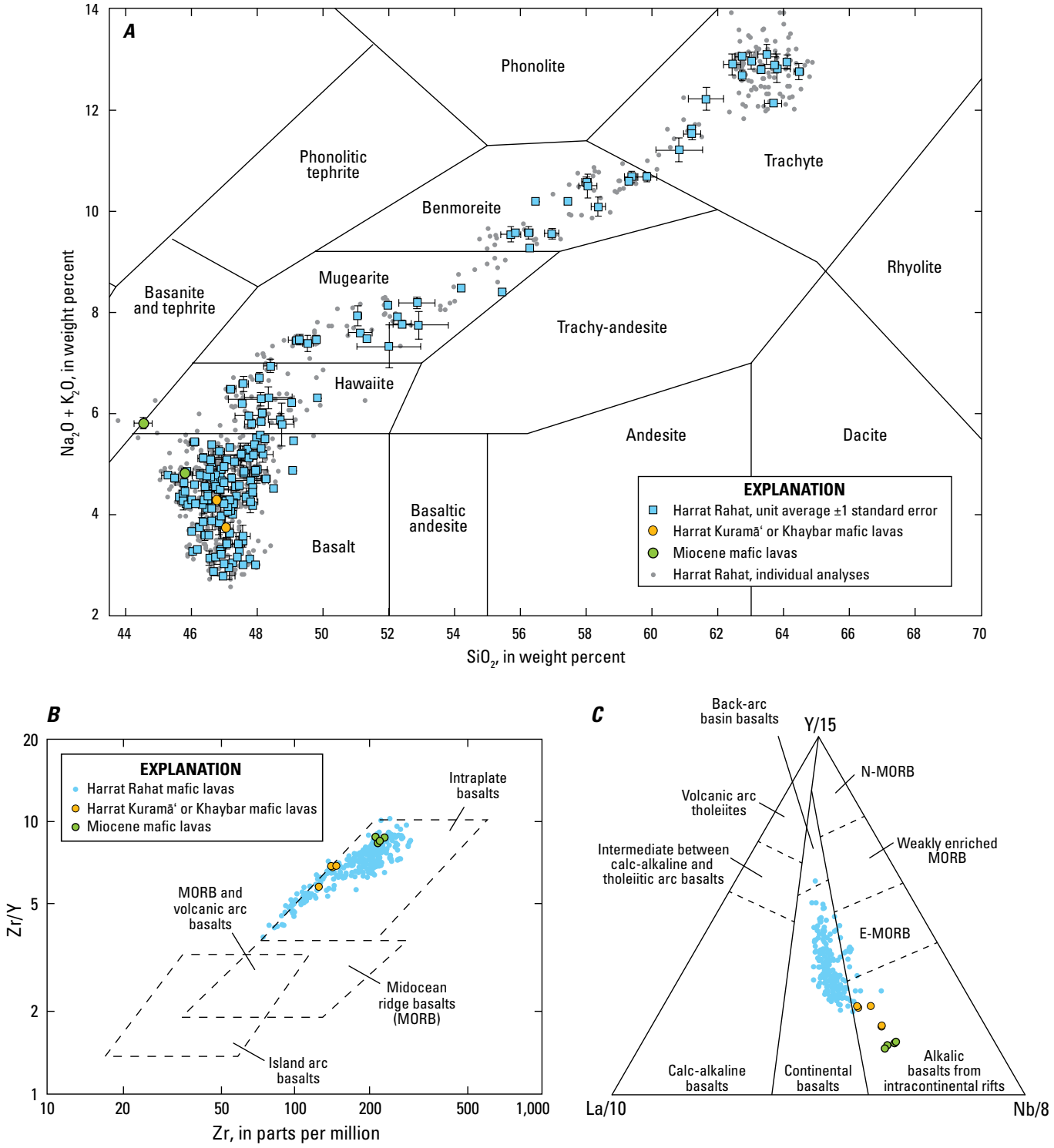

Figure 4. Whole-rock compositions for northern Harrat Rahat lavas and pyroclastic deposits and older volcanic products in the vicinity of northern Harrat Rahat. Geochemical data from Downs (2019), including analyses previously published by Dietterich and others (2018), Downs and others (2018), and Stelten and others (2018). *A,* Total alkali ($Na_2O + K_2O$) versus silica (SiO_2) diagram showing compositional fields from Cox and others (1979). Each colored data point (blue, green, or orange) represents the average of all analyses from a given eruptive unit, and the error bars represent one standard error of those analyses. Units with only one geochemical analysis have no error bar. Gray dots display all the individual geochemical analyses used to construct this diagram. *B*, Tectonic discrimination diagram of Pearce and Norry (1979). *C*, Tectonic discrimination diagram of Cabanis and Lecolle (1989). Only mafic lavas with ≥6 weight percent MgO are plotted in panels *B* and *C*. E-MORB, enriched midocean ridge basalt; N-MORB, normal midocean ridge basalt.

Table 2.. ^{36}Cl cosmogenic surface-exposure ages.

[All ^{36}Cl cosmogenic surface-exposure ages were calculated using the CRONUScalc ^{36}Cl Exposure Age Calculator v. 2.0 (Marrero and others, 2016) and the Lal and Stone time-independent scaling model (Lal, 1991; Stone, 2000). Samples easting and northing coordinates are in the World Geodetic System of 1984 (WGS 1984) Universal Transverse Mercator zone 37R north system, and elevations are in meters above sea level (mASL). Abbreviations: cm, centimeter; g, gram; g/cm^3, gram per cubic centimeter; GM, groundmass; ka, thousand years ago; PL, plagioclase; SF, topographic shielding factor; %, percent]

Sample number	Unit symbol	Phase	Easting	Northing	Elevation (mASL)	Thickness (cm)	Bulk density (g/cm^3)	SF	^{36}Cl/Cl ×10^{-15} ±1σ	^{36}Cl atoms/g ×10^5 ±1σ	^{35}Cl/^{37}Cl ±1σ	^{36}Cl age ±1σ (ka)
R14TS097[a]	bla	GM	577423	2696155	814	2	2.49	1	6.3±0.7	0.162±0.025	4.11±0.04	0.81±0.24
R17AC138	trg	GM	597588	2664566	1,261	4	2.45	1	51.4±2.0	7.23±0.96	3.31±0.02	9.0±2.5
R14AC099[a]	bdu	GM	550287	2700493	681	4	2.05	0.999921	52.4±3.7	1.43±0.11	4.26±0.02	13.3±1.9
R14TS019	bnof	GM	586138	2697339	835	4	2.33	1	88±5.6	2.76±0.18	4.07±0.01	22±3.3
R15DS107[b]	bsof	PL	596998	2690714	820	1	2.68	1	204.9±9.1	1.39±0.06	28.47±0.75	21.4±2.3
R14TS009[a]	bsof	GM	589287	2687759	920	4	2.36	1	149.9±6.8	2.43±0.13	5.47±0.11	26.4±2.9
R15MS014	bsof	GM	589900	2688412	914	5	2.33	1	153.4±7.8	2.56±0.16	5.36±0.11	26.0±3.0
R15MS030	bcef	GM	589383	2699479	820	4	1.87	1	129.5±5.5	3.03±0.17	4.45±0.06	29.1±3.7
R15MS006[a]	han3	GM	578980	2682169	949	4	1.81	0.999986	196.5±7.6	8.39±0.54	3.79±0.04	51.0±9.0
R15TS189[c,d]	bms	PL	578242	2677857	924	1	2.68	1	525.2±20.9	3.55±0.14	31.45±0.71	56.5±6.7
R15MS004[c]	bms	GM	580779	2680668	1,023	4	1.95	1	287.3±9.7	8.94±0.46	4.10±0.05	66±11

[a]Data from Downs and others (2018).

[b]The age for sample R15DS107 was calculated using the bulk rock composition from sample R14TS9a.

[c]Data from Stelten and others (2018).

[d]The age for sample R15TS189 was calculated using the bulk rock composition from sample R15MS004.

Table 3. Composition of samples used for ^{36}Cl cosmogenic surface-exposure dating.

[Bulk-rock Cl concentrations were measured by isotope dilution at Purdue Rare Isotope Measurement (PRIME) Laboratory at Purdue University. Major-oxide abundances (in weight percent [wt. %]) were measured by X-ray fluorescence and trace-element abundances (in parts per million [ppm]) were measured by inductively coupled plasma atomic emission spectrometry and inductively coupled plasma mass spectrometry following Taggart (2002). Abbreviations: GM, groundmass; PL, plagioclase]

Sample number	Unit symbol	Phase	Major elements (wt. %)											Trace elements (ppm)				
			SiO_2	TiO_2	Al_2O_3	Fe_2O_3	MnO	MgO	CaO	Na_2O	K_2O	P_2O_5	LOI	Cl	Sm	Gd	U	Th
R14TS097[a]	bla	GM	46.9	3.07	16.9	13.8	0.21	5.75	8.29	4.03	0.97	0.89	0.44	145.5	7	7.24	0.49	1.5
R17AC138	trg	GM	62.9	0.2	17.3	5.8	0.2	0.2	1.3	7.0	5.0	0.1	1.47	792.1	11.7	11.3	2.5	7.6
R14AC099[a]	bdu	GM	46.0	3.06	17.1	13.5	0.18	6.56	10.3	3.10	0.58	0.22	0.38	124.2	4.10	4.50	0.27	0.8
R14TS019	bnof	GM	45.5	3.79	16.7	14.4	0.18	6.58	8.79	3.62	0.8	0.35	0.42	147.6	4.8	4.92	0.41	1.3
R15DS107[b]	bsof	PL	52.5	0.09	30.3	0.44	<0.01	0.07	12.0	4.37	0.21	<0.01	0.28	1.2	0.2	0.13	<0.05	<0.1
R14TS009[a]	bsof	GM	45.6	2.39	16.2	13.2	0.18	8.88	10.6	2.80	0.39	0.20	0.42	57.1	3.2	3.69	0.17	0.4
R15MS014	bsof	GM	46.2	2.94	17.2	12.9	0.17	6.23	10.8	3.06	0.56	0.22	0.33	60.0	4.2	4.57	0.28	0.8
R15MS030	bcef	GM	47.0	3.75	17.4	12.6	0.14	4.68	9.5	3.36	0.73	0.29	0.60	101.0	5.0	5.30	0.48	1.2
R15MS006[a]	han3	GM	49.4	2.35	17.0	13.3	0.24	4.30	6.83	4.79	1.53	0.73	0.39	212.9	7.2	6.96	0.64	1.7
R15TS189[c,d]	bms	PL	53.0	0.10	29.6	0.43	<0.01	0.08	11.5	4.69	0.24	0.02	0.39	0.6	0.3	0.23	0.05	0.3
R15MS004[c]	bms	GM	46.5	3.56	17.9	13.9	0.20	4.83	8.17	3.96	0.84	0.49	0.29	144.1	3.6	3.80	0.33	1.0

[a]Data from Downs and others (2018).

[b]The age for sample R15DS107 was calculated using the bulk rock composition from sample R14TS9a.

[c]Data from Stelten and others (2018).

[d]The age for sample R15TS189 was calculated using the bulk rock composition from sample R15MS004.

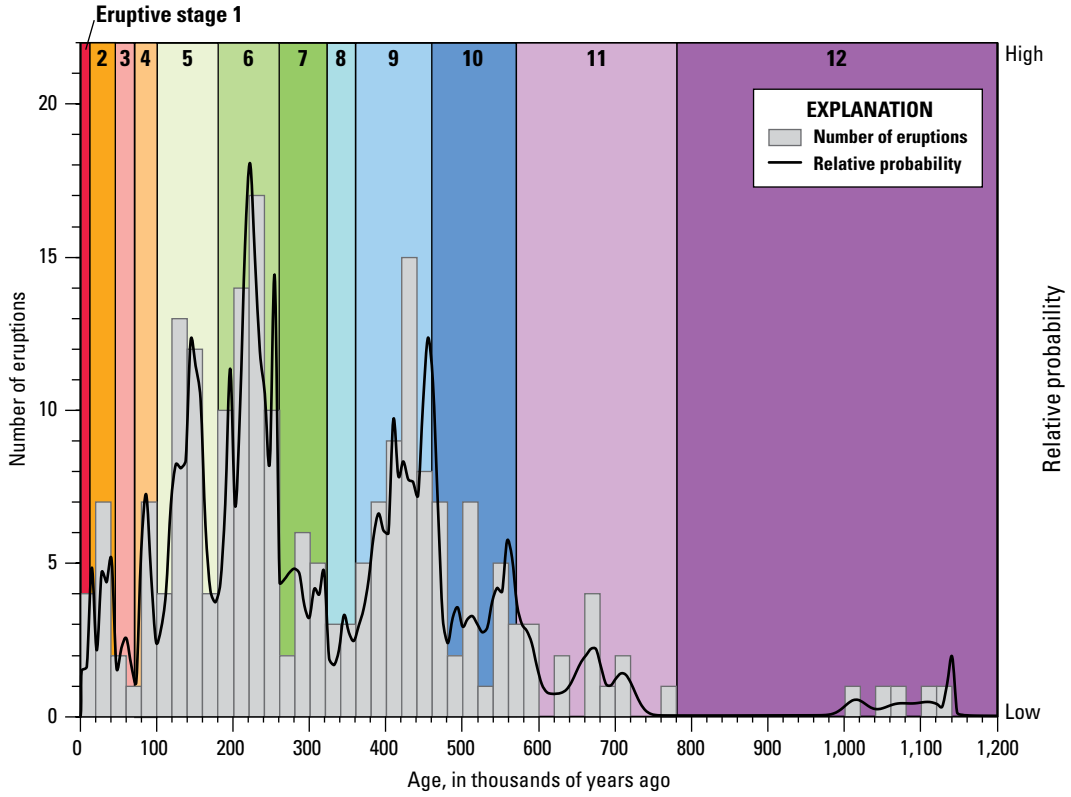

Figure 5. Probability density function (black solid line) and histogram (gray bars) showing the distribution of measured eruption ages for volcanic products from northern Harrat Rahat. This figure was constructed using the default setting in Isoplot (Ludwig, 2003) with bin sizes of 20 thousand years for the histogram. The probability density function displays the probability distribution obtained by summing the individual probability distributions (with normally distributed errors) represented by the suite of age data for northern Harrat Rahat. Volumes are not accounted for in this diagram, only the number of eruptions. Absolute ^{36}Cl and $^{40}Ar/^{39}Ar$ eruption ages as well as ages constrained by stratigraphy or paleomagnetic correlation are included in the diagram. Broad peaks in the probability density function represent periods of more frequent volcanism, whereas valleys represent periods of less frequent eruptions. Note that narrow, tall peaks are the result of very precise eruption ages, and do not alone signify periods of increased volcanism. Vertical bands of color represent eruptive stages in northern Harrat Rahat and correspond to colors on figure 6 (eruptive stage numbers provided along the top x-axis). Proportionally fewer eruptions are distinguished in older stages because of erosion and concealment beneath younger deposits.

Discussion

The Eruptive History of Northern Harrat Rahat

Geochronological and geochemical data combined with recent field mapping from the SGS-USGS project have led to a significant reinterpretation of the eruptive history of northern Harrat Rahat relative to prior studies (Camp and Roobol, 1989; Moufti and others, 2013) and greatly expanded upon datasets for northern Harrat Rahat reported by Downs and others (2018) and Stelten and others (2018) (fig. 6). Major revisions to the eruptive history of northern Harrat Rahat as a result of this new work include the following:

1. Geologic observations and mapping presented by Downs and others (2019) and Robinson and Downs (2023) allow for improved subdivision, reconstruction, and understanding of the Quaternary eruptive history.
2. $^{40}Ar/^{39}Ar$ data are interpreted to indicate that the oldest volcanic units exposed at the surface of northern Harrat Rahat erupted after 1,200 ka.
3. $^{40}Ar/^{39}Ar$ and ^{36}Cl data are interpreted to indicate that 90 percent (214 of 239) of the exposed and mapped volcanic units erupted after 570 ka. This contrasts with previous work that suggests most exposed volcanic units erupted between 1,700 and 600 ka.

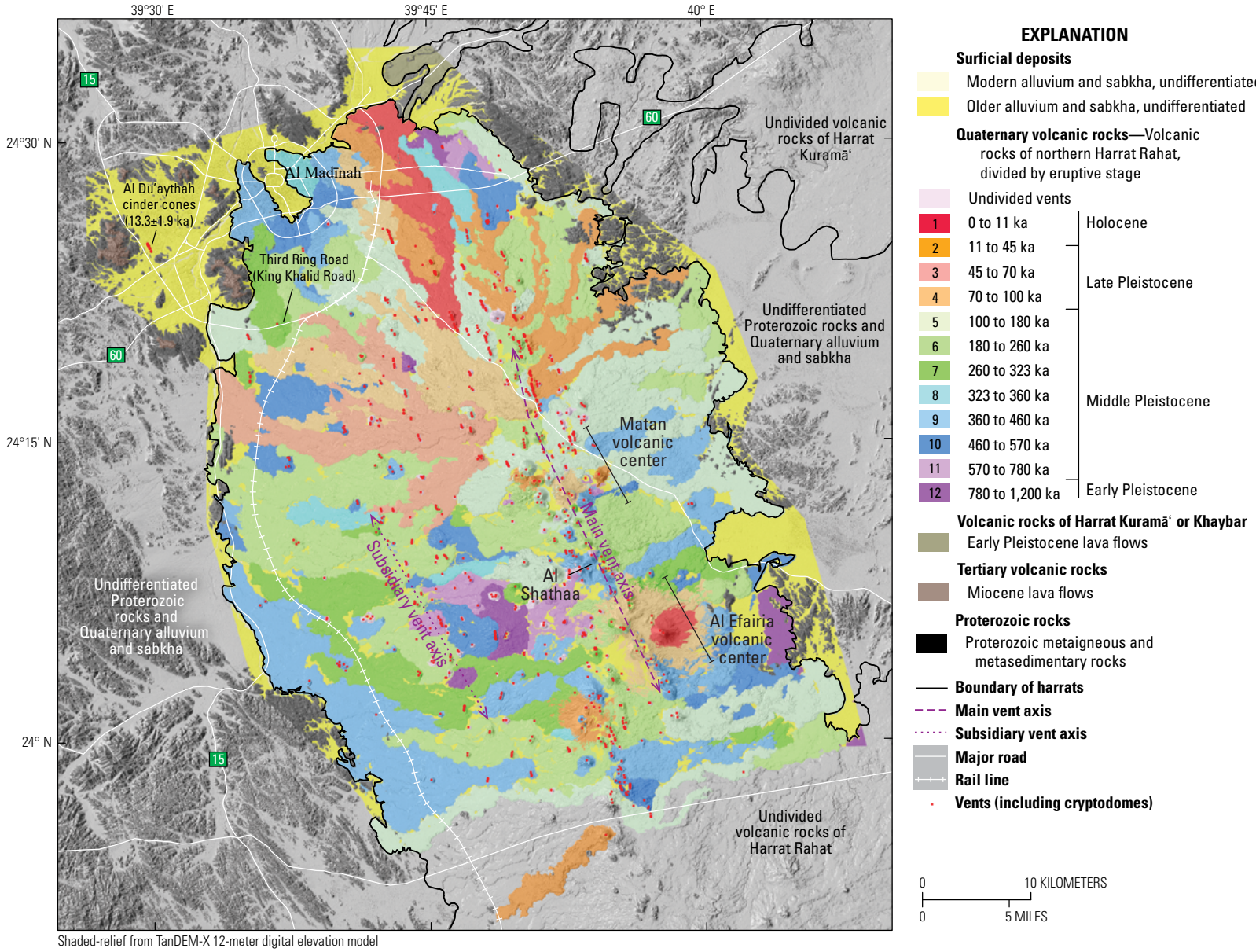

Figure 6. Geologic map of the study area in northern Harrat Rahat, displaying the age of eruptive products. Red dots represent the location of each eruptive crater, scoria cone, dome, non-erupted cryptodomes, and include nested and aligned craters and scoria cones from single eruptions. The purple dashed line and the purple dotted line indicate the location and trends of the main vent axis and the subsidiary vent axis, respectively, which are defined by constructional relief and alignments and concentrations of volcanic vents. The location of the Matan volcanic center, Al Efairia volcanic center, and the explosive eruption of the benmoreite of Al Shathaa (unit osa) along the main vent axis are indicated. Geology from Downs and others (2019) and Robinson and Downs (2023). ka, thousand years ago.

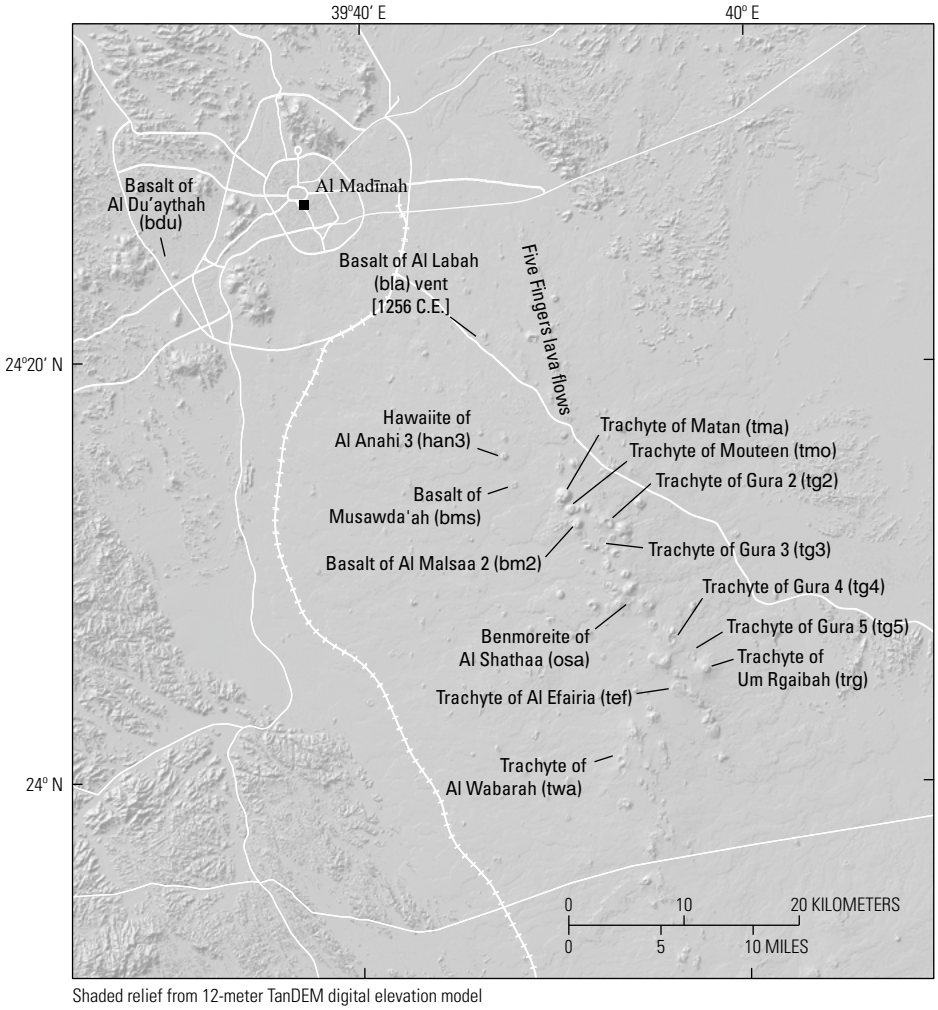

Figure 7. Shaded-relief map of the study area in northern Harrat Rahat showing the location of volcanic features referred to in the text. Names of volcanic features are from Downs and others (2019) after Moufti (1985).

4. Only two Holocene eruptions occurred within northern Harrat Rahat. These include the well-documented historical eruption of the basalt of Al Labah (unit bla) at 1256 C.E. and the eruption of the trachyte of Um Rgaibah (unit trg) at 4.2±5.2 ka ($^{40}Ar/^{39}Ar$ result) or 6.6±2.9 ka (weighted mean of $^{40}Ar/^{39}Ar$ and ^{36}Cl ages). All other units presented as Neolithic to post-Neolithic, including the proposed 641 C.E. eruption (from Camp and Roobol, 1989, 1991), have been shown to be late Pleistocene (older than 11 ka) using $^{40}Ar/^{39}Ar$ and ^{36}Cl geochronology or based on stratigraphic relations with well-dated volcanic deposits (this study; Downs and others, 2018).

5. With eruption ages determined for 115 of the 239 volcanic products, based on 150 $^{40}Ar/^{39}Ar$ ages and 11 ^{36}Cl surface-exposure ages, northern Harrat Rahat is now one of the best-dated mafic volcanic fields in the world.

Below we describe each of the 12 eruptive stages defined in this study and by Downs and others (2019) and Robinson and Downs (2023) (fig. 5). In general, eruptive stages were defined by distinct periods of either increased or decreased eruption frequency, based on the distribution of eruption ages (fig. 5). A summary of the main characteristics of each eruptive stage is provided in table 4. The observations described in table 4 provides the framework for the petrogenetic model presented in the discussion.

Eruptive Stage 12 (Between 1,200 and 780 ka)

Eruptive stage 12 is defined by the oldest exposed dated rock from northern Harrat Rahat, a benmoreite erupted at 1,137.9±3.1 ka, which encompasses an apparent gap in measured ages from 1,014 to 780 ka (table 1; fig. 5). It is likely that more eruptions occurred within the study area during this time but are not exposed because they are covered by younger volcanic products, as indicated by depth-to-basement estimates for northern Harrat Rahat ranging from 100 to 600 m (Langenheim and others, 2019, 2023). Four units in northern Harrat Rahat were originally designated by Camp and Roobol (1989, 1991) as Hammah basalt (2.5–1.7 Ma), but new $^{40}Ar/^{39}Ar$ ages show that these units are all younger than 1.2 Ma ($^{40}Ar/^{39}Ar$ ages of 1,014.0±14.0 ka, 698.1±16.0 ka, and 285.1±6.6 ka) and are better considered part of the Madinah basalt.

Table 4. Summary of the 12 eruptive stages for volcanism in northern Harrat Rahat.

[Summary of characteristics of the 12 eruptive stages defined in this paper and Downs and others (2019). See figures 3 and 6 for the location of the main vent axis (MVA) and subsidiary vent axis (SVA) within the volcanic field. Abbreviations: ka, thousand years ago; k.y., thousand years]

Eruptive Stage	Age range (time span)	Number of known eruptions (by composition)[a]	Vent locations	Apparent occurrence rate[b] (eruptions/k.y.)	Additional observations
1	<11 ka (11 k.y.)	1 basalt, 1 trachyte	MVA	0.18	Basalt and hawaiite dominate in the north. Trachyte dominates in the south near the Al Efairia volcanic center
2	<45 to >11 ka (34 k.y.)	5 basalts, 1 hawaiite, 3 trachytes	MVA (except one eruption)	0.27	Basalt and hawaiite dominate in the north. Trachyte dominates in the south near the Al Efairia volcanic center
3	<70 to >45 ka (25 k.y.)	1 basalt, 1 hawaiite	MVA	0.08	Basalt and hawaiite dominate in the north. Trachyte dominates in the south near the Al Efairia volcanic center
4	<100 to >70 ka (30 k.y.)	2 basalts, 1 hawaiite, 1 mugearite, 2 trachytes	MVA	0.2	Basalt and hawaiite dominate in the north. Trachyte dominates in the south near the Al Efairia volcanic center
5	<180 to >100 ka (80 k.y.)	22 basalts, 5 hawaiites, 3 mugearites, 2 benmoreites, 3 trachytes	MVA (except one eruption)	0.44	Basalt and hawaiite dominate in the north. Trachyte dominates in the south near the Al Efairia volcanic center
6	<260 to >180 ka (80 k.y.)	42 basalts, 3 hawaiites, 5 mugearites, 3 benmoreites	MVA, SVA	0.66	Volcanism clustered around 225 ka
7	<323 to >260 ka (63 k.y.)	14 basalts, 1 benmoreite, 1 trachyte	MVA, SVA	0.25	Trachyte erupted from the Al Efairia volcanic center
8	<360 to >323 ka (37 k.y.)	5 basalts	MVA,SVA	0.14	
9	<460 to >360 (100 k.y.)	34 basalts, 1 hawaiite, 9 mugearites, 5 benmoreites, 1 trachyte	MVA, SVA	0.5	Trachyte erupted from the Al Efairia volcanic center
10	<570 to >460 ka (110 k.y.)	30 basalts, 1 hawaiite, 2 benmoreites	MVA, SVA	0.3	
11	<780 to >570 ka (210 k.y.)	13 basalts, 1 mugearite	MVA, SVA	0.07	Mostly concealed by younger eruptive products. All compositions erupt from the Matan volcanic center
12	<1,200 to >780 ka (420 k.y.)	6 basalts, 1 benmoreite	MVA, SVA	0.02	Mostly concealed by younger eruptive products. All compositions erupt from the Matan volcanic center

[a]Note that the number of eruptions corresponds to the number of distinct map units from Downs and others (2019), not the number of volcanic vents.

[b]The apparent occurrence rate for each eruptive stage is provided to allow for a comparison of the productivity of each eruptive stage.

In total, seven eruptive products have been distinguished as falling within eruptive stage 12, six of which are basalts and one is the aforementioned benmoreite. Outcrops of stage 12 basalts are of limited aerial extent but are present throughout the map area, which suggests that basalts vented widely. The stage 12 benmoreite is exposed within the crater that formed during a trachyte eruption at 84.3±1.6 ka (Gura 4 in fig. 7) within the Al Efairia volcanic center and likely erupted from the main vent axis. This benmoreite's exposure is topographically high, indicating that preferential eruptive activity along the main vent axis occurred before approximately 1 Ma and constructed much of its positive relief. The presence of a benmoreite eruption at 1,137.9±3.1 ka also establishes that evolved magmas erupted along the main vent axis over the past 1.2 m.y.

Eruptive Stage 11 (Between 780 and 570 ka)

After 780 ka, the number of exposed and distinguished eruptive products increased. Fourteen distinct eruptions are known to have occurred between 780 and 570 ka, although this is a minimum estimate because of concealment by younger eruptive products. Of these 14 eruptive units, 13 are basalts and one is mugearite. Stage 11 basalts appear as limited outcrops throughout the map area. Most stage 11 basalts erupted from either the main vent axis or from the subsidiary vent axis in the southern part of the map area. The only mugearite recognized as stage 11 erupted at 621.8±24.0 ka and is proposed to have vented from the main vent axis near the crater formed during eruption of the benmoreite of Al Shathaa (unit osa; fig. 3).

Eruptive Stage 10 (Between 570 and 460 ka)

From 570 to 460 ka, there is a significant increase in the number of exposed and distinguished eruptive units, which is likely because of better exposure (that is, lack of burial) of stage 10 eruptive products relative to previous eruptive stages. In total, 33 eruptive units are identified as stage 10. Of these, 30 are basalt, one is hawaiite, and two are benmoreites. Basaltic units are distributed throughout the map area, appearing as partially exposed lava flows. Although vent locations for many of the basaltic eruptions are not known, exposures of stage 10 basalts suggest that they erupted from both the main and subsidiary vent axes.

The only hawaiite known to have erupted in stage 10 effused at 490.1±4.6 ka from the south end of the main vent axis. Two benmoreites are known to have erupted during stage 10 at 558.7±4.8 and 535.8±11.8 ka. One benmoreite (558.7±4.8 ka) is exposed in the northern wall of the crater and formed during the 142.4±2.2 ka eruption of the trachyte of Gura 3 (unit tg3; gura or fawha is Arabic for vent or nozzle) in the Matan volcanic center (fig. 7). Therefore, this benmoreite is proposed to have erupted from the main vent axis in the Matan volcanic center. The second benmoreite (535.8±11.8 ka) is also located within the Matan volcanic center and forms an approximately 4.5-km-long flow extending to the northeast, although its vent location is concealed by younger volcanic deposits. Thus, it is apparent that evolved volcanism erupted exclusively from the main vent axis, and that this vent axis had attained much of its elevated topography, indicating it was the site of preferential eruptions integrated at that time.

Eruptive Stage 9 (Between 460 and 360 ka)

From 460 to 360 ka, the frequency of volcanism in northern Harrat Rahat increased relative to stage 10, with 51 eruptions distinguished during stage 9. Erosion subdued the margins of stage 9 basalts exposed widely in the southwest part of the study area, and the number of flows in that area may be greater than distinguished by mapping and dating. Products of the distinguished eruptions are 34 basalts, 1 hawaiite, 9 mugearites, 5 benmoreites, and 2 trachytes. Thus, although volcanism during this stage was primarily basaltic, similar to stages 10, 11, and 12, the proportion of evolved magmas increased relative to previous eruptive stages.

Basaltic eruptive products are present throughout the map area. Most basalts during stage 9 produced broad lava flows exposed in the southern part of the field area, especially at its southwest and south periphery. This suggests that many of the stage 9 basalts erupted from the subsidiary vent axis. Several basalts (and the only hawaiite erupted during stage 9) also appear to have vented from within or east of the main vent axis and flowed toward the east margin of the field.

All mugearite, benmoreite, and trachyte magmas that erupted during stage 9 vented from the main vent axis. Mugearites erupted during this stage are exposed along the main vent axis south of the Matan volcanic center. The five benmoreites erupted during stage 9 display diverse emplacement characteristics. Three benmoreites are located at the south end of the main vent axis and formed lava flows extending at least 2.2 to 6.5 km from their vent locations. One benmoreite is located within the Matan volcanic center and erupted in two phases at 437.6±4.3 and 424.2±1.8 ka, forming lava domes, flows, and pyroclastic flow deposits. The benmoreite of Al Shathaa (unit osa) is unique among benmoreites at northern Harrat Rahat because it erupted explosively, forming block-and-ash flow and other pyroclastic-flow deposits sourced from a 0.5-km-diameter crater located along the main vent axis between the Matan and Al Efairia volcanic centers (figs. 3, 7). Eruptive stage 9 marks the first exposures of trachyte in the map area—a small, aphyric lava dome and a pyroclastic flow deposit that reach at least 2 km from its source vent, both located in the Al Efairia volcanic center.

Eruptive Stage 8 (Between 360 and 323 ka)

Eruptive stage 8 represents a lull in volcanism in northern Harrat Rahat (fig. 5). During stage 8, only five eruptions are documented, all of which produced basalt. Stage 8 eruptive units are exposed throughout the study area and seem to have

erupted dominantly from the subsidiary vent axis, except for only one basalt known to have erupted from the main vent axis. It is possible that more eruptions occurred during this time and are covered by younger eruptive products, but we consider it likely that this stage represents a true lull in volcanism possibly because of a decrease in the input of mantle-derived magmas into the crust.

Eruptive Stage 7 (Between 323 and 260 ka)

Sixteen distinct volcanic units are known to have erupted between 323 and 260 ka, of which 14 are basaltic, one is benmoreitic, and one is trachytic. Stage 7 basalts vented from both the main and subsidiary vent axes and are best exposed in the southwestern part of the map area where younger lava flows and tuffs from later eruptive stages 5 through 1 are absent.

Few evolved magmas erupted in stage 7. Exposure of the one benmoreite is limited to the walls of the crater formed during the explosive eruption of the trachyte of Gura 4 (unit tg4) at 84.3±1.6 ka within the Al Efairia volcanic center. The extent of this benmoreite is unknown because it is concealed by younger units, but its exposure suggests that it erupted from the main vent axis within the Al Efairia volcanic center. The trachyte that erupted during stage 7 forms an aphyric dome within the Al Efairia volcanic center.

Eruptive Stage 6 (Between 260 and 180 ka)

Eruptive stage 6 represents the largest pulse of volcanism known for northern Harrat Rahat. Fifty-three distinct eruptions are found to have occurred over the course of 80 k.y. Of these, 42 were of basalt, 3 were of hawaiite, 5 were of mugearite, and 3 were of benmoreite. Basaltic volcanism was distributed over both the main and subsidiary vent axes, and stage 6 basalts are present in all regions of the map area. Hawaiites that erupted during stage 6 vented along the length of the main vent axis, dominantly near the Matan and the Al Efairia volcanic centers. Mugearites erupted along the length of the main vent axis, like hawaiites, but benmoreite erupted only from the central part of the main vent axis within the Matan volcanic center.

A unique feature of eruptive stage 6, contrasting with previous eruptive stages, is that the timing of volcanism was highly clustered at around 225 ka (fig. 5). In contrast, stage 9 had a similar number of eruptions (51 over 100 k.y.), but these were distributed over a longer duration (fig. 5). Indeed, after eruptive stage 6, volcanism in northern Harrat Rahat became more tightly clustered in both time and space.

Eruptive Stage 5 (Between 180 and 100 ka)

From 180 to 100 ka, products from 35 eruptions are distinguished in northern Harrat Rahat, and exposures are sufficient that, for stages 5 and younger, eruption products distinguished by field observations and dating are close to the true numbers of eruptions. Of these eruptions, 22 were of basalt, 5 were of hawaiite, 3 were of mugearite, 2 were of benmoreite, and 3 were of trachyte. Eruptions during stage 5 were clustered in time. After a brief lull in volcanism from approximately 175 to 155 ka, the rate of volcanism increased substantially. Most volcanic products from stage 5 erupted between 155 and 125 ka, after which the rate of volcanic eruptions decreased between 125 and 100 ka (table 1; fig. 5). The basalt of Al Malsaa 2 (unit bm2, located in the Matan volcanic center) was originally assigned a Holocene age by Camp and Roobol (1989), but it is covered on its north slope by pyroclastic flow deposits from the 31.9±2.1 ka eruption of the trachyte of Mouteen (unit tmo), demonstrating that the basalt erupted before 31.9 ka. We have assigned the basalt of Al Malsaa 2 (unit bm2) to eruptive stage 5.

Stage 5 eruptive products show a distinct spatial distribution relative to previous eruptive stages. In previous eruptive stages, basalt erupted from the entire north-south length of both the main and subsidiary vent axes, and more evolved magmas erupted exclusively from the main vent axis. However, beginning in eruptive stage 5, nearly all magmas, regardless of compositions, erupted along the main vent axis. One stage 5 basalt did not erupt along the main vent axis and instead erupted from the northwest margin of the volcanic field. Furthermore, starting with stage 5, a pattern emerged in which the composition of volcanic products varied systematically along the length of the main vent axis. The part of the study area north of the Matan volcanic center erupted basalt and hawaiite magmas exclusively. Within the Matan volcanic center, eruption of basalt, hawaiite, mugearite, benmoreite, and trachyte occurred. Within the Al Efairia volcanic center, only trachyte erupted. A single hawaiite erupted near Al Shathaa during stage 5 (fig. 3), but otherwise the region along the main vent axis between the Matan volcanic center and Al Efairia volcanic center was devoid of eruptions.

Eruptive Stage 4 (Between 100 and 70 ka)

Eight eruptions have been documented during stage 4 over a brief interval from approximately 94 to 80 ka. Of these eight eruptions, two were of basalt, one was of hawaiite, one was of mugearite, and four were of trachyte. Thus, this eruptive stage was characterized by frequent eruption of trachyte. Like stage 5, no eruptions vented from the subsidiary vent axis. The basalt, hawaiite, and mugearite magmas of stage 4 erupted exclusively in the northern part of the study area along the main vent axis, and they flowed to the north or northeast toward the city of Al Madīnah. Trachyte erupted from the southern part of the main vent axis in both the Matan and the Al Efairia volcanic centers. Like stage 5, only trachyte erupted from the Al Efairia volcanic center.

Trachyte eruptive products belonging to stage 4 include the trachyte of Gura 2 (unit tg2; 93.8±2.1 ka), located within the Matan volcanic center, and the trachytes of Al Efairia (unit tef; 88±1.8 ka), Gura 4 (unit tg4; 84.3±1.6 ka), and Gura 5 (unit tg5; 79.7±1.6 ka) located within the Al Efairia volcanic center. All four of these trachyte units erupted explosively, forming pyroclastic-flow and -surge deposits (Moufti, 1985;

Downs and others, 2019; Robinson and Downs, 2023). The explosive eruption of the trachyte of Gura 2 (unit tg2) was preceded by the formation of a dome that was largely destroyed in the subsequent explosive activity. Eruption of the trachyte of Al Efairia (unit tef) was the largest explosive eruption known in northern Harrat Rahat, having pyroclastic flow deposits preserved continuously as far as 9 km from its source vent. Field relations show that the trachyte of Al Efairia (unit tef) underlies the trachytes of Gura 4 and Gura 5 (units tg4 and tg5, respectively) (Moufti, 1985; Downs and others, 2019; Robinson and Downs, 2023), consistent with the $^{40}Ar/^{39}Ar$ eruption ages. The trachytes of Gura 4 and Gura 5 have identical $^{40}Ar/^{39}Ar$ eruption ages (within analytical uncertainty), as well as identical chemical compositions and remanent magnetic directions, suggesting that they erupted at the same time from the same batch of magma (Downs and others, 2019, 2023b).

Eruptive Stage 3 (Between 70 and 45 ka)

After the eruption of the trachyte of Gura 5 (unit tg5) at 79.7±1.6 ka, no eruptions occurred in northern Harrat Rahat for approximately 19 k.y. Stage 3 consists of only two eruptions, the hawaiite of Al Anahi 3 (unit han3) and the basalt of Musawda'ah (unit bms). The hawaiite of Al Anahi 3 directly overlies the basalt of Musawda'ah and was originally interpreted to be Holocene (Camp and Roobol, 1989). However, ^{36}Cl surface-exposure dating demonstrates that the hawaiite of Al Anahi 3 erupted at 51.0±9.0 ka (Downs and others, 2018), and that the underlying basalt of Musawda'ah erupted at 59.1±5.7 ka (Stelten and others, 2018). Both lavas issued from vents on the west flank of the main vent axis near the Matan volcanic center and formed long, branching flows that advanced to the west, southwest, and northwest, away from the main vent axis. The basalt of Musawda'ah extends as far as 27 km from its source vent, reaching the west edge of the volcanic field. The hawaiite of Al Anahi 3 extends as far as 20 km from its source vent, reaching the Third Ring Road of Al Madīnah (figs. 3, 6; King Khalid Road). These eruptive units dominate the landscape in the west-central part of the study area and were the only ones to have erupted in what was otherwise a period of minimal volcanism.

Eruptive Stage 2 (Between 45 and 11 ka)

After an eruptive hiatus from approximately 51 to 40 ka, volcanism resumed with nine eruptions between 39 and 13 ka (table 1). Of these nine eruptions, five were of basalt, one was of hawaiite, and three were of trachyte. The distribution of eruptive products in stage 2 is like those of eruptive stages 5 through 3. Basalts were the sole magmas to erupt from vents around the north end of the main vent axis during stage 2. One basalt erupted at 25.6±16.2 ka from a vent just west of the historical (1256 C.E.) lava flow and flowed northward. This unit is now exposed within the Third Ring Road of Al Madīnah (figs. 3, 6). All eruptions during stage 2 occurred along the main vent axis, except for a single basalt eruption that vented west of Al Madīnah and outside of the contiguous volcanic field at 13.3±1.9 ka (Downs and others, 2018). This eruption produced four small scoria cones aligned in a northwesterly direction that fed two small lava flows that traveled only approximately 0.1 km from their source vents (figs. 3, 6). Previous researchers provisionally interpreted this eruption to be have occurred at 641 C.E. based on indirect historical accounts and minimal incision (Camp and Roobol, 1989; Murcia and others, 2015).

Three basaltic eruptions, collectively referred to as the Five Fingers lava flows (Murcia and others, 2017; Dietterich and others, 2018, 2023; Downs and others, 2019; Robinson and Downs, 2023), vented from the upper east flank of the northern end of the main vent axis. The Five Fingers eruptions were previously interpreted as post-Neolithic (that is, after 6 ka) by Camp and Roobol (1991). More recently, Murcia and others (2017) suggested minimum ages of 17.3 to 34.9 ka based on ^{3}He dating of olivine from the Five Fingers lavas. New ^{36}Cl surface-exposure dating refines these age estimates and demonstrates that the basalt of Northern Fingers (unit bnof), the basalt of Central Finger (unit bcef), and the basalt of Southern Fingers (unit bsof) erupted at 22.0±3.3 ka, 29.1±3.7 ka, and 24.0±1.5 ka, respectively. Field relations demonstrate that the basalt of Central Finger (unit bcef) underlies the other two flows, but the Northern and Southern Fingers flows (units bnof, bsof) are nowhere in contact, so their relative ages cannot be determined. Lavas from the three eruptions have distinct remanent magnetic directions that indicate the units erupted at slightly different times (Downs and others, 2019). However, given the overall similarity in chemical composition of these three units and their identical ^{36}Cl exposure ages (within analytical uncertainty), we use a weighted mean age of the three basalts (24.4±1.3 ka) as their eruption age but recognize that there may have been centuries between their eruptions.

The only hawaiite to have erupted during stage 2 vented in the southern part of the study area at 29.0±3.9 ka and flowed southwestward approximately 12 km from its vent. Paleomagnetic data are interpreted to suggest that this eruption occurred during the Mono Lake excursion (Oda, 2005; Downs and others, 2019). Two of three trachyte eruptions during stage 2 were within the Matan volcanic center on the crest of the main vent axis. Both eruptions commenced explosively, generating small-volume pyroclastic-flow deposits, and each ended with extrusion of a steep-sided dome. No trachytes erupted within the Al Efairia volcanic center during stage 2. However, the trachyte of Al Wabarah (unit twa) erupted at 39.2±1.6 ka, approximately 8 km west of the Al Efairia volcanic center, making it spatially unique among trachytes of northern Harrat Rahat (figs. 3, 6). The Al Wabarah eruption was explosive, generating pyroclastic-flow deposits that are preserved as far as 3.7 km from their source vent, which itself is a deep, open crater, showing that lava dome collapse was not the sole cause of trachytic pyroclastic flows.

Eruptive Stage 1 (Younger than 11 ka)

Camp and Roobol (1991) concluded that Harrat Rahat erupted 13 times in the Holocene Epoch (younger than 11 ka), with 9 of these eruptions in the SGS-USGS study area of northern Harrat Rahat close to the city of Al Madīnah. Our $^{40}Ar/^{39}Ar$ and ^{36}Cl ages demonstrate that there have been only two Holocene eruptions in northern Harrat Rahat. One was the well-documented historical eruption of the basalt of Al Labah (unit bla) in 1256 C.E. that vented along the northwestward end of the main vent axis and flowed northward 22 to 23 km, reaching just east of contemporary Al Madīnah (Camp and others, 1987). The other Holocene eruption was the trachyte of Um Rgaibah (unit trg), which vented within the Al Efairia volcanic center. Previously not recognized as Holocene, it yields a $^{40}Ar/^{39}Ar$ age of 4.2±5.2 ka and a ^{36}Cl age of 9.0±2.5 ka (combining these gives a weighted mean age of 6.6±2.9 ka). Its eruption initially produced an apron of pyroclastic-flow deposits that are preserved as far as 3 km northeast from its source vent. A lava dome then erupted, partly uplifting those pyroclastic deposits and extruding a Peléan spine at its summit.

Volume and Composition of Northern Harrat Rahat Eruptive Products Through Time

Estimating Eruptive Volumes

To better understand the temporal evolution of the magmatic system in northern Harrat Rahat, we estimate the volume of eruptive products through time. Most volcanic deposits exposed at the surface of northern Harrat Rahat are partially buried by younger volcanic products. Therefore, the total volume of these partially buried deposits cannot be estimated directly, and the concealed volumes must be inferred to estimate total eruptive volume. Quantifying the volume of eruptive products at mafic volcanic fields can be challenging because of their diffuse vent locations (that is, no central edifice) and commonly long-lived natures (greater than 1 m.y.; Kereszturi and others, 2013). Estimating the total volume of partially buried eruptive products by interpreting total areas and thicknesses of partially concealed units is a common approach (Hasenaka and Carmichael, 1985; Fierstein and others, 2011; Calvert and others, 2018) but is highly imprecise at Harrat Rahat because, in many instances, the locations of the source vents are unknown. Instead, we employ Monte Carlo simulation methods to estimate the cumulative volume of eruptive products from 1.2 Ma to present in northern Harrat Rahat.

In this simulation, we first define volume distributions for Harrat Rahat eruptions by estimating the area and average thicknesses of younger, well-exposed volcanic products (Stelten and others, 2020). To account for volume variations between different magma compositions, we define separate characteristic volumes for basalt and hawaiite, mugearite and benmoreite, and trachyte, incorporating published eruptive volumes where available (Dietterich and others, 2018, Murcia and others, 2015). The area of each well-exposed volcanic product was measured in ArcGIS based on 1- and 4-m digital elevation models (DEMs). Average thicknesses for each volcanic product and their source vent(s) were estimated by constructing a series of topographic cross sections (based on 1- and 4-m DEMs) from the proximal to distal parts of the deposits and measuring the average height of the feature above the surrounding topography assuming a planar sloping base. We estimate uncertainties of 30 percent in our average thickness estimates based on thickness variations observed in the cross sections. The volume of each trachyte or benmoreite dome was calculated from measurements of the dome diameter (at its base and near its top) and height, and assuming a conical frustum. Bulk volumes for eruptive products are adjusted to dense rock equivalent volumes (DRE) assuming densities of 2,500 kg/m^3 for basalt, hawaiite, and mugearite (Crosweller and others, 2012) and 2,400 kg/m^3 for benmoreite and trachyte, assuming densities of 1,500 kg/m^3 for scoria cones (McGetchin and others, 1974) and 2,200 kg/m^3 for trachyte pyroclastic deposits, and assuming that lava flows have densities equivalent to their theoretical density (that is, no correction applied).

The distribution of volumes calculated for well-exposed volcanic deposits (binned by compositions) is then fit with an appropriate probability distribution(s), and these probability distributions serve as a sampling scheme for the Monte Carlo simulation, similar to models used for forecasting future volcanic eruptions (Connor and others, 2012; Gallant and others, 2018). Because the well-exposed volcanic deposits that define the volume distributions are mostly younger than 250 ka, this approach assumes that the characteristic volumes of eruptive products after 250 ka at northern Harrat Rahat also characterize the older, partially buried volcanic deposits (extending back to 1.2 Ma).

Each Monte Carlo simulation randomly samples the appropriate volume distribution (that is, based on composition) to estimate a volume for each volcanic product in northern Harrat Rahat, and calculates the cumulative eruptive volume through time (using the assigned age for each eruptive unit). In this manner, volumes for the partially concealed eruptive units are estimated directly, and no surface area or thickness for these deposits is assumed. In the simulation, volumes are not modeled for volcanic products used to define the volume distributions. The Monte Carlo simulation runs 100 times, and the average of the 100 simulations is taken to be the best estimate for the volume of eruptive products as a function of time (fig. 8; Stelten and others, 2020). Two standard deviations of the 100 model runs at each time step are calculated and taken as the uncertainties of our volume calculations. The Monte Carlo results are presented in figure 8 and the model itself, including a full description, is provided by Stelten and others (2020).

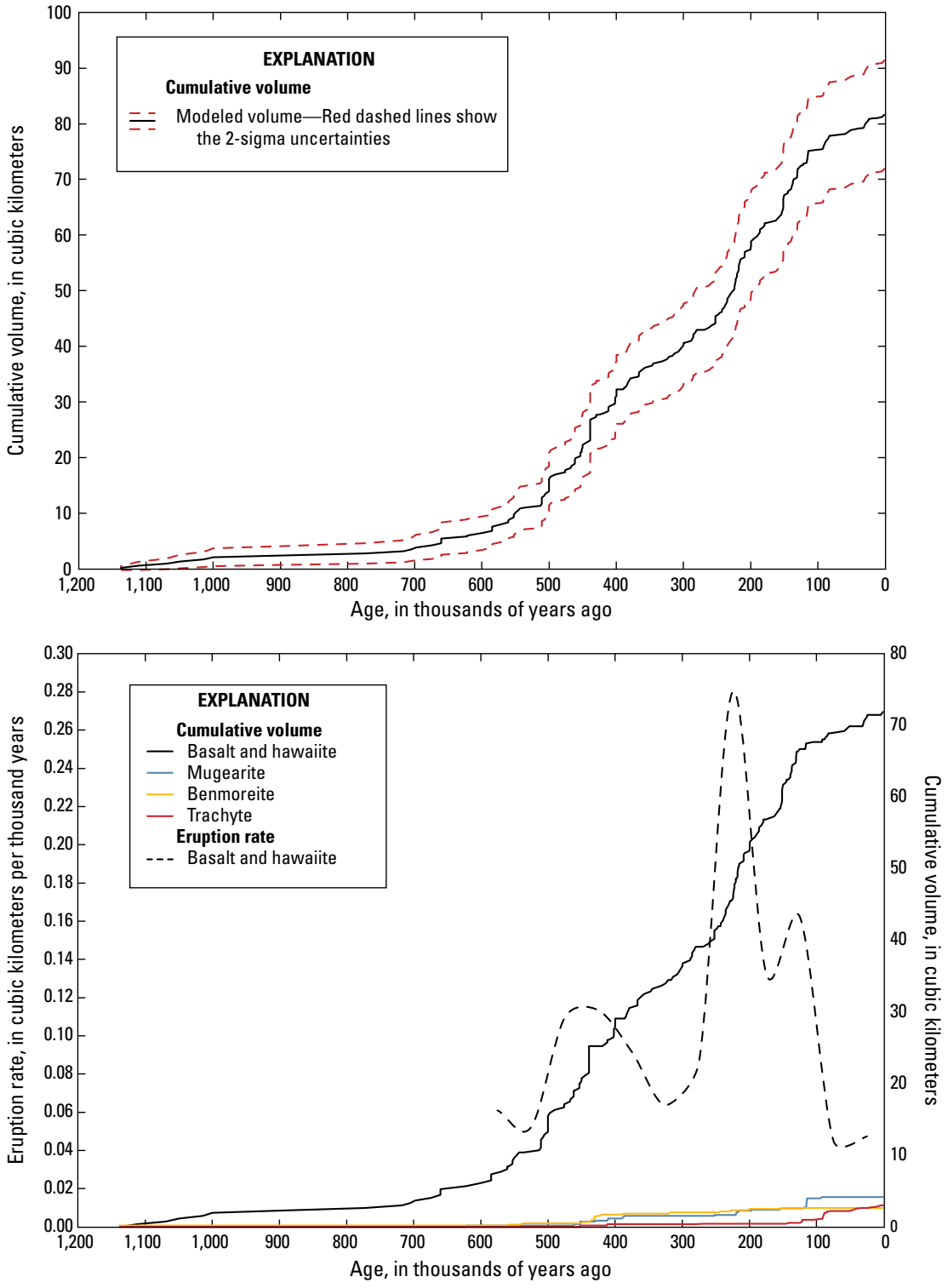

Figure 8. Plots showing age, in thousands of years ago versus cumulative volume (in cubic kilometers [km^3]) for northern Harrat Rahat. *A*, Age versus cumulative volume for all exposed and distinguished erupted compositions. Modeled volumes and associated 2σ uncertainties are the result of 100 Monte Carlo simulations (Stelten and others, 2020) in which total volumes are estimated for eruptive products that are partially concealed. *B*, Age versus cumulative volume separated by composition (based on the same Monte Carlo simulation as in panel *A*). The black, dashed curve represents the eruption rate of mafic (basalt and hawaiite) volcanism calculated in 50 thousand year (k.y.) intervals starting at 600 thousand years ago. Note that periods of evolved volcanism (that is, mugearite, benmoreite, and trachyte) are typically preceded by or coeval with high eruption rates for mafic volcanism. Also note that the last 120 k.y. are characterized by a lower eruption rate of basalt and hawaiite, but a higher than average eruption rate of trachytic magmas.

Eruption Rate, Volume, and Composition Through Time

The inferred cumulative volume of volcanic products erupted at northern Harrat Rahat from 1.2 Ma to present based on the Monte Carlo simulations is 82±10 cubic kilometers (km^3) DRE (fig. 8). Given that the model does not account for completely buried eruptive products, the volume of older eruptive products (greater than 570 ka) from stages 11 and 12 (and perhaps prior to that) are likely underestimated considerably, and the calculated approximately 82 km^3 is a lower limit for the complete volcanic productivity since 1.2 Ma. Applying the eruptive rate of the last 570 k.y. (0.14 km^3/k.y.) to the 1.2 m.y. span of documented volcanism would raise the total volume to approximately 170 km^3. Because of these uncertainties, we consider conclusions regarding the tempo, volume, and composition of eruptive products to be most reliable for the last 570 k.y.

In addition to modeling the cumulative volume of exposed eruptive products through time, we also estimate the cumulative volume of erupted material separated by composition (fig. 8*B*). On average, 65.5 km^3 of basalt, 6.4 km^3 of hawaiite, 4.2 km^3 of mugearite, 2.6 km^3 of benmoreite, and 3.0 km^3 of trachyte are accounted for over the past approximately 1.2 m.y., equating to proportions of approximately 80 percent basalt, 8 percent hawaiite, 5 percent mugearite, 3 percent benmoreite, and 4 percent trachyte by volume. As documented above, however, the proportions of magma types have changed over time. Basalts erupted persistently over the history of northern Harrat Rahat, but eruptions of intermediate to evolved magmas appear to be temporally punctuated (fig. 8*B*). Intermediate magmas (mugearites and benmoreites) erupted periodically over the exposed history of northern Harrat Rahat, with the oldest exposed benmoreite (1,137.9±3.1 ka) similar in age to the oldest exposed basalt (1,112.1±17.6 ka). In contrast, 86 volume percent of the trachytes known for northern Harrat Rahat erupted over the past 180 k.y., with only minor trachyte production prior to this time.

Considering the cumulative volume of all exposed and distinguished eruptive products over the past 570 k.y., the average eruptive flux for northern Harrat Rahat would be approximately 0.14 km^3/k.y. This is in broad agreement with the 0.2 km^3/k.y. eruptive flux estimated for the entirety of Harrat Rahat over the past 10 m.y. (Camp and Roobol, 1989). The eruptive flux in northern Harrat Rahat is an order of magnitude larger than that at the continental Auckland volcanic field, New Zealand (0.007–0.013 km^3/k.y.; Kreszturi and others, 2013), one of the few intraplate mafic volcanic fields for which comparable geochronologic data are available, although the driving forces behind volcanism in these volcanic fields are likely different (Sprung and others, 2007). Northern Harrat Rahat's eruptive flux is several orders of magnitude lower than those of other types of intra-plate basalts, such as flood basalt provinces (600–800 km^3/k.y. for the Siberian Traps, 150 km^3/k.y. for the Steens Basalt Member of the Columbia River Basalt) and modern Kīlauea (100–200 km^3/k.y.) (Swanson, 1972; Lipman and Calvert, 2013; Burgess and Bowring, 2015; Mahood and Benson, 2017).

It is apparent from the ages and volumes for northern Harrat Rahat that volcanism was episodic. The time intervals from approximately 570 to 500 ka, 375 to 255 ka, and 125 ka to present were characterized by lower eruption rates (0.07–0.08 km^3/k.y.), whereas the periods from approximately 500 to 400 ka, 250 to 200 ka, and 155 to 125 ka had higher eruption rates (0.17–0.28 km^3/k.y.; fig. 8). These magmatic stages are most easily understood by considering the eruption rate of mafic (basalt and hawaiite) eruptions though time. If we take the lower mafic eruption rate over the past 570 ka as a baseline, then the background level of mafic output at northern Harrat Rahat was between 0.04 and 0.06 km^3/k.y., whereas during periods of increased volcanism the mafic eruption rate rose to between 0.1 and 0.3 km^3/k.y. (fig. 8*B*). Importantly, periods of increased mafic eruption rate typically preceded, or were concurrent with, periods of intermediate to evolved volcanism, most notably at approximately 475 ka, 225 ka, and 125 ka, as has been observed at other well-studied mafic volcanic fields (for example, Springerville volcanic field, Arizona, United States; Condit and Connor, 1996). This observation suggests that the increased eruption rate of mafic magmas records periods of increased input of mantle-derived magmas into the crust, which in turn spawns the production of evolved magmas.

The Spatial and Compositional Evolution of Volcanism at Northern Harrat Rahat Through Time

Recent geologic mapping and geochronologic and geochemical data suggest that the spatial distribution of eruptive vents and the relative proportion of mafic, intermediate, and silicic eruptions in northern Harrat Rahat have changed over time (table 4). Key observations include the following.

1. *The spatial distribution of eruptions has changed over time.*—From 570 to 180 ka, basalts erupted from all parts of the volcanic field, including the subsidiary vent axis and the entire length of the main vent axis. Intermediate and evolved magmas erupted exclusively from the main vent axis. After 180 ka, volcanism along the subsidiary vent axis seems to have waned, and nearly all magmas, regardless of composition, erupted along the main vent axis (table 4, fig. 9).
2. *The proportion of intermediate to evolved eruptions increased over time.*—From 570 to 180 ka, basalt accounts for approximately 87 percent (46 km^3) of the total volume of eruptive products, whereas hawaiite, mugearite, benmoreite, and trachyte account for approximately 4 percent (2 km^3), 4 percent (2 km^3), 4 percent (2 km^3), and 1 percent (0.4 km^3) of the total volume, respectively. After 180 ka, basalt accounts for only approximately 55 percent (11 km^3) of the volume of eruptive products, whereas hawaiite, mugearite, benmoreite, and trachyte account for approximately 23 percent (4 km^3), 9 percent (2 km^3), 1 percent (0.1 km^3), and 13 percent (3 km^3) of the total volume, respectively (fig. 9).

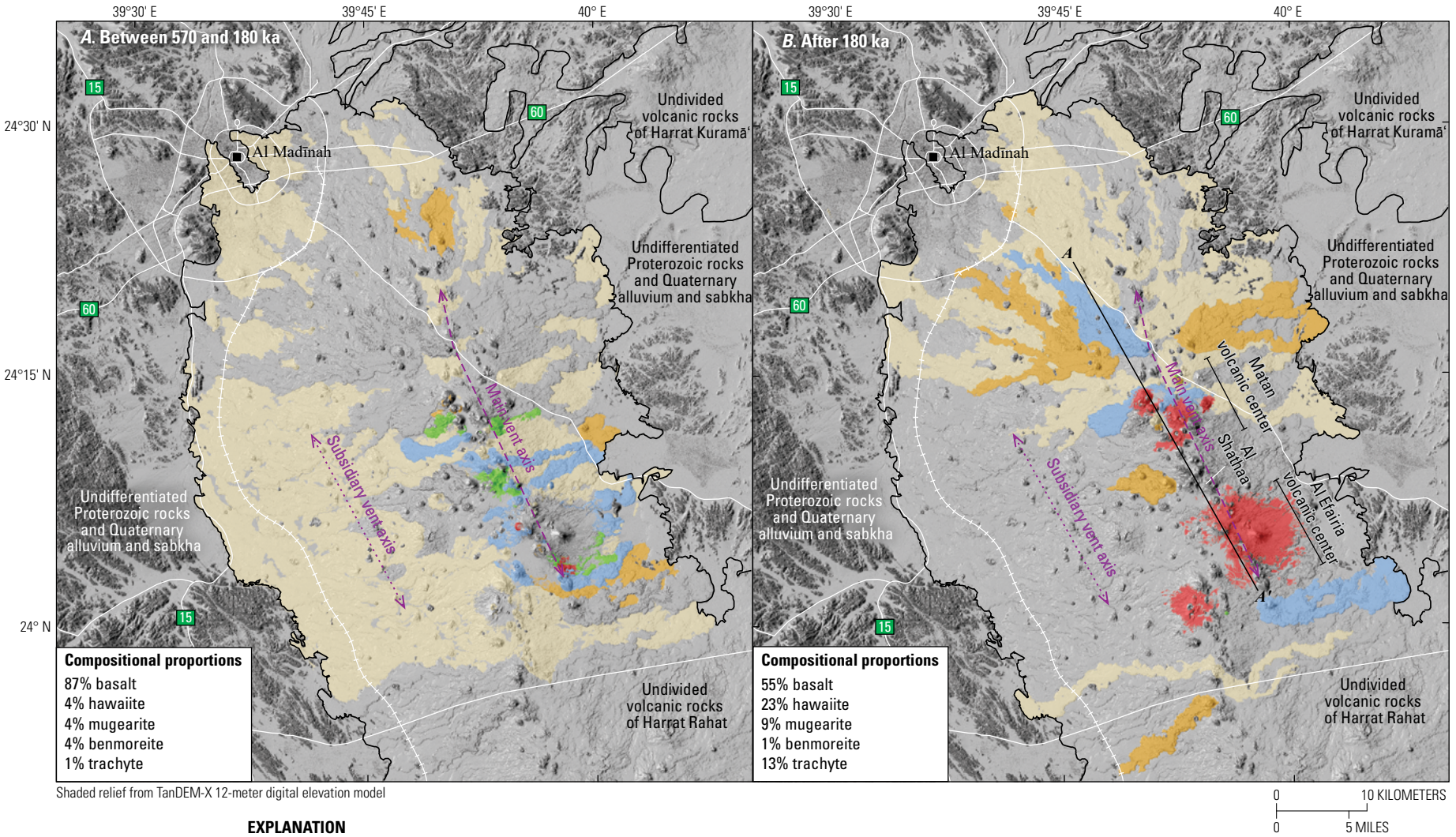

Figure 9. Map of the study area in northern Harrat Rahat, displaying the composition of eruptive products for different time periods. *A,* Map of all volcanic products that erupted between 570 and 180 thousand years ago (ka). Mafic magmas (basalt and hawaiite) erupted from all parts of the study area, including both the main and subsidiary vent axes. The main vent axis is dominated by eruption of basalt, hawaiite, mugearite, and benmoreite, with only minor trachyte found exclusively in the Al Efairia volcanic center. *B*, Map of all volcanic products that erupted after 180 ka. No eruptions occurred along the subsidiary vent axis, and nearly all volcanism occurred along the main vent axis (except for two eruptions located in the northwest corner of the study area). Note that since 180 ka, the north part of our field area is dominated by basalt and hawaiite eruptions, the Matan volcanic center hosts the entire range of compositions (basalt to trachyte), and the Al Efairia volcanic center erupted only trachyte. Cross section *A*–*A'* is shown in figure 11. km, kilometer; %, percent.

3. *After 180 ka, the composition of eruptive products varied along the length of the main vent axis.*—From 570 to 180 ka, basalts erupted along the entire length of the main vent axis. Hawaiite, mugearite, and benmoreite erupted from the main vent axis within and between the Matan and Al Efairia volcanic centers. Trachyte erupted exclusively from the Al Efairia volcanic center (fig. 9). After 180 ka, three different regions along the main vent axis can be defined based on the compositions erupted. North of the Matan volcanic center and south of the Al Efairia volcanic center, volcanism was dominated by basalt and hawaiite. Within the Al Efairia volcanic center, only trachyte erupted with no intermediate or mafic magmas. The Matan volcanic center represents a transition zone where the whole compositional spectrum (basalt to trachyte) erupted. Importantly, volcanism in each of these regions was coeval, yet displayed a different compositional range of eruptive products (figs. 9, 10).

It is well accepted that volcanism in systems driven by mantle-decompression melting is ultimately powered by the input of basalts into the crust. Therefore, it is likely that all volcanism in northern Harrat Rahat that is younger than 180 ka, regardless of composition, was driven by basaltic intrusions into the crust underlying the main vent axis. This implies that some systematic process prevented the formation and (or) eruption of evolved magmas along the northern and southern parts of the main vent axis but promoted trachyte formation and impeded eruption of basalt in the central part of the main vent axis near the Al Efairia volcanic center (fig. 9).

The region of the main vent axis within and between the Matan and Al Efairia volcanic centers has the highest density of volcanic vents (figs. 3, 6) and the highest topography

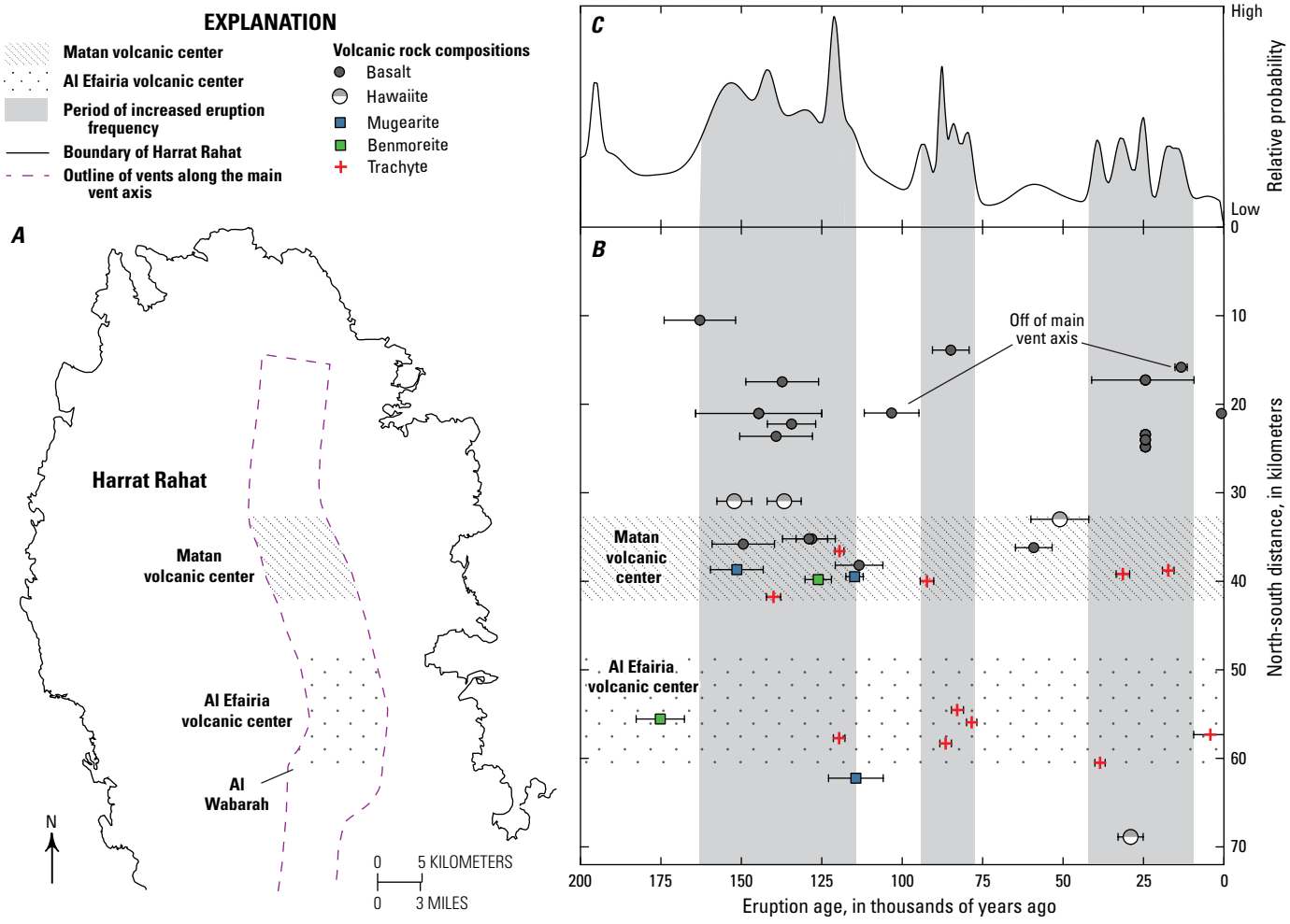

Figure 10. Age, location, and composition of eruptions that occurred less than 180 thousand years ago in northern Harrat Rahat. *A*, Simplified map of the study area. *B*, Eruption age versus the north-south distance of the vent location within the study area, where 0 marks the north end of the study area. All eruptions took place along the main vent axis, unless otherwise noted. Error bars show the uncertainty in the eruption age. *C*, Probability density function (from fig. 5) of eruption ages from 200 ka to present. Vertical gray fields indicate periods of increased eruptive activity, based on the probability density function. Note that the compositions of coeval eruptions vary systematically along the main vent axis from basalt dominated north of the Matan volcanic center to trachyte dominated in the Al Efairia volcanic center.

relative to the rest of the study area (figs. 2, 11), suggesting that this region of the main vent axis hosted the majority of eruptions throughout the history of northern Harrat Rahat. In turn, the crust underlying this region of the main vent axis received the largest cumulative flux of mantle-derived basalt over the past 1.2 m.y. (or longer), some of which reached the surface, whereas other magma batches stalled as mafic intrusions. In contrast, the main vent axis north of the Matan volcanic center and south of the Al Efairia volcanic center is at a lower elevation, which suggests that these regions of

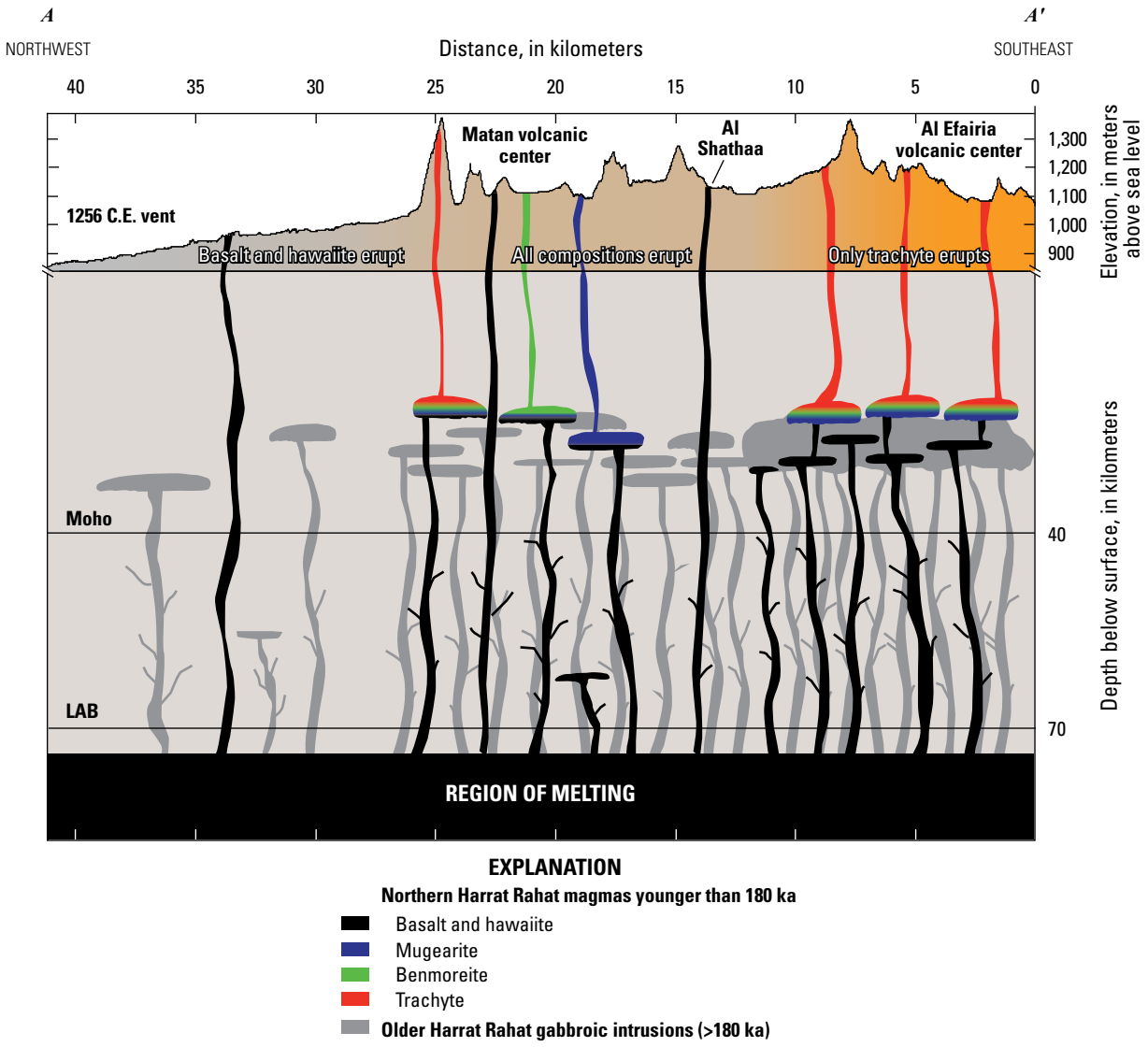

Figure 11. Cross section *A*–*A*′ (location in fig. 9) showing a petrogenetic model of the state of the crust and magmatic system beneath northern Harrat Rahat from 180 thousand years ago (ka) to present. The model is constructed on a cross section that runs northwest-southeast along the length of the main vent axis (see fig. 9). The upper part of the figure is a topographic profile along the cross section line, highlighting the difference in thickness of volcanic deposits beneath the trachyte volcanic centers and north of the trachyte centers (vertical exaggeration is approximately 75:1). Note that the y-axis of the upper and lower panels has different units, and that there is a slight break in the y-axis (850 to 0 meters not shown). Beneath the Al Efairia volcanic center is a mafic intrusive complex that may have differentiated sufficiently to produce magmatic density traps or may be too hot and ductile to fracture easily, in either case hindering the ascent of younger basaltic magmas. Mafic magmas in this region stall and differentiate to more evolved compositions before erupting. Beneath the Matan volcanic center, the mafic intrusive complex is less well developed, which allows some basalt to erupt unhindered and others to stall in the crust and differentiate to more evolved compositions before erupting (Stelten and others, 2018). Northwest (and southeast) of the trachytic centers, no mafic intrusive complex exists in the crust; basalts thus can reach the surface and erupt unhindered. Mohorovičić discontinuity (Moho) and lithosphere-asthenosphere boundary (LAB) depths from Yao and others (2017). The depths of this intrusive complex and magmas in this diagram is schematic.

the main vent axis have hosted fewer eruptions and therefore that the crust underlying these regions received a smaller cumulative flux of mantle-derived basalt.

We hypothesize that the increased proportion of intermediate to evolved magmas (relative to previous eruptive stages) and the compositional variation of eruptive products observed along the length of the main vent axis after 180 ka reflect changes in the thermal, rheological, and (or) chemical nature of the crust that underlies the main vent axis, because of the effects of prolonged intrusion of mafic magmas into the crust (figs. 9, 10, 11). We interpret that the lack of mafic eruptions near the Al Efairia volcanic center resulted from production of a mafic intrusive complex in the crust underlying this region of the main vent axis, which had been the most volcanically active over the past 1.2 m.y. The mafic intrusive complex may have differentiated sufficiently to produce magmatic density traps or may be too hot and ductile to fracture easily, in either case retarding the ascent of younger basaltic magmas (fig. 11). Instead, these magmas stalled and produced trachytes, likely through fractional crystallization and (or) partial melting of antecedent intrusions. Less cumulative basaltic flux beneath the north end of northern Harrat Rahat failed to create a sizable intrusive complex, so basaltic magmas remained able to ascend though the crust relatively unimpeded (fig. 11). The Matan volcanic center overlies a transition zone where a mafic intrusive complex has not fully developed, such that some mafic magmas stall within the crust and differentiate (in the broad sense) producing intermediate and evolved magmas, and others erupt unhindered. The observation that trachytes older than 180 ka vented exclusively within the Al Efairia volcanic center supports the concept that the region of the crust beneath the Al Efairia volcanic center had been modified to the greatest degree prior to 180 ka, and in turn is the region of the crust most likely to host a well-developed mafic intrusive complex.

This interpretation has important implications for future volcanism at northern Harrat Rahat. Our results suggest that (1) future volcanism is likely to be focused along the main vent axis and volcanism along the subsidiary vent axis is of low probability, (2) future volcanism north of the Matan volcanic center and south of the Al Efairia volcanic center will likely be basalt or hawaiite lavas (such lavas are fluid and are capable of traveling 10–20 km; Dietterich and others, 2018), (3) volcanism within the Matan volcanic center could be any composition from basalt to trachyte and may occur in clustered sequences initiated by periods of elevated mafic magma flux similar to prior volcanism (Stelten and others, 2018), and (4) volcanism within the Al Efairia volcanic center will likely be trachytic.

Recurrence Interval of Volcanism

An important consideration when characterizing the eruptive behavior of a volcanic system is the volcanic recurrence interval (that is, average time between eruptions). Previous estimates of the recurrence interval for northern Harrat Rahat have varied by four orders of magnitude, from 70 to 13,300 years (El Difrawy and others, 2013), largely because of a lack of age determinations for volcanic rocks in northern Harrat Rahat available at the time of these studies. Here we integrate $^{40}Ar/^{39}Ar$ and ^{36}Cl ages from the SGS-USGS project with eruption age estimates from stratigraphic relations and paleomagnetic analysis (Downs and others, 2019; Robinson and Downs, 2023) to reevaluate the volcanic recurrence interval in northern Harrat Rahat. In this analysis, we consider only volcanic deposits that formed after 180 ka because it is likely that the volcanic record prior to 180 ka is incomplete because of concealment beneath younger eruptive products, and because there was a change in the spatial and compositional behavior of volcanism in northern Harrat Rahat at about 180 ka (see The Spatial and Compositional Evolution of Volcanism at Northern Harrat Rahat Through Time section).

To evaluate the volcanic recurrence interval, we order the eruptive products based on their measured (or estimated) ages and stratigraphic relations, and then calculate the interval time between successive eruptions. Interval times are plotted on a cumulative probability diagram and modeled using a Poisson distribution and a mixed exponential distribution, which represent two possible interpretations of eruptive behavior at northern Harrat Rahat (fig. 12*A*). Poisson distributions have commonly been used to describe volcanic processes at Harrat Rahat and worldwide (Klein, 1982; Scott and others, 1995; El Difrawy and others, 2013; Runge and others, 2014). In a Poisson distribution, the probability that an eruption will occur during a specified period (for example, in the next year or next 100 years) is a function of the average recurrence interval for the volcanic field. This relation is calculated from an exponential distribution for the probability $P\{T \le t\}$ that an eruption will occur in a time T that is less than or equal to a time period t:

$$P\{T \le t\} = F(t) = 1 - e^{-\frac{t}{r}} \quad (1)$$

where

$F(t)$ is the probability distribution function;
r is the average recurrence interval; and
t is the specified time period.

Given that 56 eruptions have been identified over the last 180 k.y., the average recurrence interval for Harrat Rahat is 3.2 k.y. However, it is clear from figure 12*A* that a Poisson distribution provides a poor fit to the data for northern Harrat Rahat.

An alternative to a Poisson distribution is a mixed exponential distribution, which is applicable for eruption intervals that can be divided into two populations, one of short intervals and one of long intervals (Nathenson, 2001; Christiansen and others, 2007). Conceptually, this represents a system that is that characterized by two different states, one characterized by a longer recurrence interval and one by a shorter recurrence interval. The probability of an eruption occurring in either of these states is governed by an exponential distribution, with a known or estimated average recurrence interval:

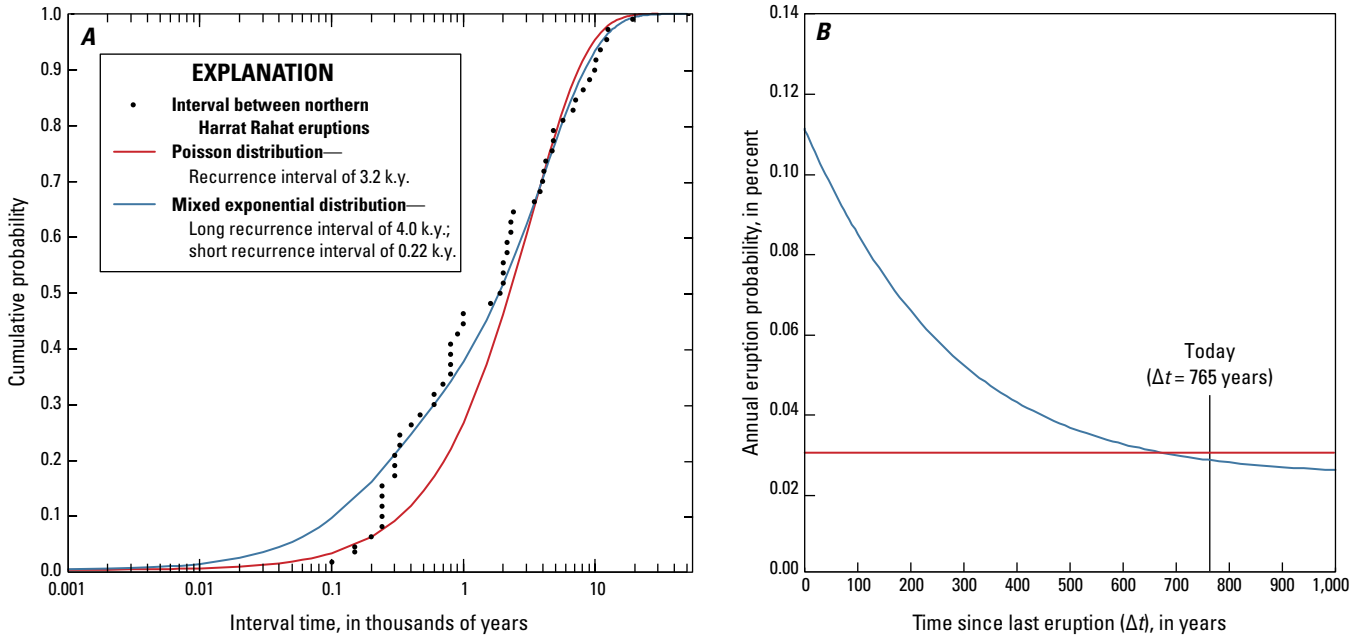

Figure 12. Plots of recurrence intervals in northern Harrat Rahat and their implications for eruption probabilities. Data used in generating this plot can be found in Stelten and others (2020). *A*, Cumulative probability versus interval time (thousand years [k.y.]). Interval times are shown for all eruptions that occurred since 180 thousand years ago, using both absolute ages and those estimated from stratigraphic relations or paleomagnetic data. These data are best fit by a mixed exponential model with a long interval of 4.0 k.y. and a short interval of 0.22 k.y. (blue curve). *B*, Annual eruption probability versus the time since the previous eruption (in years). Note that at present (765 years since the last eruption), the annual probability of an eruption is similar between the mixed exponential and Poisson distributions at about 0.03 percent.

$$P\{T \le t\} = F(t) = 1 - p_1 e^{-\frac{t}{r_1}} - p_2 e^{-\frac{t}{r_2}} \quad (2)$$

where

p_1 is the fraction of short intervals ($\frac{n_1}{n_1 + n_2}$);

r_1 is the average recurrence interval for the short intervals ($\frac{1}{n_1}\sum_{i=1}^{n_1} t_i$); and

n_1 is the number of short intervals; and

p_2, r_2, and n_2 are the equivalent parameters for the long intervals.

If it were possible to know which state the system is in, then the appropriate recurrence interval could be used in a Poisson model. However, in practice it is difficult to assess which state a volcanic system is in.

When applied to the age data for volcanic rocks in northern Harrat Rahat (fig. 12*A*), the mixed exponential model, with a long recurrence interval of 4.0 k.y. and a short recurrence interval of 0.22 k.y. (assigning 80 percent of the measured intervals to the long-repose state and 20 percent to the short-repose state), yields a significantly better fit to the data compared to a Poisson distribution. These observations suggest that volcanism at northern Harrat Rahat is best characterized by a mixed exponential model. Geologic observations support the idea that volcanism in northern Harrat Rahat is characterized by two distinct states, one of long eruption intervals and one of short eruption intervals. For example, the Five Fingers flows (located in northeastern Harrat Rahat (figs. 6, 7), represent three distinct eruptions that occurred at approximately 24 ka. Each of these eruptions has an identical eruption age (within analytical uncertainty), but each eruption has distinct chemical and paleomagnetic characteristics that demonstrate they occurred at slightly different times (Downs and others, 2019; Robinson and Downs, 2023), perhaps separated by hundreds of years. Similarly, two trachyte eruptions occurred near simultaneously from distinct vents in the Al Efairia volcanic center at approximately 80 ka, based on identical $^{40}Ar/^{39}Ar$ eruption ages (within uncertainty) and identical paleomagnetic remanent directions. Lastly, field relations and $^{40}Ar/^{39}Ar$ dating demonstrate that mafic (basalt and hawaiite) and intermediate (mugearite and benmoreite) eruptions within the Matan volcanic center over the last 180 k.y. were closely related in time, typically yielding eruption ages that are indistinguishable within analytical uncertainty (Stelten and others, 2018, 2023). These examples provide evidence that multiple distinct eruptions can occur over short time periods, supporting a mixed exponential model. It is likely that similar scenarios occurred in older volcanic deposits but cannot be recognized because of obscured field relations.

Eruption Probabilities

The recurrence intervals determined above can be used to assess the probability of future eruptions in northern Harrat Rahat (fig. 12*B*). The probability of an eruption occurring sometime in the future is a function of the characteristic volcanic recurrence interval(s) and the time-period considered. In the case of a Poisson distribution, the conditional probability of an eruption occurring within some timeframe is independent of the time elapsed since the last eruption and is simply a function of the recurrence interval (fig. 12*B*). In contrast, an important aspect of mixed exponential models is that conditional probabilities can be calculated for an eruption occurring between time Δt and time $t + \Delta t$, where Δt is the time passed since the last eruption and t is the specified time period of interest (for example, the next year or next 100 years). This conditional probability is calculated from the distribution function $F(t)$ (eq. 2) as follows:

$$P\{\Delta t \le T \le t + \Delta t \,|\, T > \Delta t\} = 1 - \frac{1 - F\left(t + \Delta t\right)}{1 - F\left(\Delta t\right)} \qquad (3)$$

where

$F(t)$ is the distribution function from eq. 2;
Δt is the time passed since the last eruption;
t is the specified time period of interest.

Using the Poisson and mixed exponential distributions described in the previous section and shown in figure 12*A*, we calculate annual eruption probabilities for the present day. Data used in these calculations, and in the construction figure 12*A*, are included in Stelten and others (2020). If volcanism at Harrat Rahat is characterized by a Poisson distribution with a recurrence interval of 3.2 k.y., then the probability of an eruption occurring within the next year is 0.03 percent regardless of the time elapsed since the previous eruption (fig. 12*B*). If volcanism at Harrat Rahat is characterized by a mixed exponential model, with a long recurrence interval of 4.0 k.y. and a short recurrence interval of 0.22 k.y., and given that the most recent eruption at Harrat Rahat occurred in 1256 C.E. (Δt=765 years), then the probability of an eruption occurring within the next year is also 0.03 percent. Thus, enough time has passed since the last eruption that the present-day annual eruption probabilities are indistinguishable between the Poisson and mixed exponential models.

Although present-day eruption probabilities are similar between the two models, they differ when considering annual eruption probabilities immediately after an eruption (fig. 12*B*). In a Poisson model the conditional probability remains at 0.03 percent because the Poisson model is not time dependent. In contrast, when using the mixed exponential model, the conditional probability would be 0.1 percent in the year immediately following an eruption. As time passes (that is, as Δt increases), this elevated eruption probability quickly decays away until the long-term eruption probability is reached (fig. 12*B*).

Conclusions

$^{40}Ar/^{39}Ar$ and ^{36}Cl dating of volcanic deposits in combination with geologic mapping, geochemistry, and paleomagnetic analyses (Downs and others, 2019; Robinson and Downs, 2023) allow for a detailed examination of the timing and compositional evolution of volcanism within northern Harrat Rahat. Results show that all exposed volcanic products in northern Harrat Rahat erupted after 1.2 Ma and that 90 percent (214 of the 239 units) of deposits exposed on the surface of the study area erupted after 570 ka (figs. 5, 6). Only two Holocene eruptions occurred within northern Harrat Rahat: the historical eruption of the basalt of Al Labah (unit bla) in 1256 C.E. and the eruption of the trachyte of Um Rgaibah (unit trg) at 4.2±5.2 ka (or 6.6±2.9 ka combining ^{36}Cl and $^{40}Ar/^{39}Ar$ results). Eight eruptive products from within the study area that were previously interpreted as Holocene (Camp and Roobol, 1989) are shown to have erupted prior to 13 ka.

Based on exposed rocks, the cumulative volume of volcanic products erupted from northern Harrat Rahat over the past 1.2 m.y. is estimated to be approximately 82 km^3 DRE, but this is a lower limit because of concealment of eruptive products chiefly older than 570 ka. Applying the eruptive rate of the last 570 k.y. (0.14 km^3/k.y.) to the 1.2 m.y. span of documented volcanism would raise the total volume to approximately 170 km^3. Accordingly, this study draws conclusions mainly from the last 570 k.y. where the record is relatively complete. The cumulative eruptive products of the last 1.2 m.y. in northern Harrat Rahat consist of approximately 80 (volume) percent basalt, 8 percent hawaiite, 5 percent mugearite, 3 percent benmoreite, and 4 percent trachyte, but the proportion of intermediate and evolved magmas increased with time. Volcanism in northern Harrat Rahat is episodic with alternating periods of a low mafic eruption rate (0.04 to 0.06 km^3/k.y.) and a high mafic eruption rate (0.1 to 0.3 km^3/k.y.). Importantly, episodes of intermediate (mugearite and benmoreite) to evolved (trachyte) volcanism are typically preceded by, or are coeval with, periods of a high mafic eruption rate, supporting a causal link between influxes of mafic magma into the crust and the production of evolved derivative magmas within the crust.

The proportions of mafic, intermediate, and evolved volcanism as well as the spatial distribution of volcanic products in northern Harrat Rahat changed over time. Prior to 180 ka, volcanism was more diffuse. Basaltic magmas erupted from both an eastern main vent axis and a western subsidiary vent axis, whereas intermediate to evolved magmas erupted exclusively from the main vent axis. With two known exceptions, nearly all volcanism after 180 ka (regardless of composition) became focused along the main vent axis, and the proportion of intermediate and evolved magmatism increased markedly (fig. 9). After 180 ka, the composition of volcanism also varied along the main vent axis from basalt dominated in the north to trachyte dominated in the south. This difference may result from growth of a mafic

intrusive complex beneath the southern part of the main vent axis, which had been the most volcanically active region of northern Harrat Rahat over the past 1.2 m.y. (documented by its high constructional relief and high density of volcanic vents). The mafic intrusive complex may have differentiated sufficiently to produce magmatic density traps and (or) may be too hot and ductile to fracture easily, in both cases retarding the ascent of younger basaltic magmas (fig. 11). Instead, these magmas stalled and produced trachyte. Lesser basaltic inputs beneath the north end of the main vent axis failed to create a sizable intrusive complex, so basaltic magmas were able to ascend though the crust relatively unhindered. These factors suggest that future eruptions in northern Harrat Rahat are most probable from the main vent axis, and that eruptions from the north part of the study area are likely to be mafic (basalt or hawaiite), whereas eruptions from the south part of the study area are likely to be more evolved and potentially explosive.

Lastly, these age data and field relations allow for a reassessment of the volcanic recurrence interval at Harrat Rahat. Eruption age determinations suggest that volcanism in northern Harrat Rahat over the past 180 k.y. is poorly described by a Poisson distribution with an average recurrence interval of 3.2 k.y. (fig. 12*A*). Instead, the frequency of eruptions is better described using a mixed exponential distribution, which is applicable for volcanic systems characterized by two different eruptive states, one of long recurrence intervals and one of short recurrence intervals. The preferred model for northern Harrat Rahat uses a long recurrence interval of 4.0 k.y. and a short recurrence interval of 0.22 k.y. and yields a present-day annual eruption probability of approximately 0.03 percent.

Acknowledgments

This work was supported by funding from the U.S. Geological Survey and the Saudi Geological Survey. We are grateful to Katie Sullivan, Brandon Swanson, Dean Miller, and James Saburomaru for their invaluable assistance in preparing and analyzing samples for this study.

We thank Patrick Muffler and Manuel Nathenson for their constructive reviews that improved our interpretations and presentation, and we thank John Mark Brigham and Monica Erdman for their skilled edits of the manuscript.

References Cited

Almond, D.C., 1986a, The relation of Mesozoic-Cainozoic volcanism to tectonics in the Afro-Arabian dome: Journal of Volcanology and Geothermal Research, v. 28, p. 225–246, https://doi.org/10.1016/0377-0273(86)90024-7.

Almond, D.C., 1986b, Geological evolution of the Afro-Arabian dome: Tectonophysics, v. 131, p. 301–332, https://doi.org/10.1016/0040-1951(86)90180-0.

Al-Samhūdī, A.B.A.A., 1488 [edited and reprinted in 2001], Wafāʻ Al-Wafāʻ Bi Akhbār Dār Al-Muṣṭafā: London, Al-Furqān Islamic Heritage Foundation, 2,615 p.

Bosworth, W., Huchon, P., and McClay, K., 2005, The Red Sea and Gulf of Aden Basins: Journal of African Earth Sciences, v. 43, p. 334–378, https://doi.org/10.1016/j.jafrearsci.2005.07.020.

Brown, G.F., Schmidt, D.L., and Huffman, A.C., Jr., 1989, Geology of the Arabian Peninsula—Shield area of western Saudi Arabia: U.S. Geological Survey Professional Paper 560–A, 188 p.

Burgess, S.D., and Bowring, S.A., 2015, High-precision geochronology confirms voluminous magmatism before, during, and after Earth's most severe extinction: Science Advances, v. 1, https://doi.org/10.1126/sciadv.1500470.

Cabanis, B., and Lecolle, M., 1989, Le diagramme La/10-Y/15-Nb/8—Un outil pour la discrimination des series volcaniques et lamise en evidence des processus demelange et/ou de contamination crustale: Compte Rendus de I'Académie des Sciences Series, v. 309, p. 2023–2029.

Calvert, A.T., Fierstein, J., and Hildreth, W., 2018, Eruptive history of Middle Sister, Oregon Cascades, United States—Product of a late Pleistocene eruptive episode: Geosphere, v. 14, p. 2118–2139, https://doi.org/10.1130/GES01638.1.

Calvert, A.T., and Lanphere, M.A., 2006, Argon geochronology of Kilauea's early submarine history: Journal of Volcanology and Geothermal Research, v. 151, p. 1–18, https://doi.org/10.1016/j.jvolgeores.2005.07.023.

Calvert, A.T., and Sisson, T.W., 2023, Cenozoic tectonics of the western Arabia Plate related to harrat magmatism near Al Madīnah, Kingdom of Saudi Arabia, chap. B *of* Sisson, T.W., Calvert, A.T., and Mooney, W.D., eds., Active volcanism on the Arabian Shield—Geology, volcanology, and geophysics of northern Harrat Rahat and vicinity, Kingdom of Saudi Arabia: U.S. Geological Survey Professional Paper 1862 [also released as Saudi Geological Survey Special Report SGS–SP–2021–1], 28 p., https://doi.org/10.3133/pp1862B.

Camp, V.E., Hooper, P.R., Roobol, M.J., and White, D.L., 1987, The Madinah eruption, Saudi Arabia—Magma mixing and simultaneous extrusion of three basaltic chemical types: Bulletin of Volcanology, v. 49, p. 489–508, https://doi.org/10.1007/BF01245475.

Camp, V.E., and Roobol, M.J., 1989, The Arabian continental alkali basalt province; Part I— Evolution of Harrat Rahat, Kingdom of Saudi Arabia: Geological Society of America Bulletin, v. 101, p. 71–95, https://doi.org/10.1130/0016-7606(1989)101%3C0071:TACABP%3E2.3.CO;2.

Camp, V.E., and Roobol, M.J., 1991, Geologic map of the Cenozoic lava field of Harrat Rahat, Kingdom of Saudi Arabia: Ministry of Petroleum and Mineral Resources, Directorate General of Mineral Resources, 37 p.

Camp, V.E., and Roobol, M.J., 1992, Upwelling asthenosphere beneath western Arabia and its regional implications: Journal of Geophysical Research, v. 97, p. 15255–15271, https://doi.org/10.1029/92JB00943.

Christiansen, R.L., Lowenstern, J.B., Smith, R.B., Heasler, H., Morgan, L.A., Nathenson, N., Mastin, L.G., Muffler, L.J.P., and Robinson, J.E., 2007, Preliminary assessment of volcanic and hydrothermal hazards in Yellowstone National Park and vicinity: U.S. Geological Survey Open-File Report 2007–1071, 98 p., https://doi.org/10.3133/ofr20071071.

Coleman, R.G., 1993, Geologic evolution of the Red Sea: Oxford Monographs on Geology and Geophysics, v. 34, 186 p.

Coleman, R.G., Gregory, R.T., and Brown, G.F., 1983, Cenozoic volcanic rocks of Saudi Arabia: U.S. Geological Survey Open-File Report 83-788, 86 p., https://doi.org/10.3133/ofr83788.

Coleman, R.G., and McGuire, A.V., 1988, Magma systems related to the Red Sea opening: Tectonophysics, v. 150, p. 77–100, https://doi.org/10.1016/0040-1951(88)90296-X.

Condit, C.D., and Connor, C.B., 1996, Recurrence rates of volcanism in basaltic volcanic fields—An example from the Springerville volcanic field, Arizona: Geological Society of America Bulletin, v. 108, p. 1225–1241, https://doi.org/10.1130/0016-7606(1996)108%3C1225:RROVIB%3E2.3.CO;2.

Connor, L.J., Connor, C.B., Meliksetian, K., and Savov, I., 2012, Probabilistic approach to modeling lava flow inundation—A lava flow hazard assessment for a nuclear facility in Armenia: Journal of Applied Volcanology, v. 1, https://doi.org/10.1186/2191-5040-1-3.

Cox, K.G., Bell, J.D., and Pankhurst, R.J., 1979, The interpretation of igneous rocks: London, George Allen and Unwin, 450 p., https://doi.org/10.1007/978-94-017-3373-1.

Crassard, R., Petraglia, M.D., Drake, N.A., Breeze, P., Gratuze, B., Alsharekh, A., Arbach, A., Groucutt, H.S., Khalidi, L., Michelsen, N., Robin, C.J., and Schiettecatte, J., 2013, Middle Palaeolithic and Neolithic occupations around Mundafan Palaeolake, Saudi Arabia—Implications for climate change and human dispersals: PLoS ONE, v. 8, https://doi.org/10.1371/journal.pone.0069665.

Crosweller, H.S., Arora, B., Brown, K.S., Cottrell, E., Deligne, N.I., Guerrero, N.O., Hobbs, L., Kiyosugi, K., Loughlin, S.C., Lowndes, J., Nayembil, M., Siebert, L., Sparks, R.S.J., Takarada S., and Venzke, E., 2012, Global database on large magnitude explosive volcanic eruptions (LaMEVE): Journal of Applied Volcanology, v. 1, 13 p., https://doi.org/10.1186/2191-5040-1-4.

Dalrymple, G.B., Alexander, E.C., Lanphere, M.A., and Kraker, G.P., 1981, Irradiation of samples for $^{40}Ar/^{39}Ar$ dating using the Geological Survey TRIGA reactor: U.S. Geological Survey Professional Paper 1176, 55 p., https://doi.org/10.3133/pp1176.

Desilets, D., Zreda, M., Almasi, P.F., and Elmore, D., 2006, Determination of cosmogenic ^{36}Cl in rocks by isotope dilution—Innovations, validation and error propagation: Chemical Geology, v. 233, p. 185–195, https://doi.org/10.1016/j.chemgeo.2006.03.001.

Dietterich, H.R., Downs, D.T., and Stelten, M.E., 2023, Lava flow emplacement in Harrat Rahat with implications for eruptions in mafic volcanic fields, chap. E *of* Sisson, T.W., Calvert, A.T., and Mooney, W.D., eds., Active volcanism on the Arabian Shield—Geology, volcanology, and geophysics of northern Harrat Rahat and vicinity, Kingdom of Saudi Arabia: U.S. Geological Survey Professional Paper 1862 [also released as Saudi Geological Survey Special Report SGS–SP–2021–1], 49 p., https://doi.org/10.3133/pp1862E.

Dietterich, H.R., Downs, D.T., Stelten, M.E., and Zahran, H., 2018, Reconstructing lava flow emplacement histories with rheological and morphological analyses—The Harrat Rahat volcanic field, Kingdom of Saudi Arabia: Bulletin of Volcanology, v. 80, no. 85, https://doi.org/10.1007/s00445-018-1259-4.

Downs, D.T., 2019, Major- and trace-element chemical analyses of rocks from the northern Harrat Rahat volcanic field and surrounding area, Kingdom of Saudi Arabia: U.S. Geological Survey data release, https://doi.org/10.5066/P91HL91C.

Downs, D.T., Robinson, J.E., Stelten, M.E., Champion, D.E., Dietterich, H.R., Sisson, T.W., Zahran, H., Hassan, K., and Shawali, J., 2019, Geologic map of the northern Harrat Rahat volcanic field, Kingdom of Saudi Arabia: U.S. Geological Survey Scientific Investigations Map 3428 [also released as Saudi Geological Survey Special Report SGS–SP–2019–2], 65 p., 4 sheets, scales 1:75,000, 1:25,000, https://doi.org/10.3133/sim3428.

Downs, D.T., Stelten, M.E., Champion, D.E., Dietterich, H.R., Hassan, K., and Shawali, J., 2023a, Eruptive history within the vicinity of Al Madīnah in northern Harrat Rahat, Kingdom of Saudi Arabia, chap. C *of* Sisson, T.W., Calvert, A.T., and Mooney, W.D., eds., Active volcanism on the Arabian Shield—Geology, volcanology, and geophysics of northern Harrat Rahat and vicinity, Kingdom of Saudi Arabia: U.S. Geological Survey Professional Paper 1862 [also released as Saudi Geological Survey Special Report SGS–SP–2021–1], 41 p., https://doi.org/10.3133/pp1862C.

Downs, D.T., Stelten, M.E., Champion, D.E., Dietterich, H.R., Nawab, Z., Zahran, H., Hassan, K., and Shawali, J., 2018, Volcanic history of the northernmost part of the Harrat Rahat volcanic field, Saudi Arabia: Geosphere, v. 14, p. 1253–1282, https://doi.org/10.1130/GES01625.1.

Downs, D.T., Stelten, M.E., Dietterich, H.R., Champion, D.E., Mahood, G.A., Sisson, T.W., Calvert, A.T., and Shawali, J., 2023b, Explosive trachyte eruptions from the Al Efairia volcanic center in northern Harrat Rahat, Kingdom of Saudi Arabia, chap. G *of* Sisson, T.W., Calvert, A.T., and Mooney, W.D., eds., Active volcanism on the Arabian Shield—Geology, volcanology, and geophysics of northern Harrat Rahat and vicinity, Kingdom of Saudi Arabia: U.S. Geological Survey Professional Paper 1862 [also released as Saudi Geological Survey Special Report SGS–SP–2021–1], 14 p., https://doi.org/10.3133/pp1862G.

Duncan, R.A., Kent, A.J.R., Thornber, C.R., Schlieder, T.D., and Al-Amri, A.M., 2016, Timing and composition of continental volcanism at Harrat Hutaymah, western Saudi Arabia: Journal of Volcanology and Geothermal Research, v. 313, p. 1–14, https://doi.org/10.1016/j.jvolgeores.2016.01.010.

El Difrawy, M.A., Runge, M.G., Moufti, M.R., Cronin, S.J., and Bebbington, M., 2013, A first hazard analysis of the Quaternary Harrat Al-Madinah volcanic field, Saudi Arabia: Journal of Volcanology and Geothermal Research, v. 267, p. 39–46, https://doi.org/10.1016/j.jvolgeores.2013.09.006.

Fierstein, J., Hildreth, W., and Calvert, A.T., 2011, Eruptive history of South Sister, Oregon Cascades: Journal of Volcanology and Geothermal Research, v. 207, p. 145–179, https://doi.org/10.1016/j.jvolgeores.2011.06.003.

Fleck, R.J., Calvert, A.T., Coble, M.A., Wooden, J.L., Hodges, K., Hayden, L.A., van Soest, M.C., du Bray, E.A., and John, D.A., 2019, Characterization of the rhyolite of Bodie Hills and $^{40}Ar/^{39}Ar$ intercalibration of Ar mineral standards: Chemical Geology, v. 525, p. 282–302.

Fleck, R.J., Hagstrum, J.T., Calvert, A.T., Evarts, R.C., and Conrey, R.M., 2014, $^{40}Ar/^{39}Ar$ geochronology, paleomagnetism, and evolution of the Boring volcanic field, Oregon and Washington, United States: Geosphere, v. 10, p. 1283–1314, https://doi.org/10.1130/GES00985.1.

Gallant, E., Richardson, J., Connor, C., Wetmore, P., and Connor, L., 2018, A new approach to probabilistic lava flow hazard assessments, applied to the Idaho National Laboratory, eastern Snake River Plain, Idaho, United States: Geology, v. 46, p. 895–898, https://doi.org/10.1130/G45123.1.

Gosse, J.C., and Phillips, F.M., 2001, Terrestrial in situ cosmogenic nuclides—Theory and application: Quaternary Science Reviews, v. 20, p. 1475–1560, https://doi.org/10.1016/S0277-3791(00)00171-2.

Hasenaka, T., and Carmichael, I.S.E., 1985, A compilation of location, size, and geomorphological parameters of volcanoes of the Michoacan-Guanajuato volcanic field, central Mexico: Geofisica Internacional, v. 24, p. 577–607.

Kawabata, E., Cronin, S.J., Bebbington, M.S., Moufti, M.R.H., El-Masry, N., and Wang, T., 2015, Identifying multiple eruption phases from a compound tephra blanket—an example of the AD1256 Al-Madinah eruption, Saudi Arabia: Bulletin of Volcanology, v. 77, https://doi.org/10.1007/s00445-014-0890-y.

Kereszturi, G., Németh, K., Cronin, S.J., Agustín-Flores, J., Smith, I.E.M., and Lindsay, J., 2013, A model for calculating eruptive volumes for monogenetic volcanoes—Implication for the Quaternary Auckland Volcanic Field, New Zealand: Journal of Volcanology and Geothermal Research, v. 266, p. 16–33, https://doi.org/10.1016/j.jvolgeores.2013.09.003.

Klein, F.W., 1982, Patterns of historical eruptions at Hawaiian volcanoes: Journal of Volcanology and Geothermal Research, v. 12, p. 1–35, https://doi.org/10.1016/0377-0273(82)90002-6.

Lal, D., 1991, Cosmic ray labeling of erosion surfaces—in situ nuclide production rates and erosion models: Earth and Planetary Science Letters, v. 104, p. 424–439, https://doi.org/10.1016/0012-821X(91)90220-C.

Langenheim, V.E., Ritzinger, B.T., Zahran, H., Shareef, A., and Al-dahri, M., 2019, Crustal structure of the northern Harrat Rahat volcanic field (Saudi Arabia) from gravity and aeromagnetic data: Tectonophysics, v. 750, p. 9–21, https://doi.org/10.1016/j.tecto.2018.11.005.

Langenheim, V.E., Ritzinger, B.T., Zahran, H.M., Shareef, A., and Al-Dhahry, M.K., 2023, Depth to basement and crustal structure of the northern Harrat Rahat volcanic field, Kingdom of Saudi Arabia, from gravity and aeromagnetic data, chap. K *of* Sisson, T.W., Calvert, A.T., and Mooney, W.D., eds., Active volcanism on the Arabian Shield—Geology, volcanology, and geophysics of northern Harrat Rahat and vicinity, Kingdom of Saudi Arabia: U.S. Geological Survey Professional Paper 1862 [also released as Saudi Geological Survey Special Report SGS–SP–2021–1], 18 p., https://doi.org/10.3133/pp1862K.

Lee, J.Y., Marti, K., Severinghaus, J.P., Kawamura, K., Yoo, H.S., Lee, J.B., and Kim, J.S., 2006, A redetermination of the isotopic abundances of atmospheric Ar: Geochimica et Cosmochimica Acta, v. 70, p. 4507–4512, https://doi.org/10.1016/j.gca.2006.06.1563.

Lipman, P.W., and Calvert, A.T., 2013, Modeling volcano growth on the Island of Hawaii—Deep-water perspectives: Geosphere, v. 9, p. 1348–1383, https://doi.org/10.1130/GES00935.1.

Ludwig, K.R., 2003, Isoplot/Ex 3.00—A geochronological toolkit for Microsoft Excel: Berkeley Geochronology Center Special Publications, no. 4, 1–72 p.

Mahood, G.A., and Benson, T.R., 2017, Using $^{40}Ar/^{39}Ar$ ages of intercalated silicic tuffs to date flood basalts—Precise ages for Steens Basalt Member of the Columbia River Basalt Group: Earth and Planetary Science Letters, v. 459, p. 340–351, https://doi.org/10.1016/j.epsl.2016.11.038.

Marrero, S.M., Phillips, F.M., Borchers, B., Lifton, N., Aumer, R., and Balco, G., 2016, Cosmogenic nuclide systematics and the CRONUScalc program: Quaternary Geochronology, v. 31, p. 160–187, https://doi.org/10.1016/j.quageo.2015.09.005.

McGetchin, T.R., Settle, M., and Chouet, B.A., 1974, Cinder cone growth modeled after Northeast Crater, Mount Etna, Sicily: Journal of Geophysical Research, v. 79, p. 3257–3272, https://doi.org/10.1029/jb079i023p03257.

Moufti, M.R.H., 1985, The geology of Harrat Al Madinah volcanic field, Harrat Rahat, Saudi Arabia: University of Lancaster, Ph.D. dissertation, 407 p.

Moufti, M.R., Moghazi, A.M., and Ali, K.A., 2012, Geochemistry and Sr-Nd-Pb isotopic composition of the Harrat Al-Madinah Volcanic Field, Saudi Arabia: Gondwana Research, v. 21, p. 670–689, https://doi.org/10.1016/j.gr.2011.06.003.

Moufti, M.R., Moghazi, A.M., and Ali, K.A., 2013, $^{40}Ar/^{39}Ar$ geochronology of the Neogene-Quaternary Harrat Al-Madinah intercontinental volcanic field, Saudi Arabia—Implications for duration and migration of volcanic activity: Journal of Asian Earth Sciences, v. 62, p. 253–268, https://doi.org/10.1016/j.jseaes.2012.09.027.

Murcia, H., Lindsay, J.M., Németh, K., Smith, I.E.M., Cronin, S.J., Moufti, M.R.H., El-Masry, N.N., and Niedermann, S., 2017, Geology and geochemistry of Late Quaternary volcanism in northern Harrat Rahat, Kingdom of Saudi Arabia—Implications for eruption dynamics, regional stratigraphy and magma evolution, *in* Németh, K., Carrasco-Núñez, G., Aranda-Gómez, J.J., and Smith, I.E.M., eds., Monogenetic volcanism: Geological Society of London Special Publications, v. 446, p. 173–204, https://doi.org/10.1144/SP446.2.

Murcia, H., Németh, K., El-Masry, N.N., Lindsay, J.M., Moufti, M.R.H., Wameyo, P., Cronin, S.J., Smith, I.E.M., and Kereszturi, G., 2015, The Al-Du'aythah volcanic cones, Al-Madinah City—implications for volcanic hazards in northern Harrat Rahat, Kingdom of Saudi Arabia: Bulletin of Volcanology, v. 77, https://doi.org/10.1007/s00445-015-0936-9.

Murcia, H., Németh, K., Moufti, M.R., Lindsay, J.M., El-Masry, N., Cronin, S.J., Qaddah, A., and Smith, I.E.M., 2014, Late Holocene lava flow morphotypes of northern Harrat Rahat, Kingdom of Saudi Arabia—Implications for the description of continental lava fields: Journal of Asian Earth Sciences, v. 84, p. 131–145, https://doi.org/10.1016/j.jseaes.2013.10.002.

Nathenson, M., 2001, Probabilities of volcanic eruptions and application to the recent history of Medicine Lake volcano, *in* Vecchia, A.V., ed., A unified approach to probabilistic risk assessments for earthquakes, floods, landslides, and volcanoes: U.S. Geological Survey Open-File Report 01-324, p. 71–74, https://doi.org/10.3133/ofr01324.

Oda, H., 2005, Recurrent geomagnetic excursions—A review for the Brunhes normal polarity chron: The Journal of Geography, v. 114, p. 174–193, https://doi.org/10.5026/jgeography.114.2_174.

Pearce, J.A., and Norry, M.J., 1979, Petrogenetic implications of Ti, Zr, Y, and Nb variations in volcanic rocks: Contributions to Mineralogy and Petrology, v. 69, p. 33–47, https://doi.org/10.1007/BF00375192.

Pellaton, C., 1981, Geologic map of the Al Madinah quadrangle, sheet 24D, Kingdom of Saudi Arabia: Saudi Arabian Deputy Ministry for Mineral Resources Geoscience Map GM–52, scale 1:250,000, 19 p.

Robinson, J.E., and Downs, D.T., 2023, Overview of the Cenozoic geology of the northern Harrat Rahat volcanic field, Kingdom of Saudi Arabia, chap. R *of* Sisson, T.W., Calvert, A.T., and Mooney, W.D., eds., Active volcanism on the Arabian Shield—Geology, volcanology, and geophysics of northern Harrat Rahat and vicinity, Kingdom of Saudi Arabia: U.S. Geological Survey Professional Paper 1862 [also released as Saudi Geological Survey Special Report SGS–SP–2021–1], 20 p., scale 1:100,000, https://doi.org/10.3133/pp1862R.

Runge, M.G., Bebbington, M.S., Cronin, S.J., Lindsay, J.M., Kenedi, C.L., and Moufti, M.R.H., 2014, Vents to events—Determining an eruption event record from volcanic vent structures for the Harrat Rahat, Saudi Arabia: Bulletin of Volcanology, v. 76, p. 1–16, https://doi.org/10.1007/s00445-014-0804-z.

Runge, M.G., Bebbington, M.S., Cronin, S.J., Lindsay, J.M., and Moufti, M.R., 2016, Integrating geological and geophysical data to improve probabilistic hazard forecasting of Arabian Shield volcanism: Journal of Volcanology and Geothermal Research, v. 311, p. 41–59, https://doi.org/10.1016/j.jvolgeores.2016.01.007.

Salters, V.J.M., Sachi-Kocher, A., Downs, D.T., Stelten, M.E., and Sisson, T.W., 2023, Isotopic and geochemical evidence for the source of volcanism at Harrat Rahat, Kingdom of Saudi Arabia, chap. J *of* Sisson, T.W., Calvert, A.T., and Mooney, W.D., eds., Active volcanism on the Arabian Shield—Geology, volcanology, and geophysics of northern Harrat Rahat and vicinity, Kingdom of Saudi Arabia: U.S. Geological Survey Professional Paper 1862 [also released as Saudi Geological Survey Special Report SGS–SP–2021–1], 30 p., https://doi.org/10.3133/pp1862J.

Scott, W.E., Iverson, R.M., Vallance, J.W., and Hildreth, W., 1995, Volcano hazards in the Mount Adams region, Washington: U.S. Geological Survey Open-File Report 95-492, 11 p., https://doi.org/10.3133/ofr95492.

Shaw, J.E., Baker, J.A., Menzies, M.A., Thirlwall, M.F., and Ibrahim, K.M., 2003, Petrogenesis of the largest intraplate volcanic field on the Arabian Plate (Jordan)—A mixed lithosphere–asthenosphere source activated by lithospheric extension: Journal of Petrology, v. 44, p. 1657–1679, https://doi.org/10.1093/petrology/egg052.

Sisson, T.W., Downs, D.T., Calvert, A.T., Dietterich, H.R., Mahood, G.A., Salters, V.J.M., Stelten, M.E., and Shawali, J., 2023, Mantle origin and crustal differentiation of basalts and hawaiites of northern Harrat Rahat, Kingdom of Saudi Arabia, chap. I *of* Sisson, T.W., Calvert, A.T., and Mooney, W.D., eds., Active volcanism on the Arabian Shield—Geology, volcanology, and geophysics of northern Harrat Rahat and vicinity, Kingdom of Saudi Arabia: U.S. Geological Survey Professional Paper 1862 [also released as Saudi Geological Survey Special Report SGS–SP–2021–1], 42 p., https://doi.org/10.3133/pp1862I.

Sprung, P., Schuth, S., Münker, C., and Hoke, L., 2007, Intraplate volcanism in New Zealand—The role of fossil plume material and variable lithospheric properties: Contributions to Mineralogy and Petrology, v. 153, p. 669–687, https://doi.org/10.1007/s00410-006-0169-1.

Steiger, R.H., and Jäger, E., 1977, Subcommission on geochronology—Convention on the use of decay constants in geo- and cosmochronology: Earth and Planetary Science Letters, v. 36, p. 359–362, https://doi.org/10.1016/0012-821X(77)90060-7.

Stein, M., and Hofmann, A.W., 1992, Fossil plume head beneath the Arabian lithosphere?: Earth and Planetary Science Letters, v. 114, p. 193–209, https://doi.org/10.1016/0012-821X(92)90161-N.

Stelten, M.E., 2021, Ar isotope data for rocks from the northern Harrat Rahat volcanic field and surrounding area, Kingdom of Saudi Arabia: U.S. Geological Survey data release, https://doi.org/10.5066/P92FB6AQ.

Stelten, M.E., Downs, D.T., Champion, D.E., Dietterich, H.R., Calvert, A.T., Sisson, T.W., Mahood, G.A., and Zahran H., 2020, The timing and compositional evolution of volcanism within northern Harrat Rahat, Kingdom of Saudi Arabia: Geological Society of America Bulletin, v. 132, no. 7–8, p. 1381–1403, https://doi.org/10.1130/B35337.1.

Stelten, M.E., Downs, D.T., Dietterich, H.R., Mahood, G.A., Calvert, A.T., Sisson, T.W., Witter, M.R., Zahran, H.M., and Shawali, J., 2023, The duration and characteristics of magmatic differentiation from basalt to trachyte within the Matan volcanic center, northern Harrat Rahat, Kingdom of Saudi Arabia, chap. F *of* Sisson, T.W., Calvert, A.T., and Mooney, W.D., eds., Active volcanism on the Arabian Shield—Geology, volcanology, and geophysics of northern Harrat Rahat and vicinity, Kingdom of Saudi Arabia: U.S. Geological Survey Professional Paper 1862 [also released as Saudi Geological Survey Special Report SGS–SP–2021–1], 56 p., https://doi.org/10.3133/pp1862F.

Stelten, M.E., Downs, D.T., Dietterich, H.R., Mahood, G.A., Calvert, A.T., Sisson, T.W., Zahran, H., and Shawali, J., 2018, Timescales of magmatic differentiation from alkali basalt to trachyte within the Harrat Rahat volcanic field, Kingdom of Saudi Arabia: Contributions to Mineralogy and Petrology, v. 173, 17 p., https://doi.org/10.1007/s00410-018-1495-9.

Stern, R.J., and Johnson, P., 2010, Continental lithosphere of the Arabian Plate—A geologic, petrologic, and geophysical synthesis: Earth-Science Reviews, v. 101, p. 29–67, https://doi.org/10.1016/j.earscirev.2010.01.002.

Stone, J.O., 2000, Air pressure and cosmogenic isotope production: Journal of Geophysical Research Solid Earth, v. 105, p. 23,753–23,759, https://doi.org/10.1029/2000JB900181.

Swanson, D.A., 1972, Magma supply rate at Kilauea volcano, 1952-1971: Science, v. 175, p. 169–170, https://doi.org/10.1126/science.175.4018.169.

Taggart, J.E., Jr., ed., 2002, Analytical methods for chemical analysis of geologic and other materials, U.S. Geological Survey: U.S. Geological Survey Open-File Report 02-223, 20 p., https://doi.org/10.3133/ofr02223.

Yao, Z., Mooney, W.D., Zahran, H.M., and Youssef, S.E.H., 2017, Upper mantle velocity structure beneath the Arabian shield from Rayleigh surface wave tomography and its implications: Journal of Geophysical Research Solid Earth, v. 122, p. 6552–6568, https://doi.org/10.1002/2016JB013805.

Appendix 1. Details on Samples Collected for ^{36}Cl Cosmogenic Surface-Exposure Dating

^{36}Cl Cosmogenic Surface-Exposure Dating

Eleven samples for ^{36}Cl cosmogenic surface-exposure dating were collected from within the mapping area using a hammer and chisel. Five of these samples have been described by Downs and others (2018) and Stelten and others (2018) and we refer the reader to those publications for a description of those samples (R15MS004, R15TS189, R14TS097, R14AC099, and R15MS006).

Five samples were collected from three young-appearing basalt flows that are together referred to as the Five Fingers flows, located in the northeastern part of the study area (see fig. 6 of the main text). One whole-rock sample from the basalt of Northern Fingers (R14TS019), one whole-rock sample from the basalt of Central Finger (R14MS030), two whole-rock samples from the basalt of Southern Fingers (R14TS009a and R15MS014), and one plagioclase separate from the basalt of Southern Fingers (R15DS107) were analyzed for ^{36}Cl exposure ages. Sample R14TS019 is a whole-rock sample collected from the top 4 centimeters (cm) of a 2 by 2 meter (m) flat-topped, high standing region of the flow that is 4.3 kilometers (km) northeast of the source vent. Sample R14TS019 contains phenocrysts of plagioclase (less than 1–3 percent, as long as 8 millimeters [mm] in length) and olivine (less than 1–2 percent, as long as 2 mm). Sample R15MS030 was collected from the top 4 cm of a large, 3 by 3 m, flat-topped block (clinker) at the distal part of the lava flow, about 9.5 km northeast of the source vent. The sample was collected more than 50 cm from the edge of the block and is composed of vesicular basalt with phenocrysts of plagioclase (2 percent, as long as mm) and olivine (less than 1–3 percent, as long as 5 mm).

Three samples were collected from the basalt of Southern Fingers to test the reproducibility of the ^{36}Cl dating method. R14TS009a is a sample of pāhoehoe collected from on top of a tumulus mound, about 3.6 km east-northeast of its source vent. The sample was trimmed such that only the upper 4 cm of the surface sample were used for ^{36}Cl dating. Sample R14TS009a is composed of vesicular basalt with phenocrysts of plagioclase (1–5 percent, as long as 40 mm) and olivine (less than 1–3 percent, as long as 30 mm). The basalt of Southern Fingers is easily distinguishable from the basalt of Northern Fingers by the presence of large feldspar (as long as 40 mm) and olivine (as long as 30 mm) grains. Sample R15MS014 is a sample of vesicular basalt with phenocrysts of plagioclase (1–5 percent, as long as 40 mm) and olivine (less than 1–3 percent, as long as 30 mm), collected from the top of a tumulus mound that stands 0.3 to 1 m above the surrounding flow, about 4.3 km northeast of its source vent. The sample was collected from the central, flat lying part of the tumulus mound and trimmed such that the upper 5 cm of the surface sample was analyzed for ^{36}Cl dating. Sample R15DS107 consists of 0.5- to 2-cm-long plagioclase phenocrysts collected from a flat part of the basalt of Southern Fingers, about 11.8 km northeast of the source vent. The plagioclase phenocrysts collected were loose on the surface of the flow but are petrographically identical to large plagioclase phenocrysts that are ubiquitous in the basalt of Southern Fingers and were likely eroded from the surface of the lava flow shortly after emplacement. These plagioclase phenocrysts are interpreted to be derived from the upper centimeter of the lava flow surface.

Sample R17AC138 is an aphyric trachyte collected from a dense, flat, 4 by 4 m block on the west rim of Um Rgaibah that stands 1 m above the its immediate surroundings. The sample was trimmed such that only the upper 4 cm of the surface sample were used for ^{36}Cl dating. The peak of Um Rgaibah is about 24 m above and 226 m to the east of the sample location, yielding an angle of 6° to the horizon at an azimuth of 90° to 150°. No topographic shielding is observed in any other direction.

For all samples collected for this study, the dip of the sample surface collected was negligible (less than 5°). At all sample locations shielding was negligible, with the angle to the horizon being less than or equal to 6° in all directions (Gosse and Phillips, 2001). As such, no shielding correction was applied to samples from this study. Sample locations and elevations were measured by a Global Positioning System using the World Geodetic System of 1984 Universal Transverse Mercator zone 37R north datum, and later confirmed using a 1 m-resolution digital elevation model. For all samples, erosion rates are estimated to be low (less than or equal to 1 millimeter per thousand years [mm/k.y.]) based on the preservation of small-scale (less than 1 cm), irregular surface features on each flow. Given the uncertainty in the erosion rate for each sample site, we conservatively assume an erosion rate of 1±1 mm/k.y. (0.5±0.5 mm/k.y. for Um Rgaibah). See table 2.2 in appendix 2 for all input parameters for ^{36}Cl age calculations.

Chemical separation and analysis of samples via accelerator mass spectrometry took place at the Purdue Rare Isotope Measurement (PRIME) Laboratory at Purdue University in West Lafayette, Indiana. Samples were chemically dissolved, spiked with a ^{35}Cl enriched tracer (for example, Desilets and others, 2006), and analyzed via accelerator mass spectrometry. Splits of each sample were analyzed for their major-element concentrations via wavelength dispersive X-ray fluorescence and for their trace-element concentrations via inductively coupled plasma atomic emission spectrometry (ICP-AES) and inductively coupled

plasma mass spectrometry (ICP-MS) at the U.S. Geological Survey in Denver, Colorado, following Taggart (2002). All whole-rock samples contained vesicle fill composed of secondary zeolites, carbonate, gypsum and anhydrite, clay, and wind-blown loess. These characteristics are ubiquitous for surface samples throughout northern Harrat Rahat. Prior to analysis for major- and trace-element concentrations, all samples were cleaned by (1) heating in deionized water at 60 degrees Celsius (°C) for an hour to dissolve any gypsum and anhydrite, (2) heating in deionized water at 90 °C for an hour to dissolve any zeolites, (3) sonicating for 8 hours to disaggregate any foreign material, (4) placing the samples in concentrated nitric acid (HNO_3) to dissolve carbonate, and (5) sonicating in deionized water for 8 hours to disaggregate any remaining foreign material. Trace elements of particular importance for the calculation of ^{36}Cl cosmogenic surface-exposure ages are U and Th, which can indirectly produce thermal neutrons as a result of alpha decay, and B, Li, Sm, and Gd, which have large thermal neutron absorption cross sections, and therefore reduce the production of ^{36}Cl from ^{35}Cl. In some cases, B and Li concentrations were below detection limits. Given that the detection limit for B and Li is 10 parts per million, we assume the concentration of B and Li is 5±5 parts per million for all samples where these elements were below detection limit.

Cosmogenic surface-exposure ages were calculated using the online CRONUScalc ^{36}Cl Exposure Age Calculator ver. 2.0 (visit the Cosmic-Ray Produced Nuclide Systematics on Earth Project: http://www.physics.purdue.edu/primelab/CronusProject/cronus/ for more information) that utilizes a MATLAB-based code and is described by Marrero and others (2016). Ages were calculated using the Lal and Stone time-independent scaling model (Lal, 1991; Stone, 2000). We refer the reader to Marrero and others (2016) for a detailed discussion of production rates for various production pathways, details of scaling models, and other parameters used in the calculation of ^{36}Cl cosmogenic surface-exposure ages.

References Cited

Desilets, D., Zreda, M., Almasi, P.F., and Elmore, D., 2006, Determination of cosmogenic ^{36}Cl in rocks by isotope dilution—innovations, validation and error propagation: Chemical Geology, v. 233, p. 185–195, https://doi.org/10.1016/j.chemgeo.2006.03.001.

Downs, D.T., Stelten, M.E., Champion, D.E., Dietterich, H.R., Nawab, Z., Zahran, H., Hassan, K., and Shawali, J., 2018, Volcanic history of the northernmost part of the Harrat Rahat volcanic field, Saudi Arabia: Geosphere, v. 14, p. 1253–1282, https://doi.org/10.1130/GES01625.1.

Gosse, J.C., and Phillips, F.M., 2001, Terrestrial in situ cosmogenic nuclides—Theory and application: Quaternary Science Reviews, v. 20, p. 1475–1560, https://doi.org/10.1016/S0277-3791(00)00171-2.

Lal, D., 1991, Cosmic ray labeling of erosion surfaces—In situ nuclide production rates and erosion models: Earth and Planetary Science Letters, v. 104, p. 424–439, https://doi.org/10.1016/0012-821X(91)90220-C.

Marrero, S.M., Phillips, F.M., Borchers, B., Lifton, N., Aumer, R., and Balco, G., 2016, Cosmogenic nuclide systematics and the CRONUScalc program: Quaternary Geochronology, v. 31, p. 160–187, https://doi.org/10.1016/j.quageo.2015.09.005.

Stelten, M.E., Downs, D.T., Dietterich, H.R., Mahood, G.A., Calvert, A.T., Sisson, T.W., Zahran, H., and Shawali, J., 2018, Timescales of magmatic differentiation from alkali basalt to trachyte within the Harrat Rahat volcanic field, Kingdom of Saudi Arabia: Contributions to Mineralogy and Petrology, v. 173, https://doi.org/10.1007/s00410-018-1495-9.

Stone, J.O., 2000, Air pressure and cosmogenic isotope produc tion: Journal of Geophysical Research, Solid Earth, v. 105, p. 23753–23759, https://doi.org/10.1029/2000JB900181.

Taggart, J.E., Jr., ed., 2002, Analytical methods for chemical analysis of geologic and other materials, U.S. Geological Survey: U.S. Geological Survey Open-File Report 02-223, 20 p. https://doi.org/10.3133/ofr02223.

Appendix 2. ^{36}Cl Data

This appendix includes input parameters and full output for ^{36}Cl surface-exposure age calculations using the online CRONUScalc ^{36}Cl Exposure Age Calculator ver. 2.0 (Marrero and others, 2016). Ages were calculated using the Lal and Stone time-independent scaling model (Lal, 1991; Stone, 2000). See appendix 1 for details on analytical methods, sample characteristics, and data reduction methods. Eastings and northings are reported in Universal Transverse Mercator zone 37R north coordinates using the World Geodetic System of 1984 datum.

Table 2.1. ^{36}Cl output parameters.

[atoms/g, atoms per gram; atoms/g/yr, atoms per gram per year; ka, thousand years ago; mm/k.y., millimeter per thousand years]

Parameter	Sample R15DS107	Sample R14TS019	Sample R15MS014	Sample R14TS009a	Sample R15MS030	Sample R17AC138
Unit symbol	bsof	bnof	bsof	bsof	bcef	trg
Material	Plagioclase	Whole-rock	Whole-rock	Whole-rock	Whole-rock	Whole-rock
Age (ka)	21.4	22	26	26.4	29.1	9
Uncertainty as ±1σ (ka)	2.3	3.3	3	2.9	3.7	2.5
Erosion rate (mm/k.y.)	0.268	0.233	0.233	0.236	0.187	0.123
Scaling Ca spallation	1.3691	1.3856	1.4623	1.4682	1.3716	1.8538
Scaling K spallation	1.3691	1.3856	1.4623	1.4682	1.3716	1.8538
Scaling Fe spallation	1.3691	1.3856	1.4623	1.4682	1.3716	1.8538
Scaling Ti spallation	1.3691	1.3856	1.4623	1.4682	1.3716	1.8538
Scaling Cl epithermal	1.3691	1.3856	1.4623	1.4682	1.3716	1.8538
Scaling Cl thermal	1.3691	1.3856	1.4623	1.4682	1.3716	1.8538
Scaling fast muons	1.0895	1.0977	1.1339	1.1367	1.0911	1.3121
Scaling slow muons	1.0895	1.0977	1.1339	1.1367	1.0911	1.3121
Production Ca spallation (atoms/g/yr)	6.07	4.411	5.6998	5.6342	4.745	0.87327
Production K spallation (atoms/g/yr)	0.35445	1.3396	0.98615	0.6917	1.2166	11.2072
Production Fe spallation (atoms/g/yr)	0.007768	0.25221	0.23762	0.24488	0.21965	0.13598
Production Ti spallation (atoms/g/yr)	0.003663	0.15303	0.12484	0.10221	0.1507	0.010809
Production Ca muons (atoms/g/yr)	0.25563	0.18712	0.23802	0.23386	0.20394	0.033579
Production K muons (atoms/g/yr)	0.014836	0.056463	0.041052	0.028616	0.05207	0.43569
Production Cl low Energy (atoms/g/yr)	0.041702	5.8311	2.5916	2.4065	3.7972	42.6656
Thermal neutron absorption cross section, σ_{th}	0.009048	0.008883	0.008759	0.009053	0.009277	0.008771
Epithermal neutron absorption cross section, σ_{eth}	0.020981	0.02185	0.020465	0.021686	0.025685	0.036391
Neutron scattering cross section, σ_{sc}	0.10751	0.1087	0.10614	0.10816	0.11038	0.11923
Spallation production ratio, Q_s	1.0308	0.97794	0.98476	0.99139	0.98612	0.9749
Thermal neutron production ratio, Q_{th}	1.0712	1.2278	1.2466	1.2305	1.1959	1.2794
Epithermal neutron production ratio, Q_{eth}	1.046	1.1259	1.1412	1.1269	1.0943	1.0699
Muon production ratio, Q_{mu}	0.99903	0.99663	0.99485	0.99532	0.9974	0.99181
Cosmogenic Cl (atoms/g)	138,615.8	269,998.9	254,193.9	241,830.2	299,268.2	501,941.7
Radiogenic Cl (atoms/g)	17.1878	5,933.062	1,551.134	816.806	3,948.762	2,20843.3
Analytical (internal) uncertainty (atoms/g)	1.1306	1.6009	1.6748	1.5411	1.7879	1.7434
Percentage of ^{36}Cl production from Ca	93.7	37.6	59.9	62.8	47.7	1.6

Table 2.1. ^{36}Cl output parameters.—Continued

Parameter	Sample R15DS107	Sample R14TS019	Sample R15MS014	Sample R14TS009a	Sample R15MS030	Sample R17AC138
Percentage of ^{36}Cl production from K	5.5	11.4	10.4	7.7	12.2	21.0
Percentage of ^{36}Cl production from native Cl	0.6	47.7	26.1	25.8	36.6	77.1

Table 2.2. ^{36}Cl input parameters.

[cm, centimeter; g, gram; g/cm^2, gram per square centimeter; g/cm^3, gram per cubic centimeter; hPa, hectopascal; m, meter; mASL, meter above sea level; mm/k.y., millimeter per thousand years; ppm, parts per million; wt. %, weight percent; %, percent; Conc., concentration]

Parameter (units)	Sample R15DS107	Sample R14TS019	Sample R15MS014	Sample R14TS009a	Sample R15MS030	Sample R17AC138
Latitude (decimal degrees)	24.32655	24.38701	24.30618	24.30032	24.40616	24.09037
Longitude (decimal degrees)	39.95606	39.84943	39.88596	39.87988	39.88156	39.9601
Elevation (mASL)	820.3	834.9	913.8	919.6	820.1	1,261
Pressure (hPa)	N/A	N/A	N/A	N/A	N/A	N/A
Sample thickness (cm)	1	4	4.5	4	4	4
Bulk density (g/cm^3)	2.68	2.33	2.33	2.36	1.87	2.45
Shielding factor	1	1	1	1	1	1
Erosion rate (mm/k.y.)	1	1	1	1	1	0.5
Conc. ^{36}Cl (atoms/gram)	138,633	275,932	255,745	242,647	303,217	722,785
Attenuation length (g/cm^2)	165	165	165	165	165	165
Depth to top of sample (cm)	0	0	0	0	0	0
Year collected (C.E.)	2015	2015	2015	2015	2015	2017
Water content in pores (volume fraction)	0.01	0.01	0.01	0.01	0.01	0.01
Mineral separation	Yes	No	No	No	No	No
Bulk-rock SiO_2 (wt.%)	45.6	45.5	46.2	45.6	47	62.9
Bulk-rock TiO_2 (wt.%)	2.39	3.79	2.94	2.39	3.75	0.21
Bulk-rock Al_2O_3 (wt.%)	16.2	16.7	17.2	16.2	17.4	17.3
Bulk-rock Fe_2O_3 (wt.%)	13.2	14.4	12.9	13.2	12.6	5.8
Bulk-rock MnO (wt.%)	0.18	0.18	0.17	0.18	0.14	0.2
Bulk-rock MgO (wt.%)	8.88	6.58	6.23	8.88	4.68	0.18
Bulk-rock CaO (wt.%)	10.6	8.79	10.8	10.6	9.5	1.3
Bulk-rock Na_2O (wt.%)	2.8	3.62	3.06	2.8	3.36	7.0
Bulk-rock K_2O (wt.%)	0.39	0.8	0.56	0.39	0.73	5.01
Bulk-rock P_2O_5 (wt.%)	0.2	0.35	0.22	0.2	0.29	0.05
Analytical water (wt.%)	0.41667	0.41663	0.32693	0.41667	0.596	1.47
Bulk-rock CO_2 (wt.%)	0.2	0.2	0.2	0.2	0.2	0.2
Bulk-rock Cl (ppm)	57.1	147.6	60	57.1	101	792.0568
Bulk-rock B (ppm)	5	5	5	5	5	15
Bulk-rock Sm (ppm)	3.2	4.8	4.2	3.2	5	11.7

Table 2.2. ^{36}Cl input parameters.—Continued

Parameter (units)	Sample R15DS107	Sample R14TS019	Sample R15MS014	Sample R14TS009a	Sample R15MS030	Sample R17AC138
Bulk-rock Gd (ppm)	3.69	4.92	4.57	3.69	5.3	11.3
Bulk-rock U (ppm)	0.17	0.41	0.28	0.17	0.48	2.54
Bulk-rock Th (ppm)	0.4	1.3	0.8	0.4	1.2	7.6
Bulk-rock Cr (ppm)	309	68	187	309	184	5
Bulk-rock Li (ppm)	5	5	5	5	5	29
Target K_2O (wt.%)	0.21	NaN	NaN	NaN	NaN	NaN
Target CaO (wt.%)	12	NaN	NaN	NaN	NaN	NaN
Target TiO_2 (wt.%)	0.09	NaN	NaN	NaN	NaN	NaN
Target Fe_2O_3 (wt.%)	0.44	NaN	NaN	NaN	NaN	NaN
Target Cl (ppm)	1.2	NaN	NaN	NaN	NaN	NaN
Latitude uncertainty (decimal degrees)	0.00001	0.00001	0.00001	0.00001	0.00001	0.00001
Longitude uncertainty (decimal degrees)	0.00001	0.00001	0.00001	0.00001	0.00001	0.00001
Elevation uncertainty (m)	0.5	0.5	0.5	0.5	0.5	2.5
Pressure uncertainty (hPa)	NaN	NaN	NaN	NaN	NaN	NaN
Sample thickness uncertainty (cm)	0.5	0.5	0.5	0.5	0.5	0.5
Bulk density uncertainty (g/cm^3)	0.001	0.000661	0.00012	0.000838	8.06E-05	0.005
Shielding factor uncertainty	0.01	0.01	0.01	0.01	0.01	0.01
Erosion-rate uncertainty (mm/k.y.)	1	1	1	1	1	0.5
Conc. ^{36}Cl uncertainty (atoms/gram)	6,484.565	17,972	15,505.38	13,367	16,732.64	95,904.58
Attenuation length uncertainty (g/cm^2)	10	10	10	10	10	10
Depth to top of sample uncertainty (cm)	0	0	0	0	0	0
Year collected uncertainty (years)	0	0	0	0	0	0
Water content in pores uncertainty (wt.%)	0.01	0.01	0.01	0.01	0.01	0.01
Bulk-rock SiO_2 uncertainty (wt.%)	0.228	0.228	0.231	0.228	0.235	0.315
Bulk-rock TiO_2 uncertainty (wt.%)	0.01195	0.01895	0.0147	0.01195	0.01875	0.0011
Bulk-rock Al_2O_3 uncertainty (wt.%)	0.081	0.084	0.086	0.081	0.087	0.087
Bulk-rock Fe_2O_3 uncertainty (wt.%)	0.066	0.072	0.065	0.066	0.063	0.029
Bulk-rock MnO uncertainty (wt.%)	0.0009	0.0009	0.00085	0.0009	0.0007	0.00096
Bulk-rock MgO uncertainty (wt.%)	0.0444	0.0329	0.03115	0.0444	0.0234	0.00091
Bulk-rock CaO uncertainty (wt.%)	0.053	0.04395	0.054	0.053	0.0475	0.00663
Bulk-rock Na_2O uncertainty (wt.%)	0.014	0.0181	0.0153	0.014	0.0168	0.03490
Bulk-rock K_2O uncertainty (wt.%)	0.00195	0.004	0.0028	0.00195	0.00365	0.02507
Bulk-rock P_2O_5 uncertainty (wt.%)	0.001	0.00175	0.0011	0.001	0.00145	0.00025
Analytical water uncertainty (wt.%)	0.2	0.2	0.2	0.2	0.2	0.2
Bulk-rock CO_2 uncertainty (wt.%)	0.2	0.2	0.2	0.2	0.2	0.2
Bulk-rock Cl uncertainty (ppm)	2.9	1.5	3.1	2.9	4.8	105.0

Table 2.2. ^{36}Cl input parameters.—Continued

Parameter (units)	Sample R15DS107	Sample R14TS019	Sample R15MS014	Sample R14TS009a	Sample R15MS030	Sample R17AC138
Bulk-rock B uncertainty (ppm)	5	5	5	5	5	1.5
Bulk-rock Sm uncertainty (ppm)	0.16	0.24	0.21	0.16	0.25	0.585
Bulk-rock Gd uncertainty (ppm)	0.1845	0.246	0.2285	0.1845	0.265	0.565
Bulk-rock U uncertainty (ppm)	0.0085	0.0205	0.014	0.0085	0.024	0.127
Bulk-rock Th uncertainty (ppm)	0.02	0.065	0.04	0.02	0.06	0.38
Bulk-rock Cr uncertainty (ppm)	15.45	3.4	9.35	15.45	9.2	5
Bulk-rock Li uncertainty (ppm)	5	5	5	5	5	1.45
Target K_2O uncertainty (wt.%)	0.00105	NaN	NaN	NaN	NaN	NaN
Target CaO uncertainty (wt.%)	0.06	NaN	NaN	NaN	NaN	NaN
Target TiO_2 uncertainty (wt.%)	0.00045	NaN	NaN	NaN	NaN	NaN
Target Fe_2O_3 uncertainty (wt.%)	0.0022	NaN	NaN	NaN	NaN	NaN
Target Cl uncertainty (ppm)	0.23	NaN	NaN	NaN	NaN	NaN
Covariance	0	0	0	0	0	0

References Cited

Lal, D., 1991, Cosmic ray labeling of erosion surfaces—in situ nuclide production rates and erosion models: Earth and Planetary Science Letters, v. 104, p. 424–439, https://doi.org/10.1016/0012-821X(91)90220-C.

Marrero, S.M., Phillips, F.M., Borchers, B., Lifton, N., Aumer, R., and Balco, G., 2016, Cosmogenic nuclide systematics and the CRONUScalc program: Quaternary Geochronology, v. 31, p. 160–187, https://doi.org/10.1016/j.quageo.2015.09.005.

Stone, J.O., 2000, Air pressure and cosmogenic isotope production: Journal of Geophysical Research Solid Earth, v. 105, p. 23753–23759, https://doi.org/10.1029/2000JB900181.

Moffett Field Publishing Service Center, California
Manuscript approved December 17, 2020
Edited by John Mark Brigham and Monica Erdman
Layout and design by Kimber Petersen
Illustration support by JoJo Mangano

Stelten and others—**Eruptive History of Northern Harrat Rahat Over the Past 1.2 Million Years**—Professional Paper 1862–D

ISSN 1044-9612 (print)
ISSN 2330-7102 (online)
https://doi.org/10.3133/pp1862D